Institut für Festkörperphysik

Friedrich-Schiller-Universität Jena

Annual Report 2006

Editors: Prof. Dr. Paul Seidel
Dr. Christian Hülsen
Uta Bornkessel

Institut für Festkörperphysik
Friedrich-Schiller-Universität Jena
Max-Wien-Platz 1
D-07743 JENA

Tel.: +49 (0) 3641 / 947410
Fax: +49 (0) 3641 / 947302
e-mail: Paul.Seidel@uni-jena.de
home page: http://www.physik.uni-jena.de/exp_phys/

Prof. Dr. Paul Seidel
director
Tel.: +49 (0) 3641 / 947410, 947411
Fax: +49 (0) 3641 / 947412
e-mail: Paul.Seidel@uni-jena.de
home page: http://www.physik.uni-jena.de/~tief

Prof. Dr. Wolfgang Richter
Tel.: +49 (0) 3641 / 947440, 947411
Fax: +49 (0) 3641 / 947442
e-mail: richter@pinet.uni-jena.de
home page: http://www.physik.uni-jena.de/~layer/

Prof. Dr. Werner Wesch
Tel.: +49 (0) 3641 / 947330, 947301
Fax: +49 (0) 3641 / 947302
e-mail: Werner.Wesch@uni-jena.de
home page: http://www.physik.uni-jena.de/~exphys/

Prof. Dr. Wolfgang Witthuhn
Tel.: +49 (0) 3641 / 947300, 947301
Fax: +49 (0) 3641 / 947302
e-mail: Wolfgang.Witthuhn@uni-jena.de
home page: http://www.physik.uni-jena.de/~exphys/

Prof. Dr. Friedrich Huisken
Tel.: +49 (0) 3641 / 947354, 947301
Fax: +49 (0) 3641 947308
e-mail: Friedrich.Huisken@uni-jena.de
home page: http://www.physik.uni-jena.de/~exphys/astrolab/

Preface

This annual report of the Institut für Festkörperphysik (IFK) of the Friedrich-Schiller-Universität Jena continues the series which was started with the year 1996 report, thus, we just started the second decade of this tradition. It summarizes the research and teaching activities and the progress achieved in 2006. As the preceding reports it again is addressed to the interested scientific community and to our colleagues within the university and from outside. We also document the use of the financial support and we would like to take the opportunity to thank all institutions for this support.

The research topics of the IFK cover different fields of solid state physics and range from fundamental questions to largely applied developments. The nuclear solid state physics groups employ electrical, optical and nuclear physics methods based on radioactive isotopes as well as ion beam techniques. The investigations are concentrated on semiconductors and optical materials. Research activities on chalcopyrite-semiconductors for thin film solar cells and optoelectronic devices are performed in the CIS-lab of the institute. In the low temperature department essentially high-T_c superconducting layers and superconducting devices like SQUIDs are studied and applied. This includes the cooling technology with self made cryocoolers as well as ultra-low temperature research. Thin films of SiC, III-nitrides and III-arsenides are deposited by molecular beam epitaxy and are characterized by a variety of surface physics methods in the thin solid films group. As a common interest within our institute investigations on carbon and silicon nanotubes were forced within the last year. The research group on laboratory astrophysics/cluster physics is devoted to fundamental astrophysical questions that can be answered by laboratory experiments, with particular emphasis on spectroscopy.

The permanent scientific staff of the IFK is strongly involved in teaching duties. The decision of the faculty to replace the diploma degree by bachelor and master degrees starting with a modularisation of the physics courses has heavily increased this burdening.

Many institutions contributed to the scientific output of the institute. The activities would be impossible without substantial financial support - equipment as well as additional scientific and technical staff - by: Thüringer Kultusministerium (TKM), Bundesministerium für Bildung und Forschung (BMBF), Bundesministerium für Wirtschaft und Technologie (BMWi), Bundesministerium für Umwelt, Naturschutz und Reaktorsicherheit (BMU), Deutsche Forschungsgemeinschaft (DFG), Europäische Gemeinschaft (EU), Nagelschneider-Stiftung, Hahn-Meitner-Institut Berlin, industrial partners and - last but not least- the Friedrich-Schiller-Universität. We express our gratitude to all these institutions.

Prof. Dr. Paul Seidel

Contents

Departments of the institute

Solid State Physics

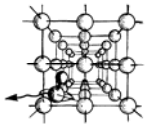

Prof. Dr. W. Witthuhn

- Structure and dynamics of impurities, defect-clusters and nanocrystals in semiconductors
- Preparation and characterization of heterogeneous thin layers for optoelectronic and photovoltaic devices; thin-film solarcells
- 3D-microstructures and material modifications by energetic ion beams

- The research of the ***solid state-/semiconductor-physics*** group is directed to three different fields:
- Investigation of structure and dynamics of local perturbations and internal fields in solid states with emphasis on atomic and electronic structures of deep intrinsic and impurity-related levels in wide-band-gap compound semiconductors. The research is part of the "Verbundforschungs-Programm" of the German BMBF, carried out at large research centres (like ISOLDE/CERN or HMI, Berlin). There exist a close cooperation with research groups at Berlin (HMI), Genf (ISOLDE/CERN), Universities at Konstanz, Saarbrücken, Freiberg, and Bonn. Furthermore, cooperations exist with the University of Oslo, Norway, and the Paul-Scherrer-Institute, Villingen, Switzerland.
- Formation and characterisation of buried metallic and/or ferromagnetic nanocrystals in wide-band-gap semiconductors for applications in optoelectronics and spintronics. Cooperation exists with groups at the Jena IPHT, the Technical University Ilmenau, the Technical University Dresden, University Ulm, University of Pittsbourgh, and the Cornell University, USA.
- Growth and characterisation of single- and polycrystalline thin layers of chalcopyrit-based semiconductors for optoelectronic and photovoltaic applications. Processing of complete solar-cells with emphasis on the systems [Cu(In,Ga)(S_2,Se_2)] and CdTe/CdS. Hetero-layers for applications in future high-efficient solar-cells. The research on CdTe/CdS-thin-film solar-cells is performed in close cooperation with the industrial partner "Antec-Solar Energy" at Rudisleben/Arnstadt. The IFK-group is member of the Thuringian "Solar Input" e.V. and of the German "PV-Uni-Netz", in which 12 German universities coordinate their research on photovoltaics.

Ion Beam Physics

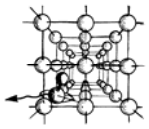

Prof. Dr. W. Wesch

- Modification of solid layers by ion implantation and succeeding processes and ion beam analysis (RBS, PIXE, ERD, NRA)
- Ion beam synthesis of buried nanostructures
- Simulation of processes of ion-solid interaction

The ***Ion Beam Physics*** Group deals with problems of modification of solids and synthesis of buried nanostructures by means of ion beams and combined secondary processes. The studies cover fundamental processes of ion-beam induced structural modification in new semiconductors and insulators being relevant for future electronic, optoelectronic and photonic device technologies, as e.g. the ternary III-V semiconductors InGaAs and InGaP (collaboration with the Australian National University Canberra, Dr. M.C. Ridgway, Prof. R. Elliman) and the wide gap semiconductor ZnO (collaboration with the University of Pretoria, South Africa, Prof. M. Hayes, and University Lisboa, Portugal, Prof. E. Alves). The structural changes in AlGaAs and Si caused by ion irradiation are also investigated by classical molecular dynamics computer simulations. At the same time the formation of ferromagnetic nanocrystals and layers in Si and GaAs by ion-beam induced non-equilibrium processes (collaboration with the University Aveiro, Portugal, Prof. N. Sobolev) and the specific modification of optical materials as $LiNbO_3$ and $KTiOPO_4$ as well as ion beam enhanced chemical etching to produce high aspect ratio microstructures for optical application of these materials (collaboration with the Institute of Applied Physics, Prof. Tünnermann) are studied. With the Institute of Bioprocess- and Analytical Technique (iba Heiligenstadt) a collaboration in the field of modification of bio-compatibility of titanium surfaces by ion beam processing exists.

Beside these activities on materials modification utilizing ion beams with conventional energies (several 10 keV to several MeV), the effect of high electronic excitation under swift heavy ion irradiation (several 100 MeV) on structural modification of crystalline semiconductors (ion track formation) as well as on plastic deformation in amorphous semiconductors is studied (collaboration with the Hahn-Meitner Institute Berlin, Dr. S. Klaumünzer).

Low Temperature Physics

Prof. Dr. P. Seidel

- Superconductivity within thin layers and layer systems
- Josephson effects, proximity effect, tunnel effects and quantum effects in superconducting devices
- DC-SQUID's and their application in measurement, e.g. biomagnetism, NDE, MRX
- cryogenic measurements on optical components (mechanical quality factor)
- Dynamics of superconducting Josephsonarrays and qubits
- cryogenic engineering (cryocoolers, cryogenic storage)

The ***low temperature physics*** group works on the following fields:

- preparation, characterization, modelling and application of Josephson junctions and SQUIDs (precision and magnetorelaxation measurements with LTS SQUIDs, non-destructive evaluation and biomagnetism with HTS SQUIDs, intrinsic Josephson junctions)
- low temperature physics and cryogenic engineering (development of new kinds of pulse tube cryocoolers, investigations on a new concept for regenerators, cryogenic storage)
- experimental work within the SFB/TR on cryogenic measurements of the Q-factor of optical components including grating optics
- thin film technologies for insulators and other materials

The research is carried out in cooperations with other research groups in Thuringia (TU Ilmenau, IPHT Jena, SQUID GmbH Jena, SUPRACON Jena, Polyoptik Bad Blankenburg, Innovent e.V. Jena). Within common activities the group works together with the Gesellschaft für Schwerionenforschung Darmstadt, DESY Hamburg, TARGET Systemelectronic GmbH Solingen and the Zentrum für Raumfahrttechnologie und Mikrogravitation Bremen.

With industrial partners there exist some resarch activies e.g. with Air Liquide (France), Northrop Gruman (USA), AEG Infrared Moduls GmbH Heilbronn and the TransMIT center for adaptive cryotechniques Gießen. A long tradition of cooperation exists with the Institute of Electrical Engineering (IEE) of the Slovak Academy of Sciences Bratislava, the Universities of Moscow (Russia), Kharkov (Ukraine), Glasgow (U.K.) and Vienna (Austria), the Tohoku University Sendai and the University of Osaka (both in Japan).

Physics of Thin Films

Prof. Dr. W. Richter

- Deposition of thin films using molecular beam epitaxy for electronic and optoelectronic devices
- Epitaxy of SiC and III-V-compounds
- Analysis of layers and surfaces using AES, XPS, UPS, LEED, RHEED, STM, TEM

The group **„Physics of thin films“** is engaged in the research on nanostructures, solid surfaces and thin films of semiconductor materials like silicon carbide and gallium aluminium arsenide as well as on carbon nanotubes and organic molecules on semiconductor surfaces.
For analysis of the chemical composition and bonding at surfaces and in thin films we use surface analysis methods like photoelectron spectroscopy (XPS, UPS) and Auger electron spectroscopy (AES). The crystalline structure can be determined by electron diffraction (LEED, XPD, and electron channeling. Scanning tunneling microscopy and atomic force microscopy are used for high-resolution imaging of nanostructures and surfaces.
Molecular beam epitaxy (MBE) in ultra-high vacuum is the preferred technique to grow nanostructures and semiconductor heterostructures (Si, Ge, SiC polytypes, GaAs, AlAs, and InGaAs) for electronic and optoelectronic applications. Carbon nanotubes can also be produced by chemical vapour deposition (CVD). Our particular interest is to understand and to control the effects of the substrate surface preparation and of the growth conditions on the structure and the properties of thin films. We investigate the self-assembly of nanostructures to grow quantum dots, carbon nanotubes or organic films. All these investigations aim to an active control of the growth processes. Additionally, GaAs and related compounds are grown by MBE for nonlinear-optical devices.


Friedrich-Schiller-Universität Jena
Institut für Festkörperphysik
AG Physik Dünner Schichten

Laboratory Astrophysics/Cluster Physics

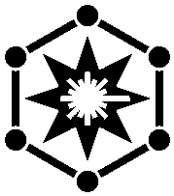

Prof. Dr. F. Huisken

- Cavity ring-down spectroscopy of neutral and ionized polycyclic aromatic hydrocarbons in supersonic jets
- UV spectroscopy of polycyclic aromatic hydrocarbons (PAHs) embedded in liquid helium nanodroplets
- Photoluminescence studies of silicon nanocrystals produced by CO_2 laser pyrolysis and Si ion implantation

The Joint ***Laboratory Astrophysics/Cluster Physics*** Group at the Institute of Solid State Physics results from a cooperation between the Max-Planck-Institute for Astronomy, Heidelberg, and the Friedrich-Schiller-University, Jena. Inaugurated in February 2003, it is conducted by Prof. Dr. Thomas Henning and Prof. Dr. Friedrich Huisken.

The research of the Joint Laboratory Astrophysics and Cluster Physics Group is devoted to fundamental astrophysical questions that can be answered by laboratory experiments, with particular emphasis on spectroscopy. The electromagnetic radiation reaching us from stellar objects is modified in a characteristic manner by interstellar molecules and dust particles. Many of these “fingerprints” are still far from being understood. In order to determine the species causing the modification of the electromagnetic signals detected by telescopes and satellites, comprehensive laboratory studies are urgently needed.

The laboratory is equipped with modern molecular and cluster beam machines as well as laser systems to contribute to the clarification of such fundamental questions. For this purpose, the molecules, clusters, and nanoparticles of interest are prepared in vacuum chambers under conditions coming close to those encountered in the interstellar space (low temperature and low density).

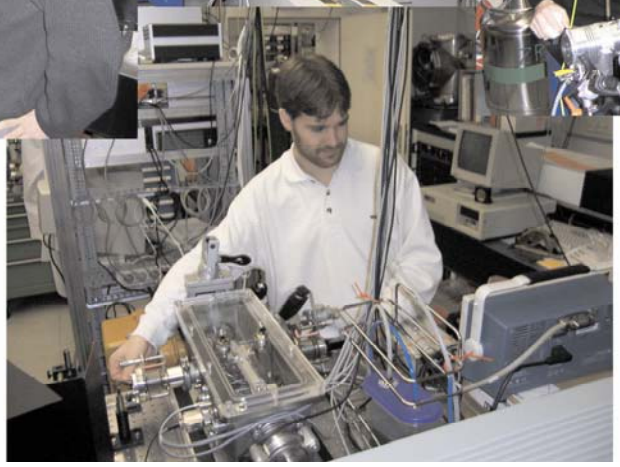

Photoluminescence of epitaxial and polycrystalline $CuInS_2$: A model for intrinsic defect levels

J. Eberhardt, K. Schulz, H. Metzner, J. Cieslak, Th. Hahn, U. Reislöhner, M. Gossla, F. Hudert*, R. Goldhahn*, and W. Witthuhn

Institut für Physik, Technische Universität Ilmenau, PF 100565, 98684 Ilmenau

Both epitaxial and polycrystalline $CuInS_2$ (CIS) layers were deposited by means of molecular beam epitaxy (MBE). The epitaxial CIS layers were directly grown on commercial Si(111) wafers of 100 mm diameter. No ex situ chemical etching or rinsing was performed on these Si wafers; instead, they were cleaned and terminated in a high-temperature sulphurisation step [1]. Polycrystalline films were deposited on untreated Si(100) wafers covered with a sputtered polycrystalline Mo buffer layer of 200 nm thickness. During film growth, the substrates were rotated and kept at temperatures of 820 K for epitaxial and 870 K for polycrystalline CIS, respectively. Following the etching step, low-energy hydrogen implantation into the epitaxial CIS layers was carried out at room temperature. Photoluminescence (PL) was excited by the 514-nm line of a continuous-wave Ar^+-ion laser. More details about the H-treatment and the PL equipment are described elsewhere [2].

Figure 1 shows typical low-temperature PL spectra of low-energy hydrogen implanted epitaxial CIS (curve a) and a KCN-etched polycrystalline layer (curve b) demonstrating strongly different recombination behaviour of both types of the material. The influence of the H-treatment of the as-grown state of epitaxial CIS layers was already discussed [2]. Epitaxial films show defect-related transitions and the PL spectra are dominated by broad luminescence of deep levels. Excitonic luminescence is completely absent for all investigated epitaxial CIS layers. A numerical evaluation with least squares fits and assuming seven transitions of Gaussian shape leads for T = 5 K and 5 mW excitation power to the following transitions: one free-to-bound (FB) transition FB-1 at 1.485(3) eV and six donor-acceptor (DA) transitions at 1.439(3) eV (DA-1), at 1.392(3) eV (DA-2), at 1.349(3) eV (DA-3), at 1.309(3) eV (DA-4), at 1.199(5) eV (DA-5), and at 1.034(5) (DA-6), respectively. In contrast to this, the PL of KCN-etched polycrystalline thin films (curve b) is dominated by excitonic luminescence at 1.527 eV. Furthermore, a donor-to-valence band (BF) transition at 1.465 eV and a DA recombination (1.435 eV) were observed. In order to improve our defect model for CIS

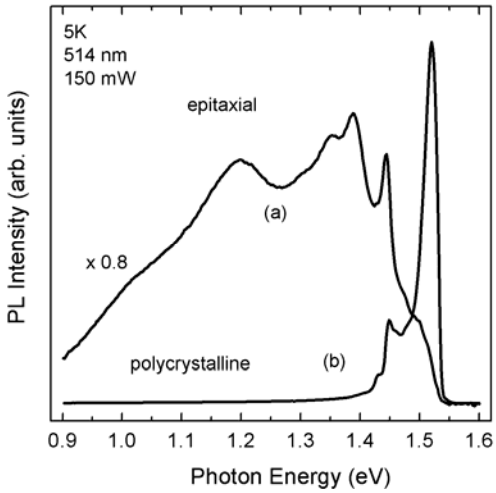

Fig. 1: Comparison of PL spectra of a epitaxial CIS layer after H-treatment (a) and a KCN-etched polycrystalline film (b).

based on earlier data [2], additional investigations on H-implanted epitaxial layers were performed. Figure 2 shows the respective PL spectra over a temperature range from 5 to 100 K. From 5 to 65 K, the temperature step between two spectra amounts to 15 K. With rising temperature, the intensity of DA-1, DA-2, DA-3 and FB-1 decreases and for more than 80 K both DA-2 and DA-3 vanish almost

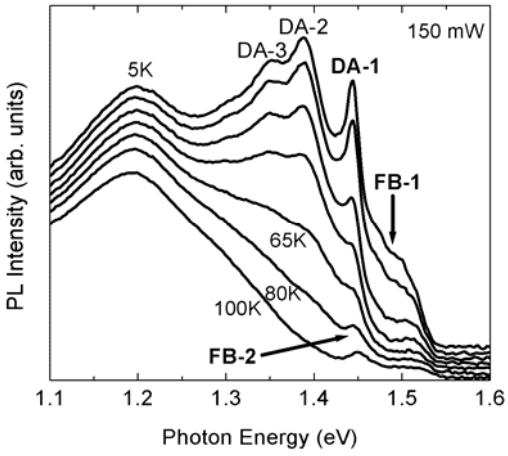

Fig. 2: Temperature dependence of epitaxial CIS after H-treatment.

completely. This behaviour is explained by the complete thermal ionisation of the donors and acceptors at higher temperatures. In contrast to this, DA-1 apparently survives up to high

temperatures. As a result of least squares fits to these data, at low temperatures (5 to 65 K) DA-1 decreases in the same way as DA-2. At higher temperatures it behaves comparable to FB-1. This strongly suggests that there is a second FB transition FB-2 at the energetic position of DA-1. Assuming the same energetic shift for FB-1 and FB-2 with rising temperature, the energetic position of FB-2 at T = 5 K is determined to be 1.436 eV.

In close analogy to the epitaxial films, detailed PL investigations were performed for the polycrystalline material. Figure 3 shows the respective PL spectra at 5 K under variation of the excitation power. The solid lines represent least squares fits to the data assuming six transitions of Gaussian shape. For the minimum intensity of 1.5 mW, the fit yielded 1.435(3) eV,

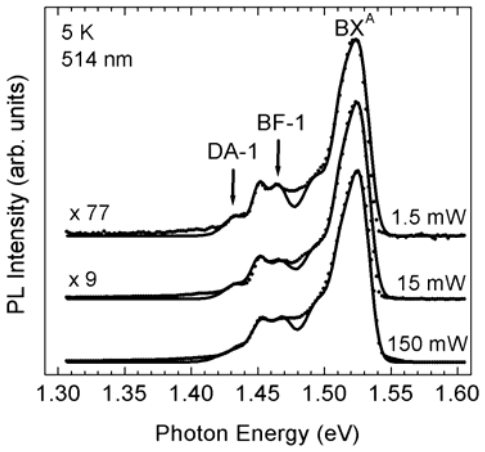

Fig. 3: PL spectra of the polycrystalline sample measured under variation of the excitation power.

1.465(3) eV, and 1.527(3) eV for the peaks denoted by DA-1, BF-1, and BX^A, respectively. In a double logarithmic plot of the respective line intensities as a function of excitation power (not shown here) exponential relations for all transitions are observed. For DA-1, assumed to be a DA transition, the expected sublinear behaviour is observed and the shift of 2 meV per decade under variation of excitation power is typical for DA emissions. The transition denoted as BF-1 shows an almost linear behaviour for the respective line intensity, typical for bound-to-free transitions. An energy shift of 2 meV per decade under variation of the excitation power supports this assumption. BX^A does not show an energy shift with excitation power in accordance with its excitonic nature. Temperature dependent measurements emphasize the excitonic nature of BX^A.

Figure 4 shows the refined defect model for $CuInS_2$ [3]. This model is based on the known band gap of 1.555 eV together with the observed transition energies at T = 5 K with an excitation power of 5 and 1.5 mW for epitaxial and

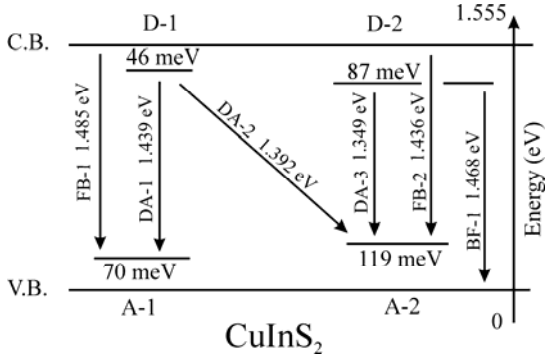

Fig. 4: Defect model for $CuInS_2$ at T = 5 K with two donors and two acceptors based on altogether six different transitions of three different types.

polycrystalline films, respectively. It includes two donors and two acceptors. FB-1 with a transition energy of 1.485 eV gives the shallower acceptor state (A-1) 70 meV above the valence band edge (V.B.). In analogy, FB-2 with 1.436 eV leads to the second acceptor (A-2) 119 meV above the valence band. The shallower donor D-1, found 46 meV below the conduction band edge (C. B.), is determined by the energetically highest DA transition DA-1. We assume that DA-2 is associated with the shallower donor D-1 and a second acceptor A-2. This gives precisely the position of A-2, which is also confirmed by FB-2. The third DA transition DA-3 leads to the second donor state (D-2) 87 meV below the conduction band edge. D-2 is confirmed by BF-1. The model is a self-consistent description of our data from both epitaxial and polycrystalline CIS. That means every defect level is confirmed by at least two different transitions. Altogether six transitions of three different types yield the energetic position of two donor- and two acceptor states.

The authors thank the Stiftung Nagelschneider and the Deutsche Forschungsgemeinschaft for their generous financial support.

[1] H. Metzner, Th. Hahn, J.-H. Bremer, J. Conrad, Appl. Phys. Lett. 69 (1996) 1900.
[2] J. Eberhardt, H. Metzner, R. Goldhahn, F. Hudert, U. Reislöhner, C. Hülsen, J. Cieslak, Th. Hahn, M. Gossla, G. Gobsch, W. Witthuhn, Thin Solid Films 480-481 (2005) 415.
[3] J. Eberhardt, K. Schulz, H. Metzner, J. Cieslak, Th. Hahn, U. Reislöhner, M. Gossla, F. Hudert, R. Goldhahn, W. Witthuhn, Thin Solid Films (2007) in press.

Apparent Doping Profiles in CdTe/CdS Thin Film Solar Cells

U. Reislöhner, M. Hädrich, H. Metzner, and W. Witthuhn

CdTe/CdS thin film solar cells have been fabricated on an industrial scale for several years, with a conversion efficiency of about 8% for large-area modules. A lot of research work has been done in order to increase this moderate efficiency. The doping, especially the shallow one, is essential for the function of the device and knowledge of the doping is necessary for comprehension and interpretation of measurement results. A capacitance-voltage (C-V) measurement is a basic and wide spread method to determine the shallow doping, because it uses the space charge region which is an inherent property of pn-junctions. Therefore, it is applicable to finished solar cells, which have undergone all process steps, and so any further critical preparations are avoided which could influence the device properties due to the measurement.

In our own laboratory we prepared thin film CdS/CdTe solar cells by close space sublimation (CSS) on ITO/SnO_2 coated float glass substrates [1]. The properties of our cells are comparable to those of commercial cells.

Fig. 1 shows the doping profiles of the CdTe layer obtained by C-V measurements and confirms the well known rise in dopant concentration with increasing depth, i. e., with increasing reverse bias, when the usual evaluation procedure is employed [2,3]. However, at 380K, the measured dopant concentration is much higher than at 300K. This result demonstrates that not only shallow level defects, which are completely ionized, contribute to the capacitance, but also a considerable amount of deep centers. We confirmed this conclusion by thermal admittance spectroscopy (for details see [4]).

The usual evaluation of Mott-Schottky-plots takes for granted a totally ionised shallow doping and a negligible amount of deep dopants only. Consequently, the basic requirement for an ordinary interpretation of C-V spectra in terms of a shallow doping profile is not fulfilled. At a higher temperature, a larger fraction of deep centers is ionized or may respond to voltage changes of the probing signal. Deep Acceptors with a band-gap level lying above the Fermi energy are neutral in the bulk, but in the space charge region they may be recharged by the changing band bending during the C-V measurement fast enough to contribute to the capacitance signal. The modulation frequency (here 1MHz) of the probing signal is normally

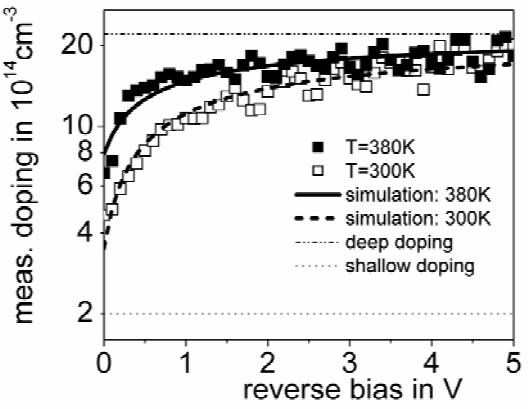

Fig. 1: Doping profiles of the CdTe layer in a CdTe/CdS solar cell obtained by C-V measurements. The simulations are calculated assuming homogeneous profiles of shallow and deep dopants with a higher concentration of deep centers.

too high for the deep centers to be recharged in this rhythm. However, during the C-V measurement the voltage is increased by typically 0.1V steps at a frequency in the order of one step per second. This may be enough time to get ionized for those deep traps which are pushed under the Fermi level due to the increased band bending. The analogous explanation holds for the case of a reversed measurement direction. A small reduction of the reverse bias will push these centers above the Fermi level, changing their charge state from negative to neutral, thereby feigning a reduction of dopant concentration with decreasing reverse bias, even for the case of uniform doping.

Assuming a homogeneous shallow doping and an additional homogeneous deep doping with similar or higher concentration, the profile of ionized centers $N(x_d)$ obtained from a C-V measurement is in this case approximately given by [4,5]:

$$N(x_d) \approx N_s(x_d) + \left(1 - \sqrt{\frac{E_t - E_F}{e(V_D + V)}}\right) \cdot N_t(x_t)$$

where x_d denotes the depletion depth, N_s is the shallow dopant concentration, N_t is the concentration of deep acceptors and x_t is the depth where the deep level crosses the Fermi level, E_t denotes the energy of the deep acceptors above the valence band, E_F is the Fermi energy level

with respect to the valence band, V_D denotes the built-in voltage and V the applied reverse bias, and e is the elementary charge.
Fig. 1 shows the result of a simulation using two deep levels (adding a term for the second deep acceptor concentration N_{t2}). The data used for this simulation are N_s=2·10^{14}cm^{-3}, N_{t1}=4·10^{14}cm^{-3}, N_{t2}=1.8·10^{15}cm^{-3}, E_{t1}=0.4eV, E_{t2}=0.75eV, E_F*(300K)*=0.15eV, E_F*(380K)*=0.4eV, V_D*(300K)*=0.65V and V_D*(380K)*=0.5V.
We note that the spectra for 300K and 380K are described by an identical set of dopant parameters. Their difference exclusively depends on a different Fermi level on account of the different temperatures. This well-fitting combined simulation of two different spectra obtained at different temperatures shows that the result of the C-V measurements is explained by the above described mechanism of recharging deep levels due to slow stepwise change of reverse bias during the C-V measurement.

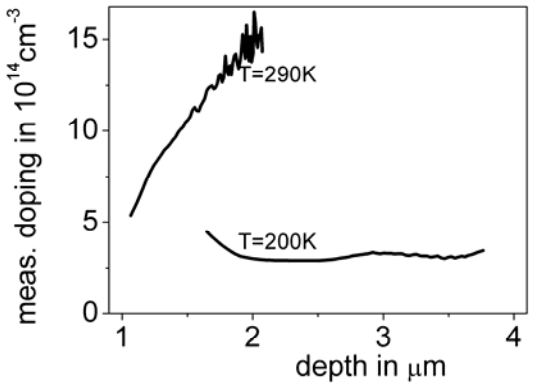

Fig. 2: Doping concentration measured by C-V profiling. At 200K the deep centers are not even able to follow the slow voltage changes during the measurement and the homogeneous shallow doping profile becomes visible.

We do not expect a perfect fit of the simulated function to the measured spectra, because the given equation is only an approximation assuming the changes Δx_t and Δx_d being equal after a change in reverse bias. Further on, the traps may not perfectly respond to the slow voltage change, especially at the lower temperature of 300K. At higher temperatures a rising fraction of traps may also respond even to the high frequency probing signal. These errors explain the quite shallow Fermi level at 300K which is necessary for the simulation. The deep traps can neither follow the high frequency probing signal nor the slow stepwise voltage change when the temperature is sufficiently decreased. Their only contribution is then stemming from those deep levels located nearest to the pn-junction being charged already at zero bias due to the built in potential. In Fig. 2 this residual influence of deep traps is visible in the slightly higher dopant concentration near the junction at 200K. Moreover, only shallow levels are observed and the uniform shallow doping becomes visible. But also C-V measurements at temperatures lying distinctly below 200K will reveal erroneous results, due to an ongoing freeze-out of the shallow doping. Furthermore, a C-V measurement becomes difficult at too low temperatures, because the space charge region already reaches the back contact at small bias values.
The simulation also confirms a rather uniform shallow and deep doping as well as a high electric field near the junction, caused by the deep acceptors being ionized there due to the built in potential. This result on the doping situation is important for the interpretation of other measurements, too. For example, it explains the high electric field near the junction which Köntges [6] had to assume to explain some properties of EQE-spectra (external quantum efficiency).

Acknowledgements
This work was funded by the Bundesministerium für Umwelt, Naturschutz und Reaktorsicherheit (Förderkennzeichen 0329881). We thank Antec Solar Energy for supplying us with commercial samples for the purpose of comparison.

References

[1] M. Hädrich et al., see this report
[2] T. Okamoto, A. Yamada, M. Konagai, Jpn. J. Appl. Phys. 39 (2000) 2587
[3] J. Versluys, P. Clauws, P. Nollet, S. Degrave, M. Burgelman; Thin Solid Films, 431-432 (2003) 148
[4] U. Reislöhner, M. Hädrich, N. Lorenz, H. Metzner, W. Witthuhn; Thin Solid Films, (2007) in press
[5] P. Blood and J. W. Orton, "The Electrical Characterization of Semiconductors: Majority Carriers and Electron States"; ISBN 0-12-528627-9, Academic Press Limited, London, 1992
[6] M. Köntges, Ph. D. Thesis, University of Oldenburg, Germany, 2002

Investigation of the influence of the activation step on CdTe solar cell properties by quantum efficiency measurements

M. Hädrich, S. Mack, H. Metzner, U. Reislöhner, W. Witthuhn

CdTe with a direct band gap of 1.45eV is a very suitable absorber material for thin film solar cells. It grows p-type and highly stoichiometric forming a heterojunction with n-type CdS. Various deposition techniques using float glass substrates allow low-cost large-scale production [1]. The highest conversion efficiencies of about 16% for laboratory cells have been obtained using close space sublimation (CSS) [2]. As the efficiencies of industrial modules are still less than 10%, improving CdTe thin film technology is essential.

We investigated the influence of different manufacturing steps on the properties of CdTe solar cells. A crucial step is the activation of the layer system which is performed by thermal annealing in the presence of a chlorine compound. This step is assumed to cause grain growth, doping and an intermixing at the interface between CdS and CdTe [3]. To quantify the intermixing, we used external quantum efficiency (EQE) measurements of complete solar cells to determine the sulphur fraction x in $CdTe_{1-x}S_x$.

The cells were produced in our own baseline using 10x10cm^2 substrates of commercially available TCO coated float glass. For CdS and CdTe layer deposition we used the CSS technique. For the activation, we employed a wet chemical treatment with $CdCl_2$ solution prior to annealing or alternatively an anneal in HCl gas ambient, applied a standard etching procedure with nitric and phosphoric acid and used molybdenum as back contact material. Galvanically isolated solar cell areas and the front contact were then structured by scribing. The sulphur fraction was determined indirectly from bandgap measurements by EQE. The bandgap energy was thereby obtained by extrapolating the linear part of the long wavelength absorption edge in a $(EQE*h\nu)^2$ versus $(h\nu)$ plot to the intersection with the photon energy $h\nu$ axis [4]. The sulphur fraction of the $CdTe_{1-x}S_x$ compound was determined by inserting the measured bandgap energy values of the respective finished solar cells into a known empirical $E_G(x)$ curve , as shown in Fig. 1. The function describing that curve is [5]:

$$E_G(x)=2.4x+1.51(1-x)-1.8x(1-x).$$

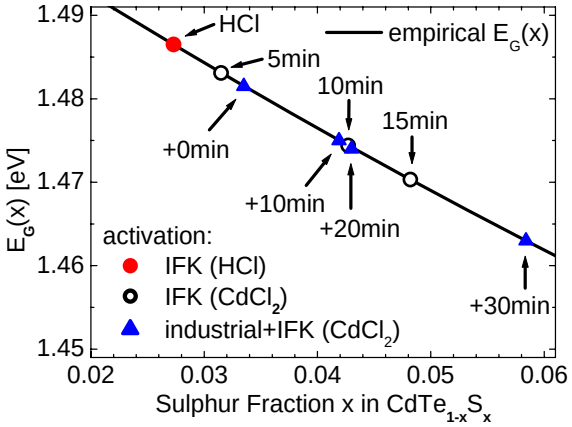

Fig.1: Change of sulphur fraction and bandgap energy of $CdTe_{1-x}S_x$ as a result of the activation step. Activation times are as indicated.

Values of x between 0.2 and 0.8 cannot be reached because of the miscibility gap in the phase diagram [5]. The experimental setup for the EQE measurements is shown in Fig. 4.

The comparison of our own (IFK) solar cells activated with $CdCl_2$ for different annealing times clearly shows a bandgap energy decrease with activation time (see Fig. 1). According to the $E_G(x)$ plot, this is due to a rise of the sulphur fraction and therefore due to stronger intermixing. The best solar cell efficiency of 8% was obtained for a 5min anneal which led to a low sulphur fraction of about 0.03. For longer activation times, the efficiency declined. A sample treated with gaseous HCl anneal, also with a sulphur fraction of 0.03, reached 8% efficiency.

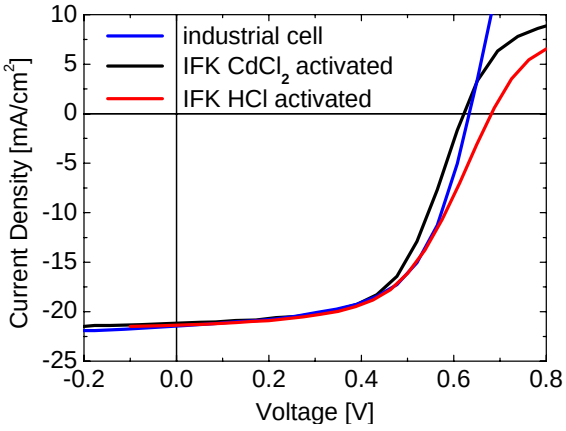

Fig.2: Current-voltage characteristics of an industrial cell and differently activated cells from our baseline.

For comparison, we applied additional activation with different annealing times to already activated industrial solar cell layers (from Antec Solar Energy, Arnstadt/Germany). The increase of the sulphur fraction and decrease of the bandgap with activation time is also visible for these samples. For the 30min annealed sample, the sulphur fraction rose to almost 0.06 which is about the solubility limit [5]. The as-manufactured sample (0min additional activation) had a low sulphur fraction of about 0.03 and 8% efficiency again. In Fig. 2, the current-voltage characteristic of this industrial cell is compared to those of HCl or 5min $CdCl_2$ activated cells from our baseline, respectively, as referred to in Fig. 1. All cells having equal sulphur fractions yield similar characteristics. The turning point for our cells is presumably explicable by an undesired back contact barrier.

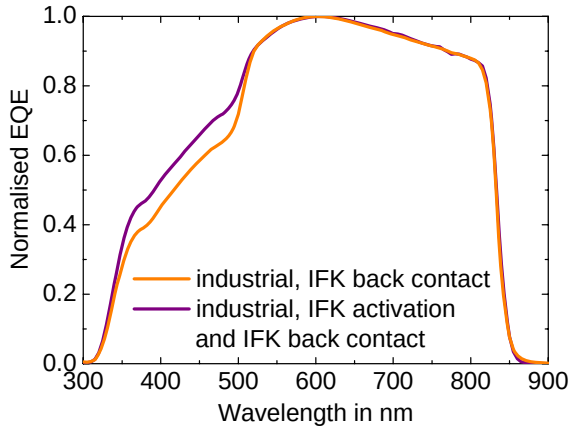

Fig. 3: Normalised EQE spectra of industrial cells with / without additional activation, both with IFK back contact.

In the EQE spectrum, the effect of intermixing is also visible in the short wavelength region. In Fig. 3, the normalised spectra of industrial cell layers with our back contact, one of that had been subjected to additional activation, are shown. The higher EQE below 500nm wavelength for the latter implies that the CdS buffer layer is getting thinner, increasing the absorption in CdTe. This effect can be beneficial for the efficiency because of a higher photocurrent. However it is detrimental if the CdS layer is consumed too far or even completely because of shunts.

Our measurements imply that good solar cell properties can be obtained when the activation step results in moderate intermixing of CdS and CdTe at the interface. For the best results, the sulphur fraction was in the order of 0.03. Using HCl gas activation, similar results like in the wet chemical $CdCl_2$ process were achieved.

[1] Bonnet, P. Meyers., J. Mater. Res. 13 (1998) 2740.

[2] X. Wu, J.C. Keane, R.G. Dhere, C. DeHart, D.S. Albin, A. Duda, T.A. Gessert, S. Asher, D.H. Levi, P. Sheldon, Proc. of the 17th Europ. Photov. Sol. En. Conf., Munich, Germany, 2001, p. 995.

[3] M.H. Aslan, W. Song, J. Tang, D. Mao, R.T. Collins, D.H. Levi, R.K. Ahrenkiel, S.C. Lindstrom, M.B. Johnson, Mat. Res. Soc. Symp. Proc., vol. 485, AIP press, 1998, p. 203.

[4] J. Kessler, D. Schmid, R. Schäffler, H.W. Schock, S. Menezes, Conf. Rec. 23rd IEEE Photov. Spec. Conf., New York, 1993, p. 549.

[5] G. Jensen, Alloys in Cadmium Telluride Solar Cells, Stanford University, 1997.

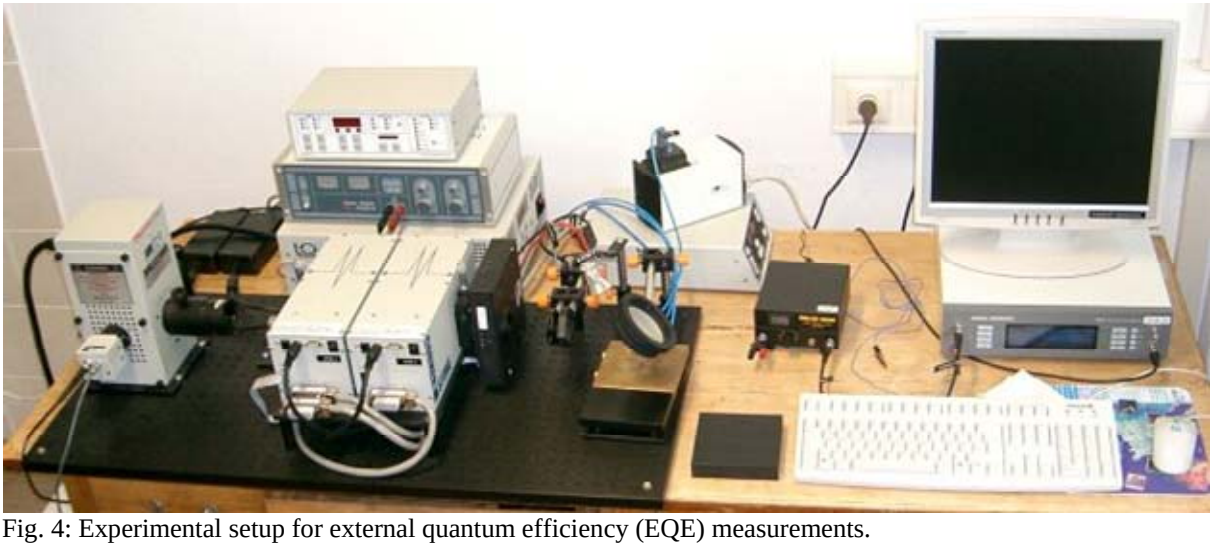

Fig. 4: Experimental setup for external quantum efficiency (EQE) measurements.

Twinning in epitaxial $CuIn_{1-x}Ga_xS_2$ on Si(111)

J. Cieslak, Th. Hahn, H. Metzner, U. Reislöhner, J. Eberhardt, W. Witthuhn

In recent works [1,2,3], successful epitaxy of the chalcopyrite semiconductor $CuIn_{1-x}Ga_xS_2$ $(0 \le x \le 1)$ (CIGS) on Si(111) was demonstrated. Structural investigations gained detailed information about the lattice parameters and the occurrence of metastable structure variants. High resolution transmission electron microscopy (HRTEM) images show a distinct tendency to twinning in epitaxial CIGS films (fig. 1).

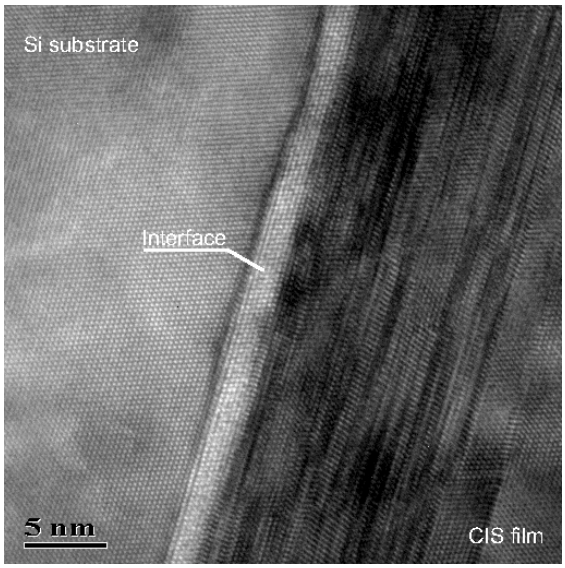

Fig. 1 HRTEM image of epitaxial $CuInS_2$ (CIS) film on Si(111)

Due to the very extensive sample preparation, HRTEM is unsuitable for systematic investigations. However, since the growth of epitaxial CIGS thin films is monitored routinely by means of reflection high energy electron diffraction (RHEED), we developed a method for a quantitative analysis of twinning in epitaxial chalcopyrite thin films on Si(111) substrates from RHEED patterns after growth. Figure 2 and fig. 3 depict RHEED images of two epitaxial CIGS films with different gallium content x. Both images show reflections mirrored by the imaginary line formed by the reflections {000}, {112} and {224}. In fig. 3, some twin reflections are marked by arrows. The ratio of the intensities of the twin and origin reflection we call the degree of twinning T $(0 \le T \le 1)$.

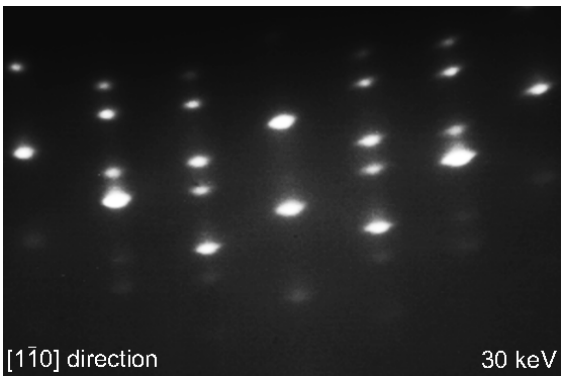

Fig. 2 RHEED pattern of a CIGS film (x=0.41) with high degree of twinning

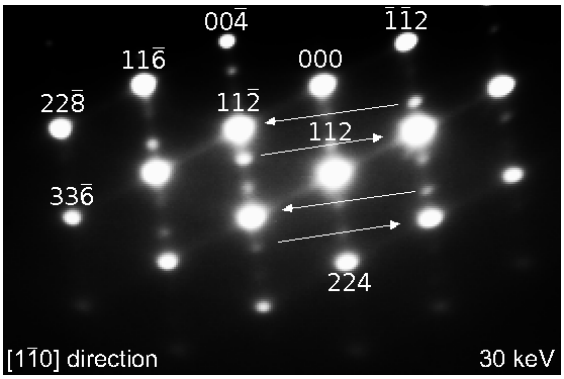

Fig. 3 RHEED pattern of another CIGS film (x=0.75) of low degree of twinning

The comparison of the reflection patterns in fig. 2 and fig. 3 shows, that the degree of twinning varies from film to film. Of course, an analysis of the values reveals two accumulation points at $T = 0.91$ and $T = 0.25$. So, a statistical reason for the variation is less likely. The investigation of other film parameters at the accumulation points leads to a systematic relation between the film composition and the degree of twinning. Figure 4 depicts the dependence of T on the gallium content of the epitaxial films. Films of low and medium Ga content are highly twinned and Films of high Ga content exhibit only low degrees of twinning. The transition between both ranges of film compositions at $x = 0.74$ is very sharp. The developing of the values can be modelled using the Heaviside function $\Theta(x)$:

$$T(x) = 0.91 \cdot \Theta(0.74 - x) + 0.25$$

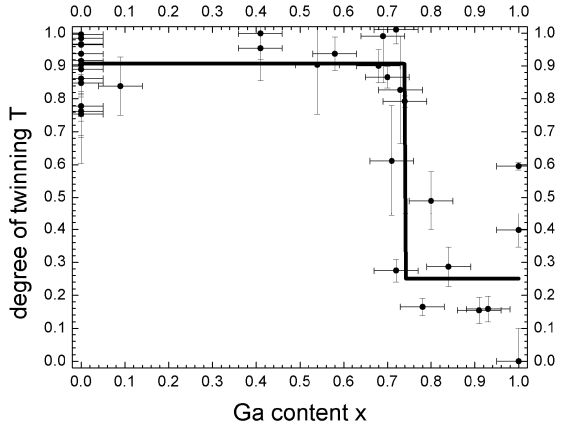

Fig. 4 Nonlinear dependence of the degree of twinning on the gallium content

The reflection patterns show, that the epitaxial films are twinned concerning {112} lattice planes. These lattice planes have a stacking ABCABC (type I) or CBACBA (type II). The sequel of both types of stacking (ABCBA) leads to a {112} twin boundary. It must be pointed out, that at least three planes (BCB) are necessary to form a {112} twin boundary. So, next but one neighbour interactions determine the correct stacking. Thus, {112} twin boundaries can form easily during film growth and are comparatively stable. The abutting of different stacked domains leads to other twin boundaries. Due to a gap at the twin boundary, illustrated by the example of the $(\bar{1}\,\bar{1}\,4)$ twin boundary shown in fig. 5, these ones are substantial more unstable than {112} twin boundaries. However, vacancies and lattice mismatch concerning the substrate are able to stabilize this kind of twin boundaries.

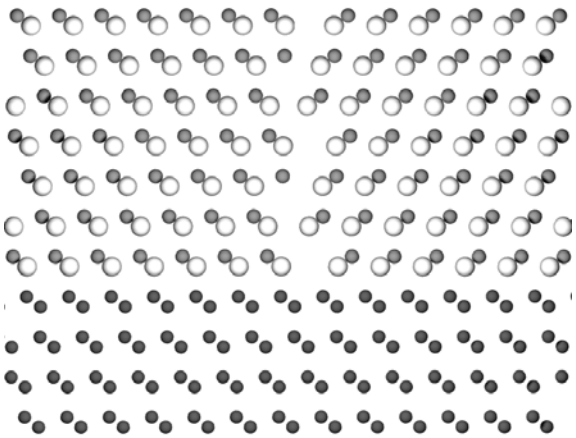
Fig. 5 surface of a CIGS(112) plane on Si(111) observed in [-1 1 0] direction;
bottom: Si substrate;
top left: type I stacked CIGS film;
top right: type II stacked CIGS film

From this consideration, a dependence of the degree of twinning on the lattice mismatch is expected. The lattice mismatch shows linear dependence on the gallium fraction [1], but the degree of twinning follows a Heaviside function. Thus, no correlation between these parameters can be found.
Although twinning is a common phenomenon [4,5,6,7], its suppression is preferable to increase the crystal quality of the epitaxial layers. By the example of the epitaxial system CdTe on GaAs, the usage of miscutted substrates has led to untwinned CdTe layers [8]. However, the Si(111) substrates used in this work already have an off-cut of 4°, but only films with high gallium fractions show a low degree of twinning. Possibly, higher miscuts could lead to an improvement concerning the suppression of twinning.

In conclusion, epitaxial CIGS layers on Si(111) show, dependent on their gallium fraction, different degrees of twinning. The curve can be described by a step function. The twinning always takes place concerning {112} lattice planes.

References

[1] H. Metzner et al., Apll. Phys. Lett. 83 (2003) 1563
[2] J. Cieslak et al., J. Phys. Chem. Solids 64 (2003) 1777
[3] T. Hahn et al., Appl. Phys. Lett. 88 (2006) 171915
[4] K. Oishi et al., J. Cryst. Growth 177 (1997) 88
[5] K. Oishi et al., J. Phys. Chem. Solids 64 (2003) 1835
[6] J. Alvarez-Garcia et al., Phys. Rev. B 71 (2005) 054303
[7] R. Hunger et al., Thin Solid Films 361-362 (2000) 437
[8] E. Ligeon et. al., J. Appl. Phys. 67 (1990) 2428

On the origin of strains in epitaxial $CuInS_2$ thin films

Th. Hahn, H. Metzner, J. Cieslak, J. Eberhardt, U. Reislöhner, K. Schulz,
M. Oertel and W. Witthuhn

Strains and stresses are very common phenomena in thin film technologies and are frequently found to have a major impact on the properties of thin films and devices. These influences can be beneficial, such as an increased carrier mobility in strained SiGe-layers or an enhanced hardening of tool coatings, however, more often one encounters restrictions in the deposition of thin films or degradations of thin film properties by the occurrence of strains. Most fatal are for example adhesion problems, where compressive or tensile strains lead to a peeling off or cracking of layers, respectively, or the formation of hillocks [1].

As far as the origins of residual strains in thin films are concerned, they can generally be divided into internal stresses generated by the film material itself as by recrystallizations or the formation of precipitates and stresses introduced by an interaction with the substrate via different lattice constants or a mismatch of the thermal expansion coefficients.

In case of $CuInS_2$ (CIS) grown epitaxially on Si-substrates, there is a considerable lattice mismatch of 1.7% and 2.4% for the *a*-axis and *c*-axis, respectively. So, for pseudomorphic growth of CIS on Si a compressive strain due to the smaller lattice constant of Si as compared to CIS has to be expected. Compared to these values, the stresses introduced upon cooling down from the deposition temperature due to different thermal expansion coefficients are smaller by almost an order of magnitude and are of tensile nature, since the linear thermal expansion coefficients of CIS are greater by a factor of 4 as compared to the one of Si [2-4].

Another important property of CIS is the easy formation of polytypes. Since the formation energy for the metastable CuAu-type structure of CIS is only 2meV/atom higher as compared to the ground state chalcopyrite structure, a crystallization of CIS in the metastable CuAu-type structure is very likely, as predicted theoretically and found experimentally [5,6]. However, since the crystal structures of the ground state chalcopyrite and metastable CuAu-type orderings are not congruent at all, instead being quite different as far as tetragonal distortions

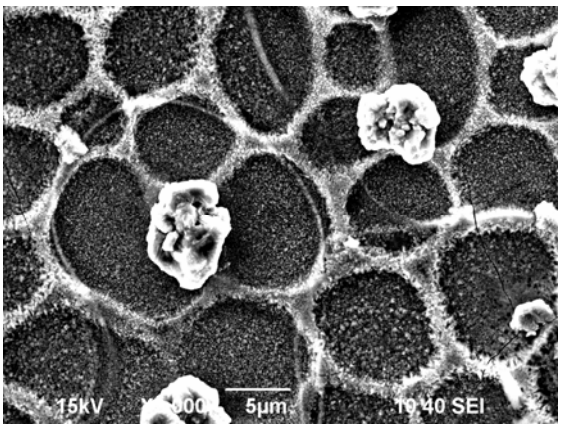

Fig. 1. SEM picture of ridges and hillocks in an epitaxial chalcopyrite thin film on Si (111). Here, compressive stresses are relieved by a transport of film material to form ridges and hillocks (preferably at triple junctions of ridges). So the dominating stresses in chalcopyrite thin film growth are of compressive nature. Additional tensile strains due to different linear thermal expansion coefficients of CIS and Si lead upon cooling down to additional cracks in the film.

are concerned [7], a coexistence of these two types of orderings, either through the incomplete recrystallization of one type into the other or through the competitive crystallization of both types during growth, leads to considerable residual strains. Indeed, earlier works showed, that the dominating ordering type in CIS epitaxial thin films imposes large strains on the minor ordering type [7,8].

As a third source of strains, binary precipitates have to be considered for CIS thin films, since these materials are normally grown with a Cu-rich composition, with the Cu-surplus segregating in Cu_xS-phases. For high-quality CIS thin films, these precipitates predominantly form as liquid phases on the surface of the film during growth [9], while any additional remains of Cu_xS inside the film leads to stresses of compressive nature for the host material [10].

As a most drastic manifestation of strains in epitaxial CIS thin films on Si, the formation of ridges and hillocks can take place, as depicted in Fig. 1 [11]. While in metallic layers, the mismatch of the linear thermal expansion coefficients between layer and substrate are often

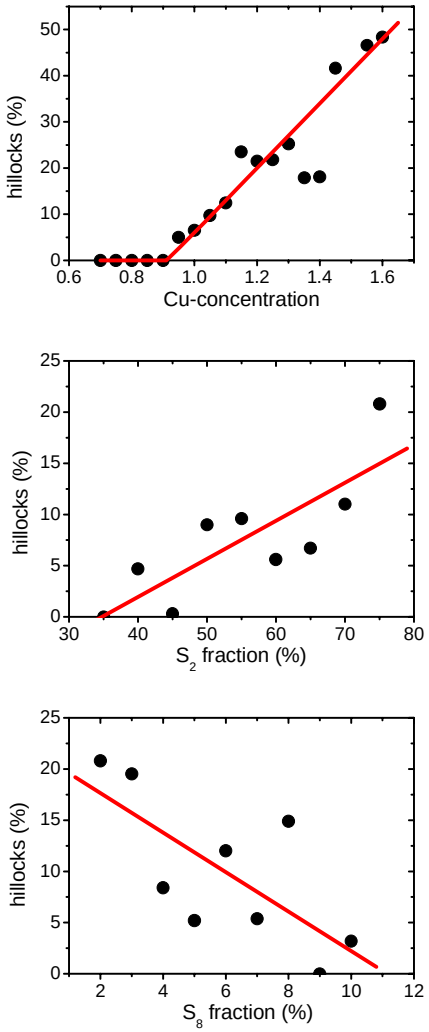

Fig. 2. Fraction of film material crystallising in hillocks as a function of Cu-surplus and composition of the S-beam during deposition.

responsible for hillock growth, for CIS on Si we must exclude the hillocks being due any interaction of the CIS with the substrate, since the lattice mismatch is compensated in this material system via dislocations at the interface [6], while the mismatch of the linear thermal expansion coefficients lead to tensile strains in the epilayer as opposed to the compressive ones needed for hillock formation. For a determination of the dominating mechanism responsible for strains in CIS thin films, segregations or the coexistence of polytypes, a closer look on the dependence of stress-related phenomena as a function of deposition parameters shows to be quite illustrative. In Fig. 2 the average amount of film material nucleated in hillocks is plotted as a function of the Cu-content of the layer and of the composition of the S-Beam during growth as generated by a cracker source. Here, a clear dependence of hillock formation on the Cu-content is found. While hillock-growth is completely absent in Cu-poor samples, the formation sets in as soon as the Cu-content crosses the point of stoichiometry. Thus, it is concluded, that Cu_xS-precipitates inside the CIS layer imposes the strains responsible for the formation of hillocks during film growth. An additional influence is found via the composition of the S-Beam. While a large fraction of reactive S-species (S_2) favours hillock formation, large S-molecules (S_8) seem to favour the segregation of excess Cu_xS on top of the film, reducing stress inducing precipitates inside the layer.

In conclusion, a rather complex scenario for the causes and effects of strains in CIS on Si is obtained. A segregation of excess Cu via binary Cu_xS inside the layers leads to large compressive stresses, which are released during film growth through the migration of film material along grain boundaries and give rise to the formation of hillocks. Residual strains of compressive as well as tensile nature are additionally introduced inside the samples, if the coexistence of metastable orderings occurs [7,8]. Finally the mismatch of the linear thermal expansion coefficient results in tensile stresses upon cooling down from the deposition temperature which can lead to additional cracks in the film.

Acknowledgements

J. Heindl (JEOL Germany) is thanked for the SEM picture. This work was supported by the *Deutsche Forschungsgemeinschaft* .

References

[1] Milton Ohring, Materials Science of Thin Films – Deposition & Structure, 2nd Edition, Academic Press, San Diego (2002).
[2] Th. Hahn et al., Appl. Phys. Lett. **72**, 2733 (1998).
[3] G.C. Bahr and L.K. Samanta, Phys. Rev. **B 26**, 2275 (1982).
[4] S.M. Sze, Physics of Semiconductor Devices, John Wiley & Sons, New York (1981).
[5] S.-H. Wei et al., Phys. Rev. **B 45**, 2533 (1993).
[6] Th. Hahn et al., Thin Solid Films **387**, 83 (2001).
[7] Th. Hahn et al., Appl. Phys. Lett. **88**, 171915 (2006).
[8] J. Cieslak et al., Phys. Rev. B, submitted.
[9] R. Scheer et al., Appl. Phys. Lett. **63**, 3294 (1993).
[10] C. Guillén and J. Herrero, phys. stat. sol (a) **203**, 2438 (2006).
[11] Th. Hahn et al., Jahresbericht des IFK 2005.

Europium Induced Deep Levels in Hexagonal Silicon Carbide

G. Pasold[1], C. Hülsen, F. Albrecht[2], R. Sielemann[3], W. Witthuhn

[1] *TRW Switzerland GmbH, Feldstrasse 1, CH-6301 Zug, Swiss*
[2] *Infineon Technologies Dresden, Königsbrücker Straße 180, D-01099 Dresden, Germany*
[3] *Hahn-Meitner-Institut Berlin, Glienicker Straße 100, D-14109 Berlin, Germany*

Introduction

The typical thermal quenching of the rare earth luminescence in semiconductors decreases with increasing band gap energy, which has been shown already for GaN and SiC [1-2]. For a detailed understanding of the luminescence mechanism the characterization of the elemental related band gap states is a basic requirement.
The studies on the SiC band gap influenced by a Gd-parent isotope [3] revealed increasing DLTS signal amplitudes, indicating the existence of deep levels of Eu appearing as daughter isotope. Based on this increase alone the assignment to Eu is by no means straightforward and can be falsified due to preceding decay effects. Therefore in additional investigations the deep level correlation with Eu impurities was studied by implantation of radioactive ^{146}Eu and ^{147}Eu isotopes as parent activities.

Experiment and results

N- as well as p-type epitaxial layers of 4H- and 6H-SiC grown by Cree Inc. on heavily doped (5×10^{18} cm^{-3}) substrates were investigated. The net shallow doping concentrations of the epitaxial layers were confirmed by means of capacitance-voltage profiling ranging between 1 and 8×10^{15} cm^{-3}.

The recoil implantations [4] of radioactive Eu-isotopes were carried out at the ISL Cyclotron of the Hahn-Meitner-Institute in Berlin applying the nuclear reactions ^{139}La(^{12}C,5n)^{146}Eu and ^{139}La(^{12}C,4n)^{147}Eu. γ-ray spectroscopy on each sample revealed the recoil implanted isotope ratio of ^{146}Eu and ^{147}Eu to be in the ratio of 1:2. Both isotopes follow their decay chain directly to Samarium. The DLTS measurements were performed by a commercial DLTS system on Schottky contacts prepared on the doped samples.

p-type SiC: Figure 1 (a) shows DLTS spectra of a p4H-SiC sample implanted with the radioactive isotopes. The decrease of the signal labelled 'pEuI' is best resolved in a signal-difference spectra shown in figure 1 (b). The analysis of this 'pEuI'-signal revealed an activation energy of $E_T=E_V+0.86(2)$ eV. The relation of that DLTS-signal to Europium is nearly impossible by conventional DLTS-experiments demonstrating the power of the applied

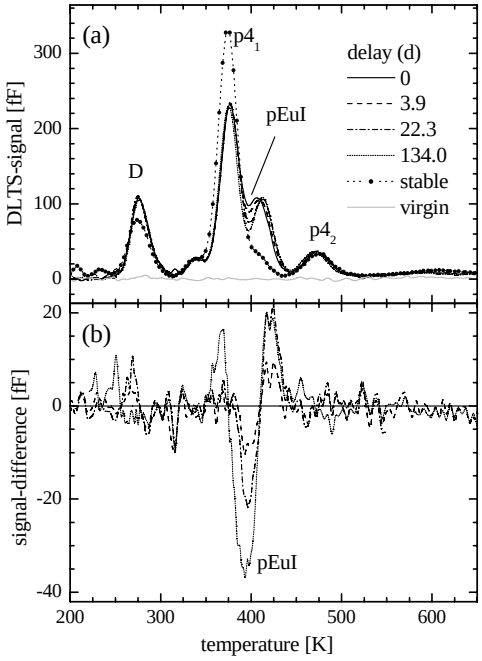

Fig. 1: (a) DLTS spectra of ^{146}Eu, ^{147}Eu and ^{153}Eu (stable) implanted p-type 4H-SiC recorded during the elemental transmutation to stable Sm. (b) signal-difference spectra from (a).

radiotracer-concept.
The signals labelled D, $p4_1$ and $p4_2$ are related to radiation induced levels found already in similar experiments on p-type SiC.

A similar scenario could be found for p6H-SiC implanted with radioactive Eu: a DLTS-signal around 390 K decreases in the spectra. The corresponding level parameters are deduced to $E_T=E_V+0.88(2)$ eV.

n-type SiC: The spectra taken on n4H-SiC samples implanted with the Eu isotopes yield unambiguously an additional Europium-correlated state in the upper part of the band gap by means of the decreasing behaviour of its DLTS signal amplitude.

For 6H-SiC we observed two Eu-correlated states at 0.29(2) eV and 0.67(2) eV, respectively, below the conduction band. The corresponding DLTS-difference spectra are shown in figure 2. The figure shows the signal differences recorded during elemental transmutations: Whereas part (a) is dominated by the decay of the Eu-parent isotopes, part (b) shows increasing signals recorded during the $^{149}Gd \rightarrow {}^{149}Eu$ transmutation reported earlier [3].

A comparison of the implanted isotope dose and the measured concentration of the deep levels allows an estimation of the degree of the electrical activation of Eu in all SiC-samples investigated to about 10 % with an uncertainty of a factor of two.
The agreement of the Eu-level energies in both p-type materials validate the energetically alignment of the valence bands of the SiC polytypes, reported earlier [5]. Also, the near band states in the two n-type polytypes coincide nearly perfect taking into account the conduction-band off-set of 0.22 eV [5] between the 4H- and 6H-SiC.

The microscopic structure as well as an involvement of additional impurities or defects in the Europium-correlated centers presented here cannot be clarified.
Increasing DLTS signals (potentially correlated with the daughter element Samarium) could not be detected.

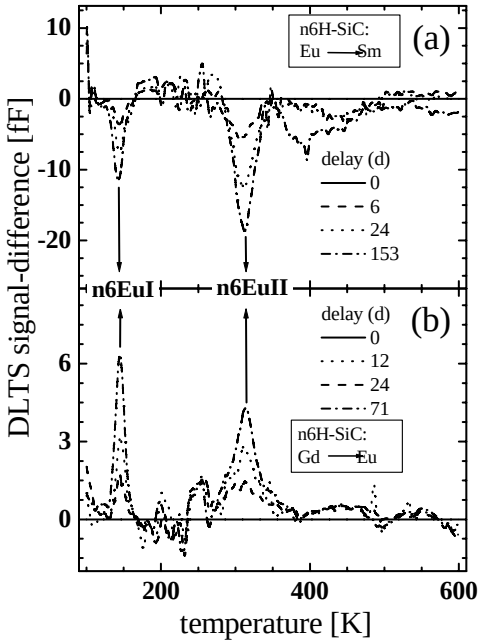

Fig. 2: DLTS-difference spectra of Europium-doped n6H-SiC recorded during elemental transmutations: (a): the ^{146}Eu-^{147}Eu-mixture decays to stable Sm. (b): ^{149}Gd transmutes to stable Eu (for experimental details see ref. [3]).

The work was partially funded by the BMBF and the DFG.

References

[1] A.J. Steckl, J.M. Zavada: MRS Bulletin (9/1999), p. 34 .
[2] Y. Shishkin, W.J. Choyke, R.P. Devaty, N. Achtziger, T. Opfermann, W. Witthuhn: Mater. Sci. Forum **338-342** (2000), p. 639 .
[3] G. Pasold, F. Albrecht, C. Hülsen, R. Sielemann and W.D. Zeitz, W. Witthuhn: Mater. Sci. Forum **457-460** (2004), p. 783 .
[4] N. Achtziger and W. Witthuhn: Silicon Carbide: Recent Major Advances, edited by W.J. Choyke et. al., Springer (2004), p. 537 .
[5] J. Grillenberger, N. Achtziger, G. Pasold, W. Witthuhn: Mater. Sci. Forum **389-393** (2002), p. 573 .

Modelling of ion track formation in swift heavy ion irradiated InP

W. Wesch, A. Kamarou, E. Wendler, A. Undisz, M. Rettenmayr**

Institut für Materialwissenschaft und Werkstofftechnologie

We have previously shown that for electronic energy depositions above ≈ 13 keV/nm swift heavy ion irradiation of InP single crystals leads to the formation of amorphous tracks which accumulate to an amorphous layer in the region of dominating electronic energy deposition with increasing ion fluence ([1] and references therein). The efficiency of damage formation depends on ion mass, ion energy and irradiation temperature. This is illustrated in Fig. 1 which shows the relative concentration of displaced lattice atoms, n_{da}, determined from RBS spectra, as a function of the ion fluence for room temperature (RT) and liquid nitrogen temperature (LNT) irradiations.

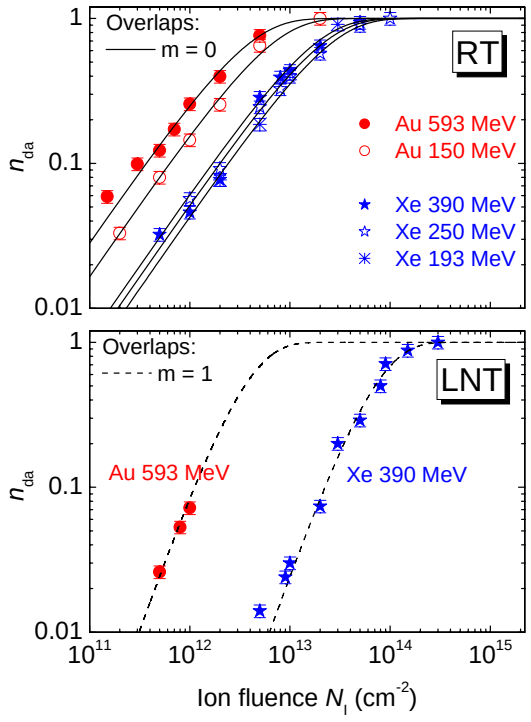

Fig. 1 Fluence dependences of the relative concentration of damage n_{da} formed in InP due to irradiation with fast Xe or Au ions either at RT (the upper part) or at LNT (the lower part). The fitting curves within the Gibbons overlap damage model are also shown as solid or dashed lines.

The analysis of the data in the framework of the overlap damage model introduced by Gibbons [2] shows that at RT obviously each ion produces an amorphous track (overlap number m = 0), whereas at LNT one overlap is necessary to create a track, i.e. predamage is required for the local formation of amorphous material. Although the electronic energy deposition per ion and unit path length is equal for 150 MeV Au and 193 MeV Xe irradiation (ε_e = 18.6 keV/nm), the $n_{da}(N_I)$ curves differ for the two cases indicating that no absolute correlation exists between the value of ε_e and the resulting efficiency of damage formation. Thus, not only the value of ε_e is important, but also the radial distribution of ε_e around the ion path which is determined by the ion velocity.

Because both RBS and TEM (not shown) results showed that the irradiation temperature significantly influences the damage formation, the processes of track formation must be of thermal nature. That means that neither Coulomb explosion nor lattice relaxation mechanisms can explain the experimental results obtained. Therefore the thermal spike (TS) mechanism is used for the description. This mechanism suggests that the deposited energy is transferred to the lattice atoms via electron-phonon coupling. If the resulting atomic temperature reaches the melting point, the material can melt locally and the following cooling can freeze in the disorder and thus leave an amorphous track behind. For the calculations the TS formalism successfully used to describe track formation in insulators and metals (see e.g. [3]) was modified for semiconductors introducing a more correct description of the first stage of track formation (ionisation spike). This includes the calculation of number, energy spectrum and radial distribution of electrons detached from all electronic shells near the ion path. Furthermore, the radial distribution of the

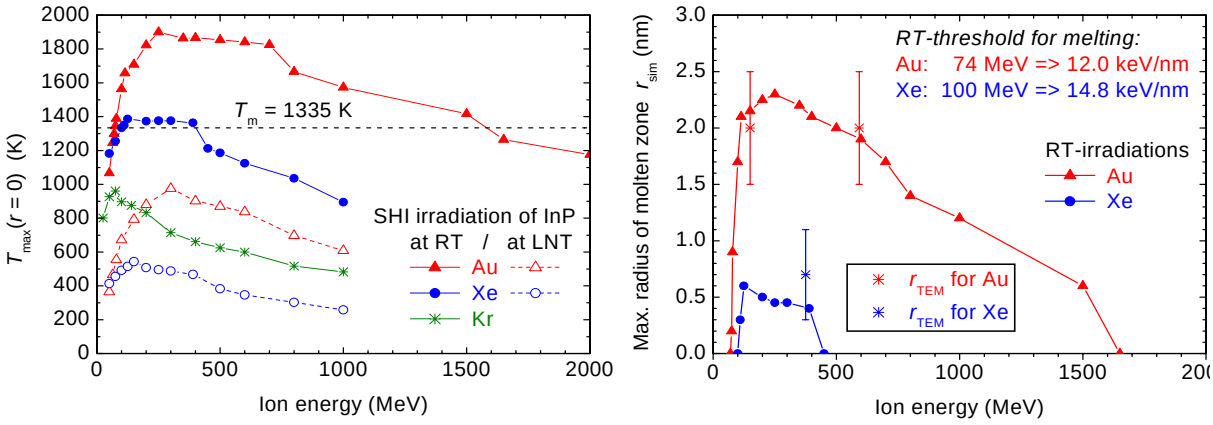

Fig. 2 (left) Dependence of the maximum atomic temperature at the ion track axis ($r = 0$) on the ion energy for various ion species. The data are presented for both RT- and LNT-irradiations. The dashed line corresponds to the melting point of InP (1335 K) [8]. (right) Dependence of the maximum radius of the molten zone, r_{sim}, on the ion energy for various ion species [8]. The data are shown solely for RT-irradiations. The "low-energy" RT-thresholds for melting are presented. Data points obtained from TEM for 150 MeV Au, 593 MeV Au and 390 MeV Xe are also shown for comparison

deposited energy density in a semi-empirical form given in [4] was used (for details see [5]). With this modified TS model the maximum temperature in the centre of the track, T_{max}, and the maximum radius of the molten zone, r_{sim}, were calculated as a function of the ion energy for the different irradiations of InP (Fig. 2). The only unknown parameter in the electron-phonon coupling efficiency, the mean free time between two collisions of an electron with lattice atoms at a certain temperature of the electronic system, T_e, was determined from the experimental data (see [5]).
One can see in Fig. 2 (left) that at RT in a certain energy range of Xe and Au ions the lattice temperature exceeds the melting point of InP. But this is not the case for Kr irradiations and for all irradiations at LNT. This explains well why for equal ion fluences much less damage is created at LNT than at RT (Fig. 1). The maximum radii of the molten zones vary with ion mass and energy (Fig. 2, right). Further, there appear both low- and high-energy thresholds for local melting, and the low-energy threshold for melting and track formation at RT which is the only measure commonly used in the literature is different for different ion species. For lighter ions its value is higher than for heavier ones. Therefore, no universal threshold for track formation exists for InP, and this is assumed to be valid also for other materials. It is furthermore to be seen that the track radii measured by TEM included in Fig. 2, right, are in a good agreement with the results of the calculation.
The results show that the modified TS model successfully describes track formation and damage accumulation in the binary semiconductor InP. Work on description of track formation in other semiconductors is in progress.

Work supported by the Deutsche Forschungsgemeinschaft (DFG) under project no. WE 1707/8-1.

References

[1] W. Wesch, A. Kamarou, E. Wendler, Nucl. Instr. and Methods B 225 (2004) 111.
[2] J.F. Gibbons, Proc. IEEE 60 (1972) 1062.
[3] M. Toulemonde, C. Dufour, E. Paumier, Phys. Rev. B 46 (1992) 14362.
[4] A. Chatterjee, H.J. Schaefer, Radiat. Environ. Biophys. 13 (1976) 215.
[5] A. Kamarou, W. Wesch, E. Wendler, A. Undisz, M. Rettenmayr, Phys. Rev. B 73 (2006) 184107.

Waveguide barriers with adjustable refractive index produced in KTP by irradiation with He- and Li-ions

F. Schrempel, Ch. Beeker, J. Fick [1], W. Wesch

[1] Laboratoire de Spectrometrie Physique, Universite Joseph Fourier Grenoble, St. Martin d'Heres, France

The irradiation of $KTiOPO_4$ (KTP) with energetic ions decreases the refractive index in the depth region of high nuclear energy deposition and, as a consequence, a waveguide barrier with a very sharp refractive index gradient is formed. Typically, the waveguide barrier is established as an amorphized layer having a refractive index decrease by almost 8%. Hence, for a given wavelength and refractive index difference, the width of the waveguide is the only free parameter to adjust the number of the guided modes. Since the dimension of a waveguide is generally specified by technological requirements, the refractive index preferably should be adjustable.

Z-cut KTP single crystals were irradiated with 20 and 300 keV He- and 1 MeV Li-ions, respectively. The irradiation was done at ion fluences in the range of 1×10^{14} to 2×10^{16} cm^{-2}. To investigate the damage accumulation, Rutherford Backscattering Spectrometry (RBS) in channeling configuration was applied. Figure 1 shows the RBS spectra of KTP irradiated with 1 MeV Li-ions. The maximum depth of displaced atoms is 2.4 µm and, therefore, the strong overlapping of the RBS-yields from elements in different depths complicates the analysis of the spectra.

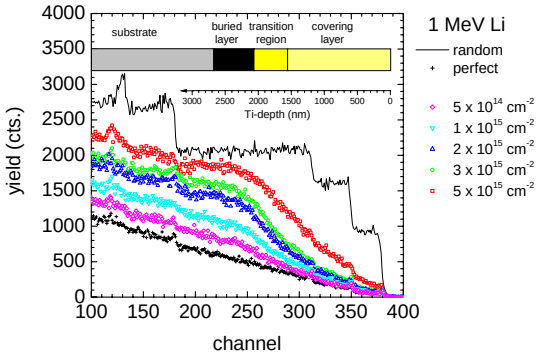

Fig. 1: RBS-spectra measured with 4 MeV He-ions of KTP irradiated with 1 MeV Li-ions at different ion fluences.

However, it is well known, that 1 MeV Li-irradiation into KTP results in a complex damage structure [1], which is schematically included in the figure. It consists of a covering layer containing point defects and point defect complexes, a transition region and a buried layer. For the irradiation with Li-ions at an ion fluence of 3×10^{15} cm^{-2} the transition region contains amorphous clusters and the buried layer is completely amorphized. The amorphization fluence for He-irradiation amounts to 1×10^{16} cm^{-2}.

The effective refractive indices of the TM-modes propagating in the planar waveguides were determined by means of m-line spectroscopy using prism-coupling at five wavelengths between 476.5 and 632.8 nm. The number of the guided modes increases with increasing ion fluence indicating an enhanced difference of the refractive index between the waveguide and the barrier. From the dependence of the effective refractive index on the mode number the distribution of the refractive index as a function of depth was calculated by means of the inverse Wentzel-Kramer-Brillouin (i-WKB) method as well as the transfer-matrix calculation method. Thereby a fermi-like distribution of the refractive index according to

$$n(z) = n_B + \Delta n(z) = n_B + \Delta n_B \frac{e^{-s} + 1}{e^{\frac{sz}{d} - s} + 1}$$

was assumed, with n_B the refractive index of the barrier, $\Delta n(z)$ the refractive index referring to the barrier index as a function of depth, Δn_B the difference of the refractive index between waveguide and barrier, d the FWHM-width of the waveguide and s the slope of the distribution. This kind of distribution was previously verified using the stepwise linear approximation [2]. The results are shown in Fig. 2.

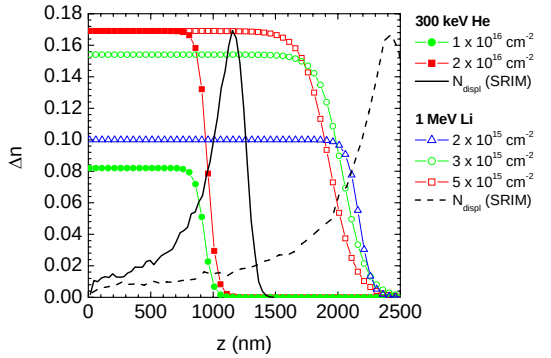

Fig. 2: Refractive index change Δn versus depth for KTP irradiated with He- and Li-ions, respectively.

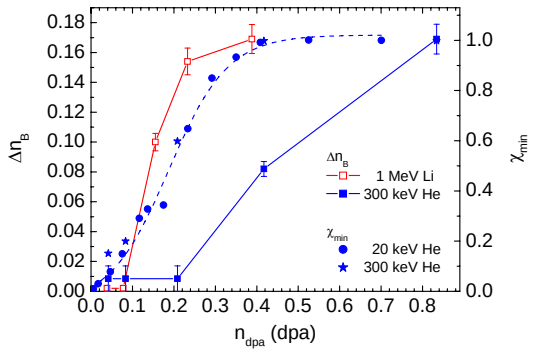

Fig. 3: Refractive index difference between waveguide and barrier Δn_B as a function of the normalized ion fluence n_{dpa} for KTP irradiated with He- and Li-ions, respectively. Additionally, the minimum yield χ_{min} taken from the RBS-spectra of He-irradiated KTP in the maximum of the damage distribution is given.

For both, the irradiation with He-ions and with Li-ions, the depth distributions of the primary displacements calculated by SRIM included in the figure in arbitrary units agree with the depths of the waveguide barriers as well as with the depths of the maximum of the defect concentration measured by RBS. In contrast to the He-irradiation, where the width of the waveguide increases with increasing ion fluence, Li-irradiation yields a decrease of the width of the guiding layer. This is explained by the fact that the transition region and the buried layer collectively act as barrier for light guiding. Compared to the He-irradiation, the transition region of the Li-irradiated KTP is much broader. Consequently, the refractive index profile is steeper for the He-irradiation. Anymore, if the barrier is already amorphous further irradiation causes broadening of the amorphous layer towards the surface of the crystal. This is observed for the irradiation with Li-ions at an ion fluence of 5 x 10^{15} cm^{-2}.

The difference of the refractive index between the waveguide and the barrier Δn_B is shown in Fig. 3 versus the normalized ion fluence n_{dpa}. = N_I x N_{displ}/N_0 with N_I the ion fluence, N_{displ} the number of primary displacements per ion and N_0 the atomic density of KTP. Additionally, the figure shows the minimum yield ($\chi_{min}(z) = Y_{al}(z)/Y_{ra}(z)$ with Y_{al} and Y_{ra} being the RBS yield of the aligned and random spectra, respectively) taken in the maximum of the damage distribution of KTP irradiated with He-ions.

According to the increase of the defect concentration Δn_B is increased with increasing ion fluence and saturates at $\Delta n_B = 0.17$. The amorphization fluence ($\chi_{min;He} = 1$ at 0.4 dpa) is less than that necessary to reach the saturation value of the refractive index difference ($\Delta n_{B;He} = 0.17$ at 0.8 dpa). Simplistic, amorphization measured with RBS stands for complete deterioration of the long-range order of single crystal atoms. The further increase of Δn_B for fluences above 0.4 dpa is probably a consequence of changes in the short-range order. Anymore, compared to the He-irradiation, for the irradiation with Li-ions the same value of Δn_B appears at much lower normalized ion fluences. This fact can be explained by the dilution of the collision cascades with decreasing ion mass and with an in-situ annealing process during the collisions due to increasing influence of the electronic energy loss, respectively.

In conclusion, the refractive index can be purposefully adjusted by varying the ion mass and the ion fluence.

The authors wish to thank G. Hagner and L. Leine for providing the computer codes, which have enabled the calculation of the refractive index profiles.

[1] F. Schrempel, Th. Höche, J.-P. Ruske, U. Gruesemann, W. Wesch, Nucl. Instr. and Meth. B 191 (2002) 202.
[2] F. Schrempel, Ch. Beeker, J. Fick, W. Wesch, Nucl. Instr. and Meth. B (2007) accepted.

Experimental Assessment of Structural Differences between Amorphous and Amorphized Matter

Th. Höche [1], F. Schrempel, M. Grodzicki [2], P. A. van Aken [3], F. Heyroth [4]

[1] Leibniz-Institut für Oberflächenmodifizierung e.V., Leipzig, Germany
[2] Institut für Mineralogie, Universität Salzburg, Salzburg, Austria
[3] Max-Planck-Institut für Metallforschung, Stuttgart, Germany
[4] Interdisziplinäres Zentrum für Materialwissenschaften, Martin-Luther-Universität Halle-Wittenberg, Germany

In-depth understanding of the structure-properties relationship of amorphous thin films (e.g., ultrathin gate oxides, ion-beam amorphized superficial layers, or nanometer-sized wetting layers at grain boundaries) becomes increasingly important for controlling device functions. Transition-metal $L_{2,3}$ electron energy-loss near-edge structures (ELNES) measured by high-resolution electron energy-loss spectroscopy (EELS) in the transmission electron microscope (TEM) is shown to be capable of distinguishing different cation coordination at nanometer spatial resolution. It is demonstrated on the basis of a barium titanium silicate (BTS) glass and its amorphized counterpart, prepared by ion irradiation of a single crystal of identical composition, that the coordination state of titanium not only can be clearly discerned but also differences between a glass and an amorphized single crystal of identical composition can be identified.

While a $2BaO\text{-}TiO_2\text{-}2SiO_2$ glass was obtained by splat cooling a melt obtained from $BaCO_3$, TiO_2 (rutile), and SiO_2, a $Ba_2(TiO)(Si_2O_7)$ single crystal was grown by the Czochralski pulling technique. The crystal was irradiated with 200 keV Ar-ions at ion fluences between 1×10^{12} and 1×10^{14} cm^{-2}. The damage formation was investigated by means of Rutherford backscattering spectrometry (RBS) in channeling configuration. A detailed description of the results, of the preparation of cross-sectional TEM samples and of measurement, extraction and correction of the EEL spectra is given in [1].

Concerning the RBS-results, after Ar-irradiation of the BTS-crystal at an ion fluence of 1×10^{14} cm^{-2}, a superficial amorphous layer of approximately 100 nm thickness is formed. Below this layer and down to a depth of 250 nm, the initially single-crystalline BTS is strongly modified but not entirely amorphous. These results, however, only reflect the degree of damage as related to the dechanneling of the analyzing ions and does not allow direct conclusions with respect to the type of structural modification, which can also not become resolved by transmission electron microscopy.

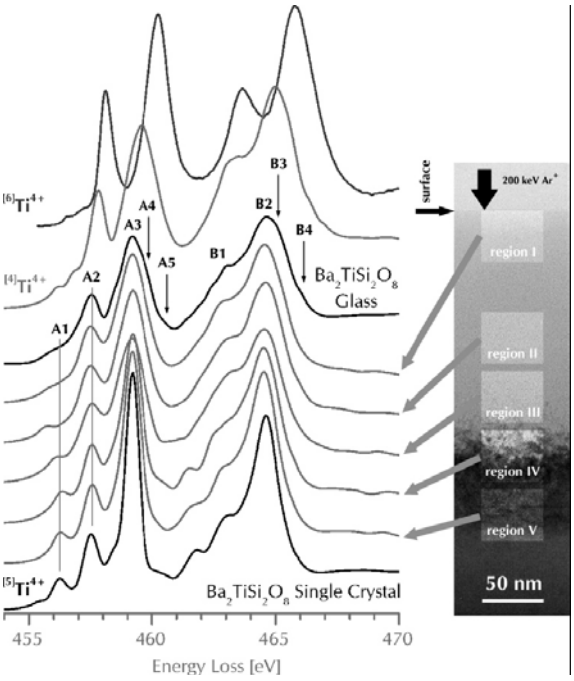

Fig. 1: Ti-$L_{2,3}$ ELNES spectra acquired at different depths of the BTS single crystal amorphized by Ar-irradiation in comparison to spectral reference data: tetrahedral coordination in β-Ba_2TiO_4 ($^{[4]}Ti^{4+}$), 5-fold (square-pyramidal) coordination found in fresnoite ($^{[5]}Ti^{4+}$), and octahedral coordination in $BaTiO_3$ ($^{[6]}Ti^{4+}$). For comparison, the Ti-$L_{2,3}$ ELNES of single-crystalline BTS and BTS-glass are also given. The integral intensity of all spectra was normalized between 455 and 467 eV, and the curves are plotted vertically staggered to facilitate their comparison.

However, in the cross-sectional TEM micrograph (see Fig. 1), a modified superficial layer totally extending to 260 nm depth into the crystal is found. At the lower end of the modified layer, a ~55 nm thick region V can be discerned that is not amorphized but contains most likely point defects. This region is covered by the ~55 nm thick region IV, in which crystalline fragments are embedded into an amorphous matrix. Between the surface and the top of region IV (depth ~150 nm), the BTS single crystal appears to be completely amorphized. Since minor fractions of crystalline clusters in an amorphous ambient cannot be resolved by high-resolution TEM, it is not astonishing that the RBS measurement did indicate incomplete amorphization in the depth range between 100 and 150 nm.

ELNES spectroscopy was hence applied at different depths to resolve this apparent discrepancy. As shown in Fig. 1, ELNES spectra acquired from a scanning area of 40 x 50 nm^2 in depths of 0-40 nm (region I), 80-120 nm (region II), and 130-170 nm (region III), respectively, in fact possess very significant differences. From the comparison of the Ti-$L_{2,3}$ ELNES spectrum of the amorphized BTS-crystal taken from region I and the BTS-glass, it becomes apparent that the amorphized layer can - due to the characteristic shape of the corresponding Ti-$L_{2,3}$ ELNES - unambiguously be assigned to the presence of $^{[5]}Ti^{4+}$. Detailed inspection, however, reveals that minima and maxima of the amorphized BTS-crystal Ti-$L_{2,3}$ ELNES are even more pronounced than the corresponding features in the BTS-glass Ti-$L_{2,3}$ ELNES, and the width of the peaks is smaller than in the glass. Moreover, maxima in the Ti-L_3 ELNES of the amorphized BTS-crystal in region I (especially peak A3 at 459.1 eV, assigned to the Ti-$3d_z^2$ orbital) possess a much higher peak-shape symmetry than the corresponding spectral features in the glass Ti-L_3 ELNES. This observation is strongly indicative of primarily pentahedrally coordinated Ti^{4+} at this depth. Tetrahedrally coordinated Ti^{4+} is giving rise to peaks A4 and B3 indicated in Fig. 1, while octahedrally coordinated Ti^{4+} causes the occurrence of peaks A5 and B4. Such peaks cannot be discerned in the amorphized single crystal, the contribution of non-pentahedrally coordinated Ti^{4+} (20% $^{[4]}Ti^{4+}$ plus 20% $^{[6]}Ti^{4+}$ in BTS-glass of identical composition) must therefore be significantly smaller if ever present in the amorphized single crystal. A different picture arises in regions II and III of the irradiated BTS single crystal. Besides a pronounced peak broadening in comparison to the spectra from regions IV and V being related to the absence of crystalline fragments, the major deviation is found for peak A1. This peak is related to the Ti($3d_{xy}$) orbital and significantly shifted toward lower energy losses in regions II and III. Recent theoretical studies have shown that the position of this peak is closely related to the bond length between the titanium ion inside the square pyramid and the apical oxygen ion (O4) such that a lowering of the bond length causes a shift of the peak toward lower energy losses. Hence, the Ti-$L_{2,3}$ ELNES spectra acquired at regions II and III are consistent with a nanoscopic picture comprising large argon atoms squeezed into the amorphous network at depths where they become deposited. The latter atoms provoke locally enhanced compressive stresses leading to very significant distortions of the lattice and - on the average - shorter bond length. The bond lengths distribution is thus found to be much wider than both in the single crystal and at depths within the amorphized crystal where no argon is deposited.

Growth of the BTS single crystal by R. Uecker (Institut für Kristallzüchtung Berlin), preparation of the BTS-glass by R. Keding (Institut für Glaschemie, Friedrich-Schiller-Universität Jena), computing time provided by RIST (Universität Salzburg), and granted access to the high-resolution TEM facilities at the MPI for Microstructure Physics Halle by U. M. Gösele are gratefully acknowledged.

[1] Th. Höche, F. Schrempel, M. Grodzicki, P. A. van Aken, F. Heyroth, Chem. Mater. 18 (22) (2006) 5351.

Influence of ion implantation on titanium surfaces for medical applications

S. Krischok [1], C. Blank [2], M. Engel [1], R. Gutt [1], G. Ecke [1], J. Schawohl [1], L. Spieß [1], F. Schrempel, G. Hildebrand [2], K. Liefeith [2]

[1] Zentrum für Mikro- und Nanotechnologien, TU Ilmenau P.O. Box 100565, 98684 Ilmenau
[2] Institut für Bioprozess- und Analysenmesstechnik e.V., 37308 Heiligenstadt

Meanwhile it is well known that surface topography and surface physico-chemistry as well as visco-elastic properties influence the cell response after implantation of implants into the human body. The implantation of ions, such as Ca and P, both elements present in the inorganic bone phase, is a new approach to improve the osseointegration of metallic biomaterials like titanium [1-3]. Pure commercial titanium grade 2 (ISO 5238-2) has been implanted with 30 keV Ca- and P-ions at fluences of 2×10^{17} and 1.5×10^{17} cm^{-2}, respectively. Concentration profiles of the observed elements as well as their chemical state and the crystallographic structure have been analyzed using X-ray photoelectron spectroscopy (XPS), X-ray diffraction (XRD) and Auger electron spectroscopy (AES) depth profiling. A detailed description of sample preparation and measurement techniques is given in [4].

The XPS-spectra in Fig. 1 show, that the surface of the pure titanium is oxidized and consists mainly of TiO_2. Besides the titanium related peak I, the O(1s) peak shows some additional features at higher binding energies, which gives evidence for the presence of additional oxygen. The calculated chemical composition is given in Table 1.
After implantation of P-ions the near surface region shows rather small changes in the chemical surface composition. As proven by AES depth profiling, P was successfully implanted, but into deeper regions of about 25 - 350 nm. Obviously, only 7 at.% of P is present in the near surface region and the oxygen/titanium ratio is rather similar to TiO_2. A closer analysis of the P(2p) peak reveals two different environments for the incorporated P. From the observed binding energies we assign peak I to P^{3+} and therefore intuitively to phosphate like species, which is supported by the presence of an additional O-component at about 531.6 eV in the O(1s) signal. The additional P(2p) peak around 129 eV (III) points to negatively charged P and is eventually related to phases such as Ti_xP_y.

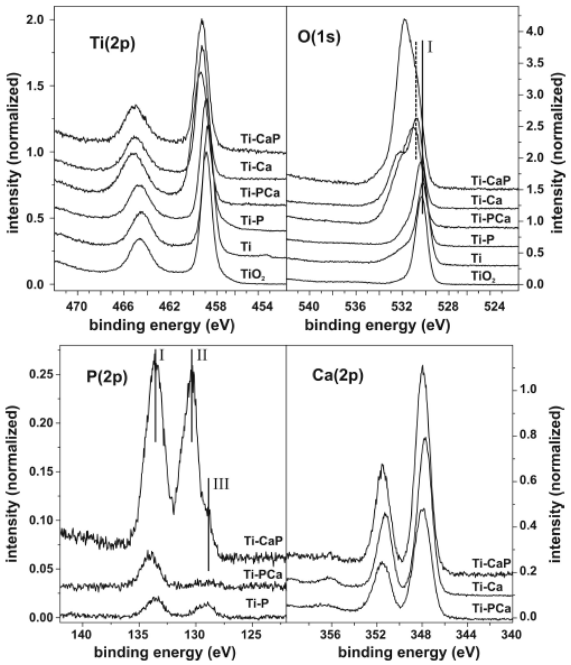

Fig. 1. XPS(AlKα) spectra of the Ti(2p), O(1s), P(2p) and Ca(2p) core levels, for different titanium surfaces. Spectra of a single crystalline rutile TiO_2(100) sample are included as a reference. The intensities are normalized to the Ti(2p) peak height. The vertical O(1s)-line I indicates the TiO_2 phase. Inserted vertical (P2p)-lines I, II, and III indicate the different P-components.

Table 1: Calculated chemical composition (at.%) as calculated from the XPS data shown in Fig. 1.

	Ti	**Ca**	**P(I/II/III)**	**O(I/other)**
TiO2	25	0	0	60(55/5)
Ti-P	22	0	7(4/0/3)	60(46/14)
Ti-CaP	6	11	21(11/9/1)	48(5/43)
Ti-PCa	15	13	5(4/0/1)	58(38/20)
Ti-Ca	13	18	0	55(31/24)

In contrast to P, the implantation of Ca leads to the appearance of the implanted element in the surface region. A strong Ca

signal is observed together with an additional component in the O(1s) peak. This is a strong evidence that Ca and O containing species (e.g. CaO, $Ca(OH)_2$ and $CaCO_3$) are formed in the near surface region. In the valence band region (not shown), the XPS spectra show three additional well pronounced features which correspond well with spectra obtained for $CaCO_3$. Thus we conclude, that at least part of the implanted Ca ions forms $CaCO_3$. In agreement to our XPS data, AES depth profiling detects a high amount of Ca at the surface, whereas the Ca concentration drops with depth.

AES depth profiling of titanium successively implanted with Ca and P ions (see Fig. 2), reveals that the implantation sequence is very important.

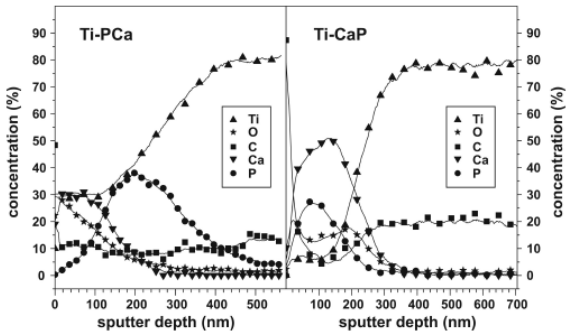

Fig. 2. Elemental concentration profiles as measured by AES depth profiling for titanium samples after P implantation followed by Ca implantation (left) and Ca implantation followed by P implantation (right).

Just like for pure P implantation, for the P implantation followed by the Ca implantation (Ti-PCa), a low amount of P at the outermost surface is detected. The obtained XPS data are rather similar to Ca implantation. AES depth profiling reveals that Ca is found near the surface, whereas P is implanted into deeper regions. The corresponding XPS data show, that only small amounts (about 5 at.%) of P are detected. In contrast to the data for pure P implantation the $P^{-\delta}$-peak (III) is not present anymore. The observed Ca(2p) signal and the valence band structure is very similar to that obtained for pure Ca implantation. The O(1s) signal shows a broad peak. However, in contrast to pure Ca implantation, we do not observe two well separated components. Taking into account the data for the P implanted surface, obviously the O(1s) signal now consists of at least three different components related to TiO_2 (530.5 eV), phosphates (531.5 eV) and a Ca induced oxygen species (532.2 eV), most likely including $CaCO_3$. Summarizing, the P implantation followed by Ca implantation leads to a chemical composition which is similar to pure Ca implantation in the near surface region and very similar to pure P implantation in deeper layers.

If the implantation is performed in the opposite order (Ca followed by P implantation: Ti-CaP) the chemical surface composition changes drastically. Ca and P are now located near the surface and in similar depths. These changes have strong impact on the XPS spectra; now an increased P(2p) intensity (about 20 at.% P) is detected. Moreover, besides the already discussed P(2p) spectral features I and III, an additional P peak II is present. Since this structure is only present if P is implanted into the Ca pre-implanted titanium we assume that both elements are involved in the formed compound responsible for this peak. Therefore it is very likely that the additional structure can be assigned to phases such as for instance $Ca_3(PO_4)_2$, $CaHPO_4$, $Ca_{10}(PO_4)_6(OH)_2$. Grazing X-Ray diffraction (not shown) reveals a rather complicated crystallographic structure consisting of various phases. The measured diffraction pattern is in agreement with the formation of $CaCO_3$ and various compounds consisting of Ca, P and O.

This project is supported by the ”Thüringer Kultusministerium” (TKM) under grant no.: B478-04003.

[1] E. Wieser, I. Tsyganov, W. Matz, H. Reuther, S. Oswald, T. Pham and E. Richter, Surf. Coat. Technol. 111 (1999) 103.

[2] M.T. Pham, M.F. Maitz, W. Matz, H. Reuther, E. Richter and G. Steiner, Thin Solid Films 379, (2000) 50.

[3] F. Schrempel, G. Hildebrand, M. Frant, W. Wesch, K. Liefeith, Mater. Res. Soc. Symp. Proc. 0908-OO14-22.1.

[4] S. Krischok, C. Blank, M. Engel, R. Gutt, G. Ecke, J. Schawohl, L. Spieß, F. Schrempel, G. Hildebrand, K. Liefeith, Surf. Sci. (2007) accepted.

Ion-beam induced effects at 15 K in MgO

E. Wendler, K. Gärtner and W. Wesch

Radiation effects in MgO have been studied for many years (see [1, 2] and references therein). However, in most of these papers rather high ion fluences (10^{15} ... 10^{17} cm^{-2}) were applied. Less data can be found regarding the damage formation at very low ion fluences, for which the collision cascades of individual ions do almost not overlap. In this work the damage formation in MgO during ion implantation at 15 K is studied with special emphasis placed on the region of very low ion fluences [3].

(100) oriented MgO samples purchased from CRYSTEC were implanted with 150 keV Ar or 450 keV Xe ions. Defect analysis was performed by Rutherford backscattering spectrometry (RBS) in channelling configuration using 1.4 MeV He ions and a backscattering angle of 170°. Both ion implantation and RBS analysis were done with the samples cooled to 15 K without changing their environment.

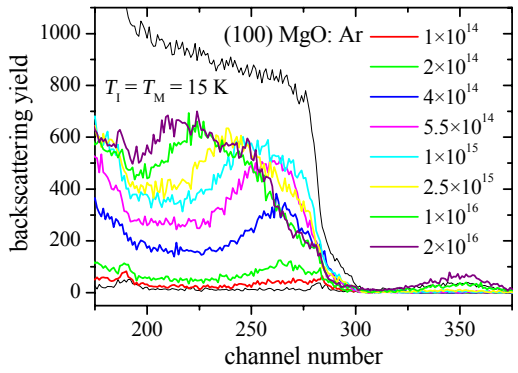

Fig. 1: RBS spectra of 1.4 MeV He ions backscattered on 400 keV Au implanted $In_{0.1}Ga_{0.9}N$ (a) and 380 keV Au implanted GaN (b) at $T_I = T_M = 15$ K (no temperature change between implantation and measurement). The ion fluences are given in 10^{14} cm^{-2}.

Figure 1 shows the energy spectra of He ions backscattered on 150 keV Ar implanted MgO for various ion fluences N_I. Up to the maximum ion fluence applied ($N_I^{max} = 2\times10^{16}$ cm^{-2}) the yield of the aligned spectra does not reach the random level, i.e. no amorphisation is found even if implantation and analysis were done at 15 K.

Assuming the displaced magnesium and oxygen atoms to be randomly distributed within a lattice cell, the evaluation of the measured backscattering data provide the defect profiles given in Fig. 2 for Ar ion implantation. For low ion fluences ($N_I \leq 5.5\times10^{14}$ Ar cm^{-2}) a reasonable agreement between the measured defect profiles and those calculated using SRIM2003 is observed except of the more pronounced tails of the measured profiles. The

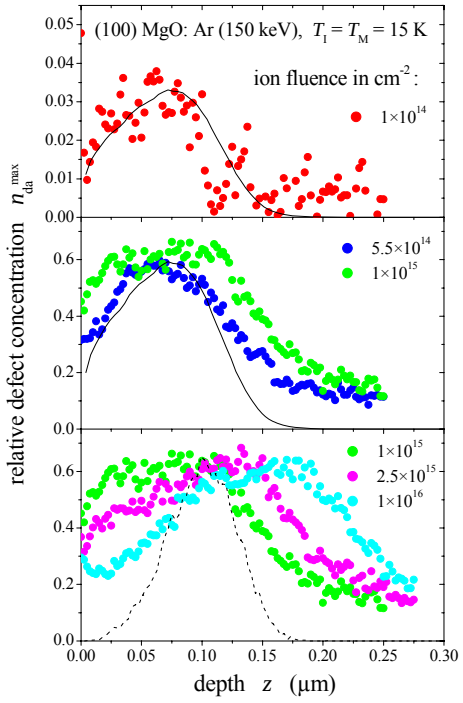

Fig. 2: Relative defect concentration n_{dpa} versus depth z in (100) MgO implanted with 150 keV Ar ions and various ion fluences. The thin solid line in the upper and middle part is the distribution of primary displacements calculated with SRIM2003 given in arbitrary units. The thin dashed line in the lower part is the distribution of Ar ions calculated with SRIM2003 given in arbitrary units.

maximum defect concentration remains almost constant for fluences $N_I > 5.5\times10^{14}$ cm^{-2}. For larger fluences the damaged layers extend into depths far behind the projected range of the implanted ions (see lower part of Fig. 2). A strong annealing of the defects in the near-surface region of about 0.12 μm is visible in the figure. Most probably it occurs due to the electronic energy loss of the implanted ions, which is highest near the surface. Such annealing effects are well known from

insulating materials (see [2] and references therein).

For the analysis of the fluence dependence of defect production the defect concentration in the maximum of the distribution was taken. The resulting values n_{da}^{max} versus the ion fluence N_I are given in Fig. 3. For $n_{da}^{max} < 0.05$ the defect concentration n_{da}^{max} increases linearly with rising N_I (region I) whereas for larger defect concentrations a steeper increase of n_{da}^{max} with N_I occurs followed by a saturation (region II). This change of the slope indicates a change in the mechanism of damage production. For Ar implantation a third region is found for $N_I > 1\times10^{15}$ cm^{-2}, in which part of the defects, which have already formed in the maximum of the distribution, disappear during proceeding implantation (region III in Fig. 3).

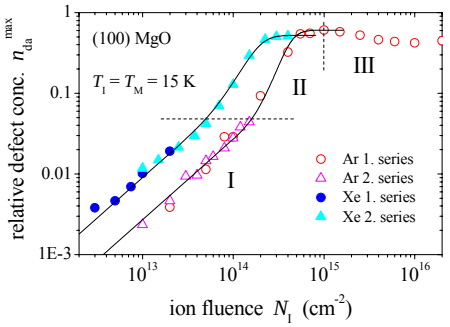

Fig. 3: Relative defect concentration in the maximum of the distribution n_{da}^{max} versus the ion fluence N_I for 150 keV Ar and 450 keV Xe ion implantation in (100) MgO. Series 1 and 2 represent two different samples. Each of them was stepwise implanted followed by the RBS measurement after each implantation step.

Within region I each ion hits regions of undamaged MgO and no remarkable overlap of the damage cascades of the individual ions occurs. Therefore, the damage efficiency per ion can be estimated from these data. This is done in Fig. 4 which plots n_{da}^{max} versus the number of primary displacements per lattice atom n_{dpa} . The latter is given by $n_{dpa} = N_{displ}^{*} N_I/N_0$ with $N_{displ}^{*} = 0.30\times10^{8}$ cm^{-1} and 0.95×10^{8} cm^{-1} for Ar and Xe implantation, respectively, being the number of Mg displacements per ion and unit depth and $N_0 = 4.25\times10^{22}$ cm^{-2} being the Mg atomic density of MgO. Figure 4 clearly shows that the data $n_{da}(n_{dpa})$ fall on one line for both ion species. This indicates that within the corresponding range of ion fluences the defect formation is determined by the nuclear energy deposition. The slope of the line amounts to 0.5.

Taking into account that RBS measures and SRIM calculates the number of displaced lattice atoms, this means that only 50% of the primarily displaced lattice atoms survive the relaxation of the collision cascades. This is true provided the displacement energies used in the SRIM calculations (55 eV) are correct. To obtain a slope of unity the displacement energies have to be increased to 105 eV which is much higher than the results of the other measurements [1]. Therefore our results are in agreement with earlier results summarised in Ref. [1], which yield a surviving defect fraction between 0.15 and 0.4. The higher value obtained here may be caused by the lower temperature of the samples realised in the present experiments or may be connected to the fact that different techniques were applied (data summarised in Ref. [1] are from density or optical absorption measurements).

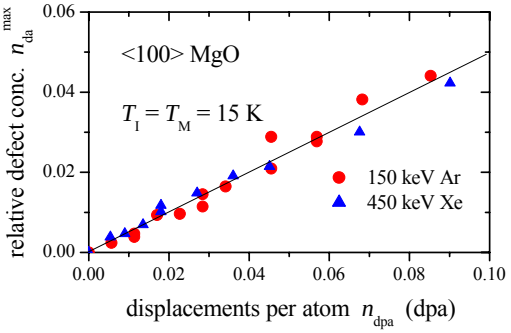

Fig. 4: Relative defect concentration in the maximum of the distribution n_{da}^{max} versus the number of displacements per lattice atom n_{dpa} for 150 keV Ar and 450 keV Xe ion implantation in (100) MgO. The line is the linear fit to all data.

There is also another possibility for the interpretation of the RBS data for region II. Assuming that the maximum number of displaced Mg atoms is unity, the RBS data provide a spread of the magnesium atoms of $\sigma_{Mg} \approx 0.6$ Å which is not unrealistic and points to a heavily distorted crystal. In this case the saturation of the backscattering spectra in Fig. 1 could be explained by a limitation of the displacement distance of the magnesium atoms without a limitation of their relative number (for detail see [3]).

[1] S.J. Zinkle, C. Kinoshita, J. of Nucl. Mater. 251 (1997) 200.

[2] S.J. Zinkle, V.A. Skuratov, D.T. Hoelzer, Nucl. Instr. and Meth. B 191 (2002) 758.

[3] E. Wendler, K. Gärtner, W. Wesch, Nucl. Instr. and Meth. B (in press).

Silicon nanowire synthesis by chemical vapour deposition on metal implanted silicon substrates

Th. Stelzner, G. Andrä[1], F. Falk[1], E. Wendler, W. Wesch, R. Scholz[2], S. Christiansen[2,3]

[1] *Institute for Physical High Technology, Albert-Einstein-Str. 9, 07745 Jena, Germany*
[2] *Max-Planck-Institute of Microstructure Physics, Weinberg 2, 06120 Halle, Germany*
[3] *Physics Department, Martin-Luther-University Halle-Wittenberg, Hoher Weg 8, 06120 Halle, Germany*

One-dimensional semiconductor nano-structures have gained much attention due to possible applications, for example, in electronic, photonic, and sensing devices. Here we studied the potential of various metals (Au, Ga, In, Al) to be used as a template in the catalysis of SiNW growth by chemical vapour deposition [1]. We used ion implantation for the deposition of the metals and studied their behaviour in the silicon substrates upon annealing. Moreover, silicon nanowires (SiNWs) were grown by the vapour-liquid-solid (VLS) growth mechanism using gold implanted silicon substrates [2,3].

Si(111) substrates were implanted at room temperature with Au^+, Ga^+, In^+, or Al^+ ions to an ion fluence of 1 x 10^{16} cm^{-2} and with energies of 10 - 30 keV. The implanted substrates were annealed in air at temperatures between 350 and 700°C in order to study the agglomeration of the implanted metal in silicon. In order to grow SiNWs the Au implanted wafers were etched with 5 % HF to remove the oxide layer immediately before trans-ferring them into the CVD chamber. After annealing the substrates in vacuum at ~580°C for 10 min the temperature was reduced to ~500°C and a mixture of 5 sccm Ar and 4 sccm SiH_4 was introduced for the nanowire growth for 20 min at a pressure of 0.5 mbar.

Implantation with the high ion fluence at room temperature leads to an amorphized silicon (a-Si) layer at the substrate surface with a thickness of 30 - 40 nm.

Upon annealing of the Au implanted substrates the gold agglomerates and forms nanoparticles. The gold agglomeration is aided by the amorphized silicon layer in which the Au has a diffusion coefficient that is about 4 orders of magnitute higher compared to the one in crystalline silicon. After annealing at 350°C statistically distributed gold nanoparticles of a few nanometers in diameter form within the amorphous silicon matrix. At higher annealing temperatures even larger gold particles form that tend to reside closer to the wafer surface. Moreover, the initially amorphous silicon matrix starts to epitaxially crystallize. For sufficiently long enough anneals (> 30 min) the Au crystallites are confined to the wafer surface and have diameters in the range of 50-200 nm. Figure 1 shows TEM cross-sections of Au implanted Si(111) annealed at 350°C and 600°C both for 1 hour.

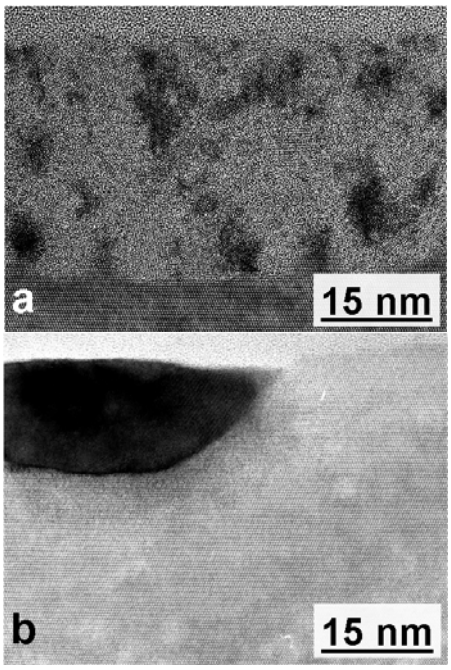

Fig. 1. HRTEM micrographs of the surface region of Au implanted Si(111): a) annealed at 350°C, gold nanoparticles (dark patches) are distributed within the a-Si layer, and b) annealed at 600°C, after recrystallisation of the amorphous layer the Au crystals are confined to the wafer surface.

Annealing of the wafers implanted with Ga, In, or Al does not lead to the epitaxial recrystallisation of the a-Si. Figure 2 shows cross-sectional TEM micrographs of the implanted a-Si regions after annealing at 700°C for 1 hour in air. Nanoparticles with a diameter of only a few nanometers are distributed within the a-Si and only occasionally reach the wafer surface (for the Ga-case) if at all. The a-Si stays amorphous or recrystallizes partly to a nano-crystalline state. Probably the high metal content (more than 10 %) in the surface layer and a relatively low diffusion coefficient of the metals prevent recrystallization.

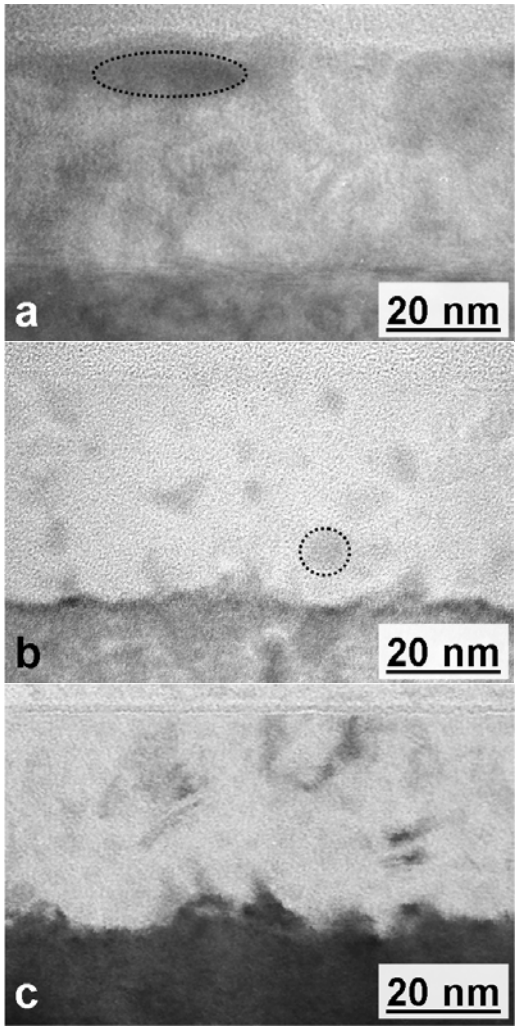

Fig. 2. Cross-sectional TEM micrographs of the annealed wafers implanted at an energy of 30 keV with a) gallium , b) indium, and c) aluminum prior to annealing. Agglomerates of the metals (dashed line as a guide to the eye) are visible within the amorphous or already partly recrystallized silicon matrix.

The use of the Au implanted wafers in the CVD process leads to SiNWs which under the applied conditions (low supersaturation level of SiH_4) mainly grow perpendicular to the surface and thus epitaxial to the Si(111) substrate. However, some of the wires are oriented along the three other equivalent (111) directions (Figure 3a). At a higher supersaturation level of silane (20 sccm Ar, 4 sccm SiH_4, 5 mbar) the CVD process leads to dense SiNW arrays, where the SiNWs show different growth directions, such as (110), (111), and (100) (Figure 3b).

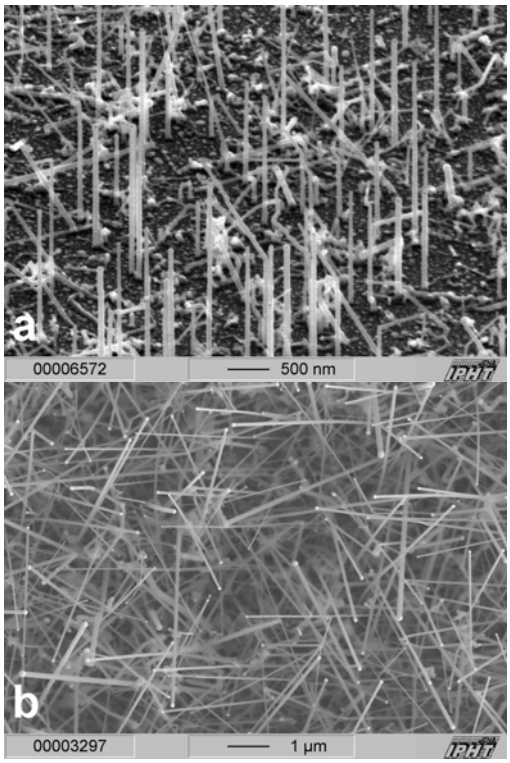

Fig. 3. SEM images of SiNWs obtained on Au implanted and annealed Si(111) after CVD growth. a) At lower partial pressure of silane most of the wires grow in the (111) direction which is perpendicular to the substrate surface (tilt angle of the image 60°). b) Dense SiNW arrays with different growth directions of the wires are obtained at a higher supersaturation level of silane.

[1] Th. Stelzner, G. Andrä, F. Falk, E. Wendler, W. Wesch, R. Scholz, S. Christiansen, Nucl. Instr. and Meth. B (in press).
[2] Th. Stelzner, G. Andrä, E. Wendler, W. Wesch, R. Scholz, U. Gösele, S. Christiansen, Nanotechnol. 17 (2006) 2895.
[3] S. Christiansen, R. Schneider, R. Scholz, U. Gösele, Th. Stelzner, G. Andrä, E. Wendler, W. Wesch, J. Appl. Phys. 100 (2006) 084323.

Room temperature annealing of low-temperature ion implanted sapphire

E. Wendler, C.S. Schnohr, W. Wesch

High-quality sapphire single crystals (α-Al_2O_3) of c-, a- and r-orientation obtained from CRYSTEC were implanted at 15 K (LT) with 80 keV Na, 150 keV Ar or 150 keV K ions. After the measurement at LT the analysis of the annealing behaviour was done at room temperature (RT) with RBS in channelling configuration using 1.4 MeV He ions and a backscattering angle of 170°.

The minimum yield $\chi_{min} = Y_{al}/Y_{ra}$ was calculated from the yields of the aligned spectra Y_{al} of the perfect (un-implanted) or damaged crystal and the yield measured in random direction, Y_{ra}. For the study of defect accumulation at LT the difference in minimum yield $\Delta\chi_{min} = \chi_{min}^{dam} - \chi_{min}^{perf}$ was taken as a measure for the amount of damage produced.

The RT measurements were done repeatedly over the course of more than one year in order to study the long-term RT annealing behaviour. Using the computer code DICADA [1] the depth profiles of the relative defect concentration, $n_{def}(z)$ were calculated from the measured RBS spectra.

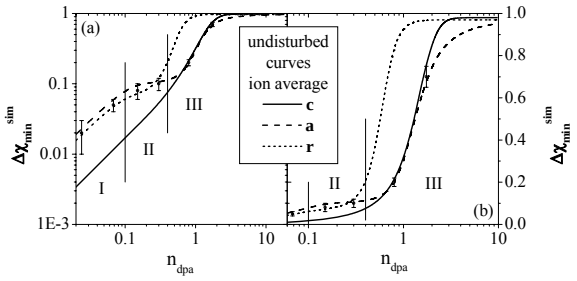

Fig. 1: $\Delta\chi_{min}^{sim}$, representing the defect concentration corrected to remove the influence of the He measurement, as a function of ion fluence, recalculated into the number of displacements per lattice atom n_{dpa}, for c-, a- and r-oriented samples. For better visibility the graphs are given in (a) double- and (b) half-logarithmic scale. The experimental error is indicated by arbitrary data points.

Figure 1 shows the difference in minimum yield $\Delta\chi_{min}^{sim}$ in the maximum of the distribution for implantation and measurement at LT versus the ion fluence recalculated into the relative number of displaced lattice atoms n_{dpa}. The plotted data $\Delta\chi_{min}^{sim}$ are ion-averaged values which have been corrected to remove the influence of the He induced annealing (undisturbed fluence dependence; for details of the procedure see [2-4]). For implantation up to about $n_{dpa} \approx 0.1$ (region I, see Fig. 1) only isolated point defects are produced. At larger ion fluences (region II) the collision cascades of individual ions start to overlap and the recombination of point defects causes a plateau in the undisturbed fluence dependence for a- and r-oriented samples. Within region I and II the defect concentration measured in samples of c-orientation is lower than that measured in samples of a- und r-orientation. This can be explained by the fact that in this direction the vacant octahedral sites of the Al sub lattice are hidden (for details see [2-4]). A further increase of the ion fluence to $n_{dpa} > 0.4$ (region III; see Fig. 1) results in the formation and stimulated growth of clusters, the structure of which is not yet clear. The samples considered here all fall into this region of cluster defects after implantation and measurement at LT.

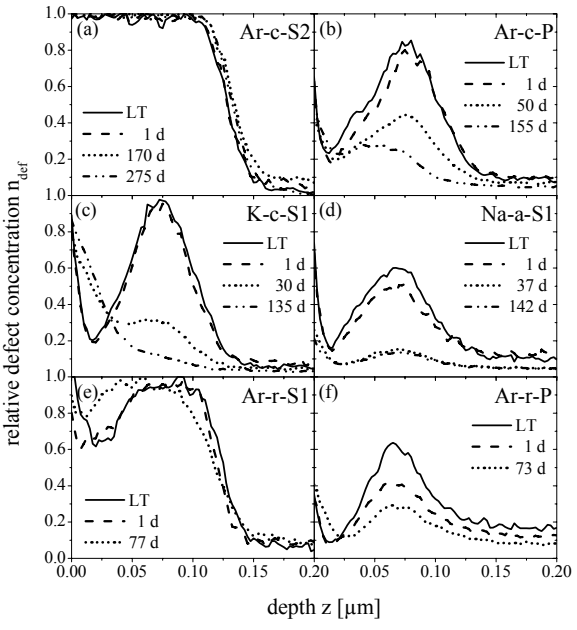

Fig. 2: Relative defect concentration, n_{def}, versus depth z calculated from the Al part of the RBS spectra for the LT measurement at 15 K and the RT measurements done at various times after implantation for the samples investigated.

The relative damage concentration n_{def} versus depth z is plotted in Fig. 2 for the measurement at 15 K and the analysis done at RT as a function of time t. For samples where a relative defect concentration of unity is reached up to the surface, no change of the defect concentration is observed (see Fig. 2 (a)). However, this layer is not assumed to be amorphous because for the corresponding value of number of displace-ments per lattice atom $n_{dpa} = 7.1$ different damage concentrations still occur for the various crystal orientations (see Fig. 1 and [2]). The latter should not be the case for an amorphous layer. Probably a stable and dense structure of clusters has formed with no defect-free areas in between, which does not allow for annealing at RT. For buried damaged layers with a maximum n_{def} in the range of 0.5...0.9 after implantation at LT, the defect concentration is reduced when measured at RT after one day and this continues when storing the samples at RT for some weeks.

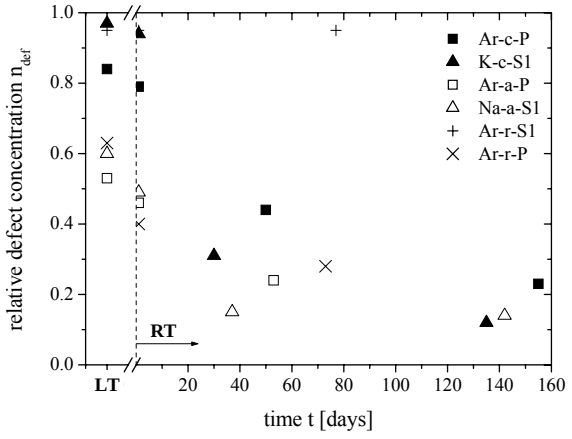

Fig. 3: Relative defect concentration, n_{def}, taken at the depths of the maximum defect concentration, as a function of time t for the samples investigated.

A summary of the results of the RT annealing is given in Fig. 3 which plots the relative defect concentration at the depth of the maximum of the LT damage profiles versus time t. Usually the time dependence of phase transformations is fitted using the Johnson-Mehl-Avrami (JMA) model [5], which yields the volume fraction f of transformed material to be $f = 1 - \exp[-(Kt)^n]$. K is a factor depending on the nucleation and growth velocity of the new phase and n is the Avrami exponent which has a value between one and four depending on the nucleation mechanism and the morphology of the growth. If we assume the starting phase to be the clusters mentioned above and the end phase to be crystalline material, the volume fraction of non-transformed material is given by $n_{def} = \exp[-(Kt)^n]$. Unfortunately, the number of data points is too low to do proper fits. However, our simulations with varying K and n clearly show that the general tendency (steep decrease of n_{def} at low t) can only be reproduced with $n \approx 1$. This means that precipitates grow from nuclei which are already present, whereas nucleation is of minor importance. The precipitates we can see with RBS are crystalline areas being aligned to the substrate. Therefore, the corresponding nuclei are crystalline areas which were not damaged during ion implantation but remained from the former undamaged crystal. In the case of completely damaged layers such nuclei do not exist and consequently, no annealing is seen (see Fig. 2 (a)). For a more comprehensive understanding of the RT annealing behaviour of sapphire implanted at very low temperatures further studies are necessary.

[1] K. Gärtner, Nucl. Instrum and Meth. B 227 (2005) 522.

[2] C.S. Schnohr, E. Wendler, K. Gärtner, W. Wesch, K. Ellmer, J. Appl. Phys. 99 (2006) 123511

[3] C.S. Schnohr, E. Wendler, K. Gärtner, K. Ellmer, W. Wesch, Nucl. Instrum. and Meth. B 250 (2006) 85

[4] C.S. Schnohr, Diploma thesis (English), Friedrich-Schiller-Universität Jena 2005.

[5] see e.g. K.L. Sahoo, M. Wollgarten, K.B. Kim, J. Banhart, J. Mater. Res. 20 (2005) 2927.

MD simulation of ion implantation damage in AlGaAs : I. Displacement energies

K. Gärtner

The ion irradiation causes a collision cascade consisting of energetic recoils where the low energy recoils of the final part of the collision cascade are approximately isotropically distributed. The generation of point defects in crystalline $Al_xGa_{1-x}As$ caused by such recoils with low energies up to 50 eV is investigated using classical molecular dynamics computer simulations and a modified Tersoff potential. The crystals are kept at room temperature and the composition x is varied between zero and one. The MD cell of the $Al_xGa_{1-x}As$ lattice consists of 10×10×10 unit lattice cells and contains in total 8000 atoms.

The displacement energy is the threshold energy of a low energy recoil for generating one stable Frenkel pair. It is not a fixed value but it depends on the direction of the motion of the recoil. Therefore, usually an average displacement energy E_d is used corresponding to the isotropical distribution of the recoil velocities. The isotropically distributed recoils are simulated by a series of atoms starting with a given kinetic energy E_r (up to 50 eV) in a direction chosen by random numbers according to the isotropic distribution. The quantity of interest is the average number of stable vacancies which is obtained after short time recovery of about 2.5 ps (remark: number of Frenkel pairs = number of vacancies in this energy region). For the example of x = 0.5 and Ga recoils the result for the average number of stable vacancies $n_{av}(V,E_r)$ as a function of the recoil energy E_r is given in Fig.1. As can be seen, there are three characteristic regions of the recoil energy E_r. In the first region up to 8 eV, no vacancy is generated at all. The second region ranging from 8 eV to about 30 eV is characterized by a considerable increase of $n_{av}(V,E_r)$ with increasing E_r up to $n_{av}(V,E_r) = 1$. In this region $n_{av}(V,E_r)$ varies between zero and one and it can be understood as the probability to generate one vacancy. In the third region given by $E_r >$ 30 eV, one recoil generates in average more than one vacancy and $n_{av}(V,E_r)$ increases approximately with a constant rate. This dependence of $n_{av}(V,E_r)$ on the recoil energy shows that there is no sharp threshold energy for the generation of one stable vacancy but its generation occurs within an energy region (region 2) with a probability ranging from zero to one. Therefore, an (average) displacement energy E_d is introduced by replacing $n_{av}(V,E_r)$ in region 2 by a step function with the same area which means that the two hatched areas in Fig.1 must be equal. Consequently, E_d is given by the position of the step.

Fig.1. The average number of stable vacancies $n_{av}(V)$ (averaged over time interval

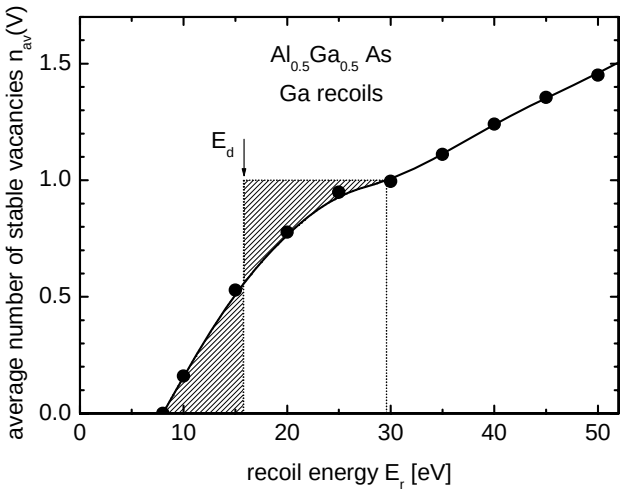

from 2.5 ps to 3.0 ps) generated by Ga recoils in $Al_{0.5}Ga_{0.5}As$ at room temperature, as a function of the recoil energy E_r. The results of the simulation are given by the filled circles and the full line represents the corresponding spline. The procedure of the determination of the displacement energy E_d is explained in the text

Using this procedure, the displacement energies are determined for the Al, Ga and As atoms in the $Al_xGa_{1-x}As$ crystal for different compositions x. The results are given in Fig.2. As can be seen, the dis-

placement energy for Al is considerably larger than that of Ga and As. Furthermore, the displacement energies of Al and Ga increase slightly with increasing Al content x, while the displacement energy of As show a stronger dependence on the value of x. It is interesting to note that the average of the three displacement energies follows Vegard's law within the statistical errors while this is not true for the single displacement energies.

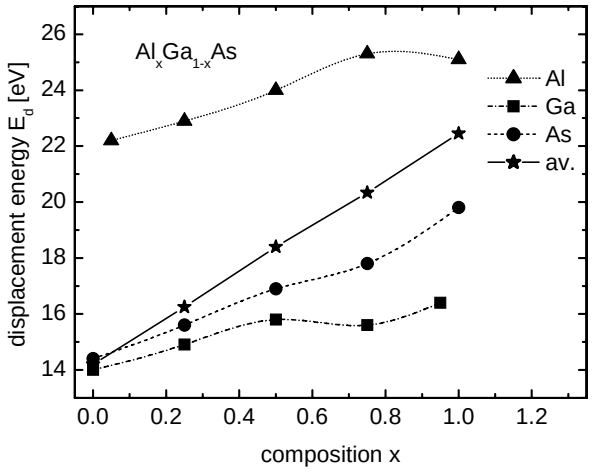

Fig.2. The displacement energy E_d for the Al, Ga and As atoms in $Al_xGa_{1-x}As$ at room temperature as a function of the composition x. The filled symbols give the results of the simulation (the statistical error is within the size of the symbols) and the lines represent the corresponding spines. The average displacement energy is added by the stars.

In order to understand these results and get information about the main processes contributing to the total average number of vacancies, all the different kinds of point defects generated by the low energy recoils have been studied and partially the trajectories of the recoils have been statistically analyzed and also visualized. Summarizing, it was found that recoils which overcome the first neighbor distance provide the main contribution to stable vacancies (therefore in the following called 'efficient' recoils). There are mainly two effects. First, the number of the 'efficient' Al recoils is smaller than the number of the 'efficient' Ga and As recoils. Second, the average total path length of the 'efficient' Al recoils is considerably larger than that of the 'efficient' Ga and As recoils, while the maximum distances of these Al recoils (from their starting points) is even a bit less than that of the corresponding Ga and As recoils. This indicates the 'efficient' Al recoils to move like 'random walk', where only a small part of them succeed in occupying interstitial sites and most of them return to their lattice site which has been confirmed by the visualization of a series of recoil trajectories. This means that the lower number of Al recoils which overcome the first neighbor distance and their lower probability for occupying an interstitial site (compared with that of Ga and As recoils) are mainly responsible for the displacement energy of Al being considerably larger than those of Ga and As.

The fact that the displacement energies of Al and Ga increase only slightly with increasing Al content x, while the displacement energy of As show a stronger dependence on the value of x can be understood as follows. For all the main processes mainly the first neighbor of the starting recoil is involved. In $Al_xGa_{1-x}As$, the Al atoms as well as the Ga atoms have four As atoms as next neighbors independent of the composition x. Therefore the corresponding processes and consequently also the displacement energy E_d depend only weakly on the composition x. The situation is different for As recoils where the next neighbors are Al atoms and Ga atoms with an average composition given by x. Because the influence of the next neighbored Al atom and the next neighbored Ga atom on the generation of vacancies is different, the resulting average number of vacancies and the displacement energy E_d show a remarkable dependence on the composition x. Finally, it can be stated that the dependence of the displacement energy of an atom in $Al_xGa_{1-x}As$ on the composition x is considerably determined by the composition of its first neighbors.

Quenching of photoluminescence of Si nanocrystals in SiO_2 matrices by foreign ions

O. Debieu, F. Huisken, W. Wesch, and W. Witthuhn

Silicon nanocrystals are discussed as possible carriers of the Extended Red Emission (ERE), an astrophysical phenomenon observed in many stellar objects and clouds [1,2]. In order to prove whether Si nanocrystals embedded in silica and silicate grains give rise to similar emission features as observed for free oxygen-passivated Si nanocrystals, we have carried out photoluminescence (PL) studies of Si nanocrystals (nc-Si) in solid state matrices (mainly SiO_2) and investigated the effect of foreign ions on the PL of the nanocrystals.

Silicon nanocrystals were produced in SiO_2 windows by Si ion implantation and subsequent annealing at temperatures above 1000 °C. For the present studies, we have used as substrates 0.2-mm-thick quartz plates into which the Si ions were implanted with energies of 100 keV. The typical ion fluence was 1×10^{17} Si ions per cm^2. The annealing was performed in a high-temperature oven at 1100 °C for 1 h under the exclusion of oxygen.

The PL studies were carried out at room temperature by irradiating the samples with the fourth harmonic of a ns-pulsed Nd:YAG laser (λ = 266 nm). In order to avoid bleaching effects, the laser energy was generally kept at rather low values around 200 $\mu J/cm^2$. The PL emission was recorded using a computer-controlled grating spectrometer equipped with VIS/IR photomultiplier (Hamamatsu R5509-72, 300 – 1700 nm). All spectra were corrected for the spectral response of the optical setup.

When exposed to the light of a simple laboratory UV lamp, the annealed samples showed weak PL, but clearly visible to the naked eye. As reported earlier [3], the photoluminescence originating from the silicon nanocrystals after annealing at 1100 °C gives rise to a broad (150-nm-wide) band peaking between 750 and 950 nm. The exact position depends on the ion fluence and the annealing temperature as these parameters have strong influence on the size of the nanocrystals. The variation with the size can be understood in view of the quantum confinement effect according to which a PL maximum at larger (shorter) wavelength correlates with a larger (smaller) average size of the Si nanocrystals.

For the present studies, we have prepared Si nanocrystals in quartz windows as described before. After annealing and verifying the proper PL of the Si nanocrystals, the samples were doped with various ions at various fluences. To recover the PL of the Si nanocrystals, it was necessary to apply a second annealing which was performed at 900 °C.

Figure 1 shows the effect of calcium ion incorporation on the intensity of the PL originating from nc-Si as a function of the Ca ion fluence applied. The black curve has been measured for the reference sample which was not irradiated with Ca ions but which was subjected to the second annealing. At low Ca ion fluence (*e.g.* 1×10^{12} cm^{-2}) the effect is rather small. But when the Ca ion fluence is further increased, the PL of the Si nanocrystals is progressively quenched. At a Ca ion fluence of 1×10^{14} cm^{-2} the integrated PL intensity is reduced by a factor of 10. The dependence of the PL quenching on the Ca ion fluence is plotted in Fig. 1b.

Together with the quenching, we observe a progressive red shift of the PL curve. This is clearly demonstrated in Fig. 2 where we show in panel (a) the normalized PL curves and in panel (b) the red shift of the PL with respect to the undoped sample.

The progressive quenching of the nc-Si PL with increasing Ca doping is attributed to the formation of defects which also remain after the second annealing. Keeping in mind, that the PL at short wavelengths is associated with small nanocrystals while the PL at longer wavelengths is attributed to the larger nanocrystals, the observation of a pronounced red shift indicates that the PL of the smaller nanoparticles is more efficiently quenched, meaning that the small nanoparticles are more susceptible to quenching. This observation gives us some insight into the mechanism responsible for the quenching. If the Ca ions produced defects in the interior of the nanocrystals we would expect that the quenching scales with the volume of the nanocrystals, *i.e.* the PL of larger nc-Si par-

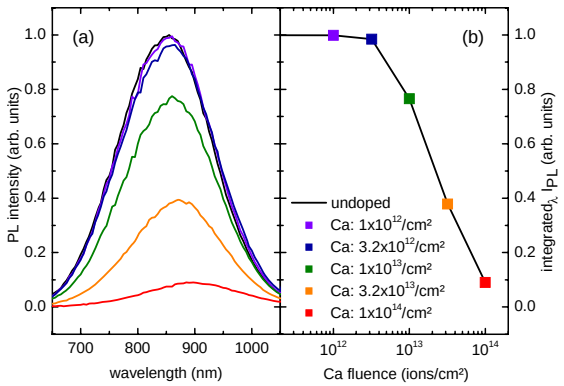

Fig. 1: PL spectra of Si nanocrystals embedded in a quartz window (black curve) showing the effect of subsequent Ca ion incorporation (colored curves). In panel (b), the PL quenching as a result of foreign ion implantation is quantified.

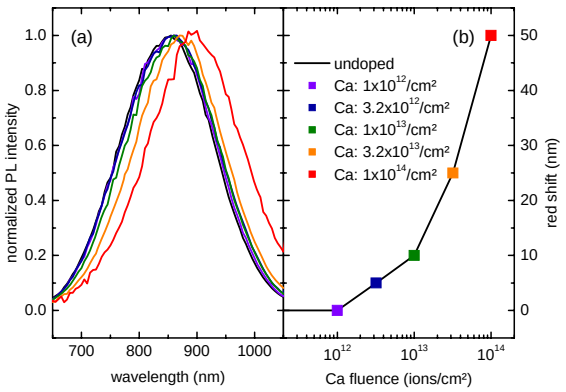

Fig. 2: Normalized PL spectra of nc-Si samples as a function Ca concentration (same measurements as in Fig. 1) demonstrating the progressive red shift. Panel (b) shows the red shift as a function of the Ca ion fluence.

ticles would be more effectively quenched and we should observe a blue shift. Since we observe the opposite trend, we conclude that, with the second annealing, the Ca ions (if present) are expelled from the Si nanocrystals so that they reside either at the interface between the nc-Si's and the SiO_2 matrix or deeper in the matrix.

This picture would also explain the observed red shift. The electrons of the excitons produced upon UV photon absorption can be trapped by the positive Ca ions at the interface. The hole remaining in the core of the Si nanocrystal acts as a defect inhibiting radiative recombination of newly created excitons. Since in small nanocrystals, the electron can more readily interact with a Ca^{2+} ion at the interface, this effect is more pronounced for smaller nc-Si's explaining the observed red shift.

We have also studied the effect of Ca doping on the nc-Si PL in the time domain by measuring the decay of the PL after excitation. It was found that, with increased Ca concentration, the decay rates increased as well. This is in agreement with the PL quenching observed in the frequency domain.

Similar quenching effects have been observed when the luminescent nc-Si samples were doped with other ions, such as Mg^{2+}, Na^{+}, Ge^{+}, and Er^{3+}, but only for Er^{3+}, we could demonstrate a transfer of the excitation energy giving rise to a new emission at 1536 nm originating from the Er^{3+} ion.

The systems studied during the course of the present project can be considered as analog materials for astrophysical dust grains (SiO_2 grains containing Si nanocrystals). Comparing the results with those obtained earlier on free nanocrystals, which led to the proposal that Si nanocrystals could be the carriers of the ERE, it is found that the PL of a Si nanocrystal of a specific size is shifted to lower energy when it is surrounded by the matrix. As a result, if the ERE observations are to be explained by Si nanocrystals in SiO_2 grains, the size distribution must be shifted by 1 nm to smaller values. Finally, our doping experiments have shown that silicate grains with silicon-rich cores cannot be efficient light emitters. Therefore, silicates containing nc-Si can be discarded as candidates for ERE carriers.

Acknowledgments

This work was supported by a cooperation between the Max-Planck-Institut für Astronomie and the FSU Jena as well as by the Deutsche Forschungsgemeinschaft.

References

[1] A. N. Witt, K. D. Gordon, and D. G. Furton, Astrophys. J. **501**, L111 (1998).

[2] G. Ledoux *et al.*, Astronomy and Astrophysics **377**, 707 (2001).

[3] O. Debieu *et al.*, Annual Report of the Institute of Solid State Physics of the University of Jena (2004) p. 66 and (2005) p. 64.

Electronic spectroscopy of PAHs under astrophysical conditions: Benzo[ghi]perylene

G. Rouillé, M. Arold, A. Staicu, Th. Henning, and F. Huisken

Polycyclic aromatic hydrocarbons (PAHs) have been postulated to constitute an important component of the interstellar medium [1] and to account for some of the so-called diffuse interstellar bands (DIBs) [2], a still unresolved mystery in astronomy which was first discovered in the twenties of the last century.

Despite the importance of this class of molecules not only for astrophysics but also for nanophysics – PAHs can be regarded as nanoscale fragments of a sheet of graphite – the spectroscopic characterization of PAHs in the gas phase has remained a challenge, and therefore, systematic investigations are rather scarce. To improve this situation and to provide more laboratory data that can be compared with astrophysical observations, we have initiated a research program to study the electronic spectroscopy of PAH molecules under astrophysically relevant conditions, *i.e.* at low temperature and at low density so that the molecules do not interact. For this purpose, the molecules are studied in the expansion of a supersonic jet using a highly sensitive photoabsorption technique as provided by cavity ring-down spectroscopy (CRDS). In this technique, the decay of the radiation from a pulsed tunable laser at the exit of a high-quality resonator is measured. The decay time can be directly converted to an absorption cross section.

Using this technique, we have already investigated several PAHs, both in their neutral and cationic states [3,4]. Here we report on our latest study devoted to the electronic $S_1 \leftarrow S_0$ transition of benzo[ghi]perylene (BghiP, $C_{22}H_{12}$) whose molecular structure is depicted as inset in Fig. 1. It can be considered as a precursor of the prominent PAH molecule, coronene, which is formally obtained from BghiP by closing the open ring with C_2H_2.

While the second electronically excited state (S_2) of BghiP at 369 nm has been studied just recently [5], the information on the significantly weaker transition to the first electronically excited state (S_1) was very scarce. We only had some matrix data (in Ne and Ar) that was obtained by our own team and by our cooperation partners at NASA Ames [6]. Even though it appeared that we had to work at the sensitivity limit of our CRDS setup, it was our goal to determine the origin band position of the $S_1 \leftarrow S_0$ system at low temperature in the gas phase and to obtain information on some fundamental vibrations in the S_1 state.

The main results of our study are presented in Fig. 1. According to high pressure liquid chromatography (HPLC) measurements carried out in our group, it was found that the BghiP samples that we had purchased contained traces of perylene (on the order of 1%). Since perylene has absorption bands in the same spectral region, it was not possible to measure a clean absorption spectrum of BghiP alone. As a result, our experimental spectrum presented as upper trace in Fig. 1 shows bands of the $S_1 \leftarrow S_0$ transition of BghiP and perylene as well. The center trace shows a control spectrum of pure perylene, and the lower trace represents the difference between the two spectra, emphasizing the bands related to BghiP by marking them with circles. Peaks labelled with a star denote residuals of the perylene bands.

The analysis of these spectra regarding band positions and rotational contours has yielded the position of the origin band of the $S_1 \leftarrow S_0$ transition of BghiP at 399.567 nm (25 027.1 ± 0.2 cm^{-1} in vacuum). In addition, the fundamental frequencies of a dozen vibrational modes for the S_1 states of BghiP could be specified. It was important to determine the position of the origin band, in order to test the accuracy of theoretical predictions established by the means of TD-DFT-based calculations [5]. Our conclusion is that such calculations do not perform well, especially when compared to calculations based on semi-empirical models.

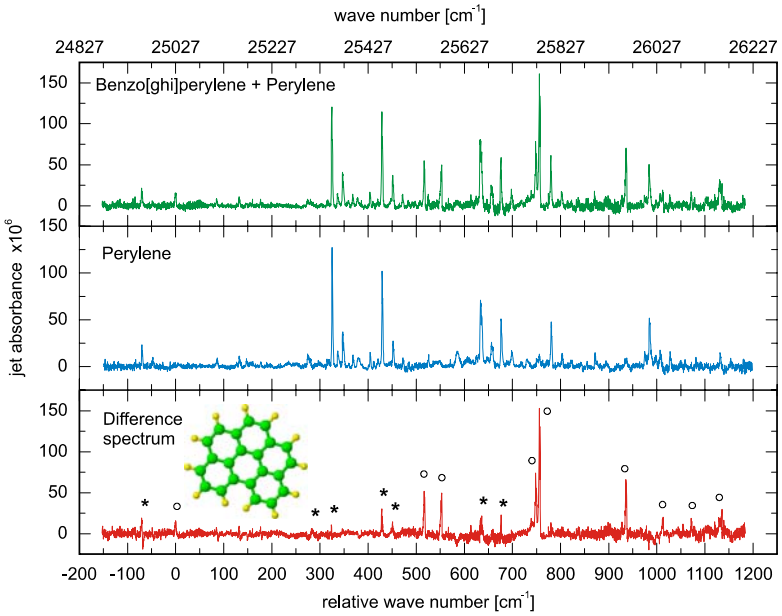

Fig. 1: CRDS spectra of benzo[ghi]perylene containing 1% of perylene (top) and pure perylene (middle), as well as the difference spectrum (bottom). The peaks designated with circles are assigned to benzo[ghi]perylene while those labelled with an asterix are reminiscent of perylene.

Incidentally, the analysis of the spectra has also yielded the position and assignment of about twenty new bands in the $S_1 \leftarrow S_0$ transition of perylene and of a dozen bands associated with complexes of perylene with argon.

Evaluating the upper trace of Fig. 1 and comparing two bands of BghiP and perylene exhibiting the same absorbance, we obtained the result that the absorption cross section related to the perylene band is about hundred times larger than the one corresponding to the BghiP band. This ratio is indicative of the very weak oscillator strength of the $S_1 \leftarrow S_0$ transition in benzo[ghi]perylene.

As far as the problem of diffuse interstellar bands is concerned, the comparison of the BghiP spectrum with astronomical data bases does not lead to any identification. This can be due to the fact that the $S_1 \leftarrow S_0$ transition is too weak and the first strong transition (to the S_2 state) near 369 nm is out of the ranges covered by current DIB surveys. Yet, an interesting point is that the band contour analysis has yielded a band width of 2.7 cm^{-1} associated with a rotational temperature close to 40 K. This supports the assumption that neutral PAHs are better candidates for DIB carriers than their positively charged counterparts which exhibit band widths on the order of 20 – 30 cm^{-1}. But in order to present electronic transitions at wavelengths longer than 400 nm, neutral PAHs have to be heavier than the molecules studied here.

Acknowledgments

This work was supported by a cooperation between the Max-Planck-Institut für Astronomie and the FSU Jena as well as by the Deutsche Forschungsgemeinschaft.

References

[1] F. Salama *et al.*, Astrophys. J. **526**, 265 (1999).

[2] P. Jenniskens and F.-X. Désert, Astron. Astrophys. Suppl. Ser. **106**, 39 (1994).

[3] S. Krasnokutski *et al.*, Annual Report of the Institute of Solid State Physics of the University of Jena (2004) p. 64.

[4] A. Staicu *et al.*, Annual Report of the Institute of Solid State Physics of the University of Jena (2005) p. 62.

[5] X. Tan and F. Salama, J. Chem. Phys. **123**, 014312 (2005).

[6] X. Tan and F. Salama, unpublished results.

Optical Spatial Solitons in Semiconductor Optical Amplifiers

Mathias Weiß, Wolfgang Richter

1. Optical Spatial Solitons

Whereas the cross section of a common light beam increases with propagation, optical spatial solitons are beams that travel without changing their shape. They could play a decisive role in future all-optical applications such as optical routing, guiding, and beam steering.

Light intensities required for soliton excitation range from microwatts to hundreds of watts. This figure depends on the medium in which the soliton is propagating. With respect to applications in optical signal processing and communication, the aim is to have both fast and low power solitons. Therefore, semiconductor optical amplifiers (SOAs) are an appropriate medium. They support stable solitons with power levels in the range of milliwatts and response times in the range of picoseconds.

The formation of spatial solitons requires self-focusing of the light beam. In semiconductors, this process relies on the dependence of the material's refractive index on light intensity. Among other things, the refractive index n for light of frequency ν depends on the free carrier concentration N:

$$n = \sqrt{n_0^2 - \frac{Ne^2}{4\pi^2 m_e^* \varepsilon_0 \nu^2}}$$

Here, n_0 denotes the refractive index without free carriers, e the electron charge, ε_0 the permittivity of free space, and m_e^* the effective mass of conduction band electrons. Fig. 1 shows the refractive index in an SOA perpendicular to light propagation direction.

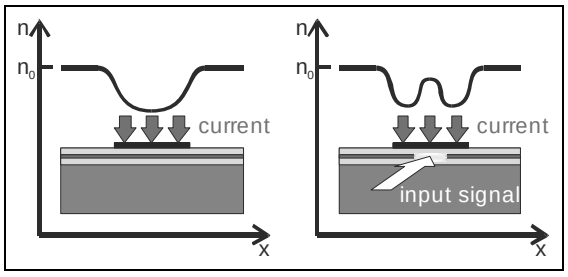

Figure 1. Lateral cross section of an SOA (lower part) and resulting refractive index distribution (upper part). The layers on top of the SOA form a planar waveguide with the amplifying active zone in its center.

The injection of electric current into a limited area of the planar waveguide raises N and causes the refractive index to drop in this region. Diffusion of electrons in x direction is responsible for the somewhat blurred index change (left part of Fig. 1). If a light beam of appropriate frequency is focused on the front facet of the electrically pumped SOA, this light becomes amplified in the active zone due to stimulated emission, thus decreasing the free carrier density N. In the beam's center the optical intensity I is larger than at its tails, therefore N is altered nonuniformly. Consequently the refractive index in the middle will be larger than at the margins because $n(x)$ resembles $I(x)$ (right part). One can say that the input signal creates its own strip waveguide.

2. Device Design

For examination of soliton formation, semiconductor optical amplifier chips have been manufactured from a GaAs wafer with a waveguiding GaAs/AlGaAs layer system on top which has been grown by Ferdinand-Braun-Institut Berlin. An InGaAs quantum well forms the active region in the center of this waveguide. The top electrode of the 10 mm long and 0.5 mm wide devices consists of 150 µm wide metalized contact stripes, separated by 50 µm wide insulating regions. Thus, electrically pumped gain regions (gain coefficient $g > 0$) and unpumped saturable absorption (SA) regions ($g < 0$) alter in light propagation direction (Fig. 2).

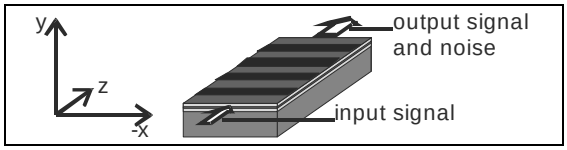

Figure 2. SOA chip with structured top electrode (dark grey – metalized, light grey – insulating).

In general, optical gain saturates with signal power P as [1]

$$g = \frac{g_0}{1 + P/P_{\text{sat}}},$$

where the small-signal gain g_0 and the saturation power P_{sat} are controlled by the pumping current density. In the absorption

regions less intense optical fields are attenuated to a larger extent than fields of higher intensity. By this means it is possible to stabilize the background in the SOA/SA system and to support self-focusing of Gaussian beams (Fig. 3).

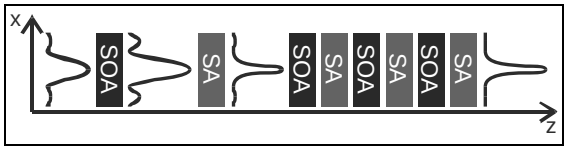

Figure 3. Propagation of optical signal through SOA, SA, and stacked device. Note that the SA regions both suppress noise and diminish the width of the Gaussian peak.

3. Measurements and Results

The optical experiments were performed at the Institute of Applied Physics in collaboration with the group of Prof. Thomas Pertsch. An elliptically shaped laser beam of 940 nm wavelength and 14.8 µm Gaussian radius in *x* direction was focused on the front facet of the SOA. The intensity profile at the chip's rear facet was recorded with a CCD camera, yielding curves such as the one in Fig. 4 for each measurement. The width of the transmitted signal was determined by fitting the data with a Gaussian function.

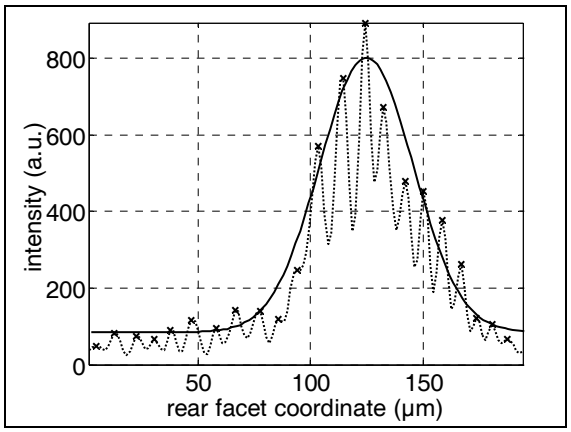

Figure 4. Exemplary graph for determination of the beam width at the rear facet. The dotted line represents experimental data. The regular pattern is traced back to a longitudinal Fabry-Perot interference inside the SOA chip. Its local maxima (crosses) represent the envelope of the measured signal and are fitted with a Gaussian function (solid line).

Patterned semiconductor optical amplifiers are dissipative systems, thus the solitons propagating in such devices are called dissipative spatial solitons [2]. Their characterizing feature is that both the beam width and the beam power do not change with propagation. Furthermore, these figures are entirely controlled by the material parameters and the amplifier current. As long as they lie within certain parameter windows, called "range of stable attraction", the input parameters do not affect the soliton properties.

In order to check for both of the above mentioned soliton features, two types of measurements were carried out: Firstly, the amplifier current was varied from 0 to 12 A at constant input power of 87 mW (Fig. 5).

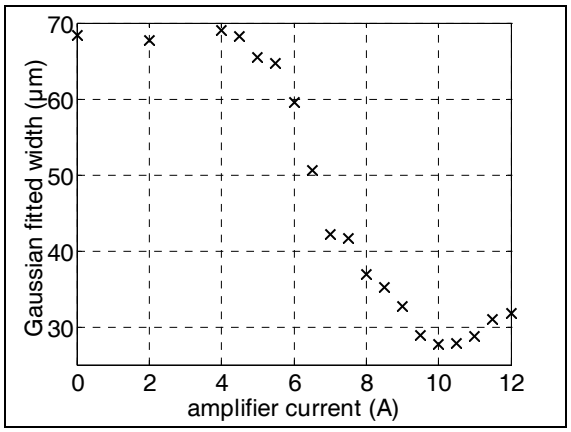

Figure 5. Gaussian fitted radius of lateral signal distribution at the rear facet at 87 mW input power.

Secondly, the input power was changed from 0 to 116 mW at 8 A amplifier current.

Whereas the first measurement clearly shows self-focusing at currents larger than 5 A, the second measurement does not show the expected constant output power for varying input power.

The results can be understood considering the numerical simulations of light propagation through an SOA which have been carried out by Oleg Egorov from the Institute of Condensed Matter Theory and Solid State Optics. These simulations suggest that 8 A amplifier current are not in the range of stable attraction, thus the observed self-focusing at this current is only a preliminary stage for soliton formation and the soliton as stable attractor forms only at currents larger than 10 A.

References

[1] M. J. Conelly. *Semiconductor Optical Amplifiers*. Kluwer Academic Publishers, 2002.

[2] E. A. Ultanir et. al. Stable Dissipative Solitons in Semiconductor Optical Amplifiers. *Physical Review Letters*, 90(25), 2003.

Preparation and characterization of pyrrole-functionalized carbon- and silicon-terminated silicon carbide surfaces

Bernd Schröter, Johanna Sochos, Wolfgang Richter, Martin Preuss[1], Friedhelm Bechstedt[1]

[1] *Institut für Festkörpertheorie und Optik, Friedrich-Schiller-Universität Jena, Max-Wien-Platz 1, 07743 Jena*

During the last years, the formation of organic thin films on crystal surfaces has attracted much attention in the surface science community, from both the fundamental and practical points of view. In particular, organic functionalization is becoming an indispensable tool for the development of semiconductor-based devices. This technique comprises, on the one hand, the possibility to overcome the size limitations inherent to current-day silicon-based transistors by contacting source and drain with a molecular gate. On the other hand, it may be used for imparting molecular functionality onto inorganic components by, e.g., covalent immobilization, thus obtaining sensitivity towards chemical stimuli. If such hybrid systems are to be used, however, as highly selective sensors in vivo, nontoxicity in the living organism must be assured, which leads to the minimal demand of biocompatibility.

Compared to silicon, both diamond and silicon carbide (SiC) have the same advantages like stability and biocompatibility [2], but SiC processing is easier. Therefore, silicon carbide could be the ideal candidate for the substrate material of a biocompatible biosensor. For the realization, a strategy for the covalent immobilization of the active molecules, e.g. enzymes, on SiC has to be developed.

The high breakdown field, high thermal conductivity, and strong bonding in SiC may turn out advantageously for high-power and high-frequency devices being operational up to 1000 K. The electronic properties of SiC can be tailored due to the large number of possible polytypes simply by variation of the SiC bilayer stacking along the (111) or (0001) direction. For example, the fundamental gap ranges from 2.4 eV in cubic 3C-SiC to 3.3 eV in hexagonal 2H-SiC. The difficulties in the preparation procedure of clean, high-quality SiC crystals and surfaces have prevented its widespread commercial use by now. However, in this respect substantial progress has been made recently.

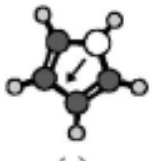

Fig. 1: Sketch of the pyrrole molecule: white (gray, small gray) disks correspond to N (C, H) atoms, respectively, and double bonds are indicated; the permanent dipole moment μ =1.93 D of the free molecule is represented by an arrow.

The pyrrole (C_4H_5N, Fig. 1) molecule has been chosen for organic functionalization of SiC surfaces for three reasons:
first, it is a small aromatic molecule, resulting in a relatively limited number of conceivable bonding possibilities on SiC. Second, it possesses as functional units a NH group and two carbon-carbon double bonds which may be used for further functionalization of the surface. Third, it is readily available in good quality, ensuring the reproducibility of the experimental results.

The adsorption of pyrrole on both polar faces of SiC{111} / {0001} is studied by means of x-ray photoelectron spectroscopy (XPS), low-energy electron diffraction (LEED) and, scanning tunneling microscopy (STM). Accompanying *first-principles* calculations of energies, geometries, and core-level shifts elucidate possible bonding geometries in dependence on the polarity and the reconstruction of the clean SiC surface [1].

The experiments were performed in an ultrahigh-vacuum multichamber piece of

equipment. The substrate preparation was similar as described in Refs. 2 and 3. The on-axis 6H-SiC(0001) polar surfaces (silicon or carbon face) were prepared *ex situ* by hydrogen etching at 1800 K. The nominally on-axis SiC surfaces show atomically flat terrraces up to several hundreds of nanometers wide. *In situ* substrate preparation was done by the common heating in Si flux to clean the surface and to obtain differently reconstructed substrate surfaces corresponding to different surface compositions. The stoichiometry and symmetry of the surfaces were controlled using low-energy electron diffraction (LEED), scanning tunneling microscopy (STM), and x-ray photoemission spectroscopy (XPS). Photoelectron spectra have been measured by Mg *Kα* excitation at electron emission angles of 0° and 70° to the surface normal. The measured binding energies have been referenced to the silicon carbide signals of Si 2*p* at 100.8 eV and C 1*s* at 283.0 eV.

Because there are some difficulties with the usual wet chemical processing of SiC, the alternative way has to be followed, which means that small organic molecules with functional groups are immobilised on the clean surface in a vacuum chamber at substrate temperatures between 300 K and 1000 K in ultrahigh vacuum.

Figure 3 presents Nitrogen 1s photoelectron spectra of pyrrole evaporated in vacuum at room temperature on 6H-SiC(0001) (√3x√3) R30° (a) before and (b) after heating in ultrahigh vacuum at 700 K exposition of a SiC sample.

The comparison with theoretical calculations [1] and other experimental data leads to the conclusion that the molecules adsorb on the surface via N-H-dissociation and the formation of covalent N-Si bonds. Additionally, it can be concluded that UV-radiation leads to a higher surface coverage and heating to 600°C leads to a decomposition of the adsorbed molecules and the formation of silicon nitride and silicon carbide species.

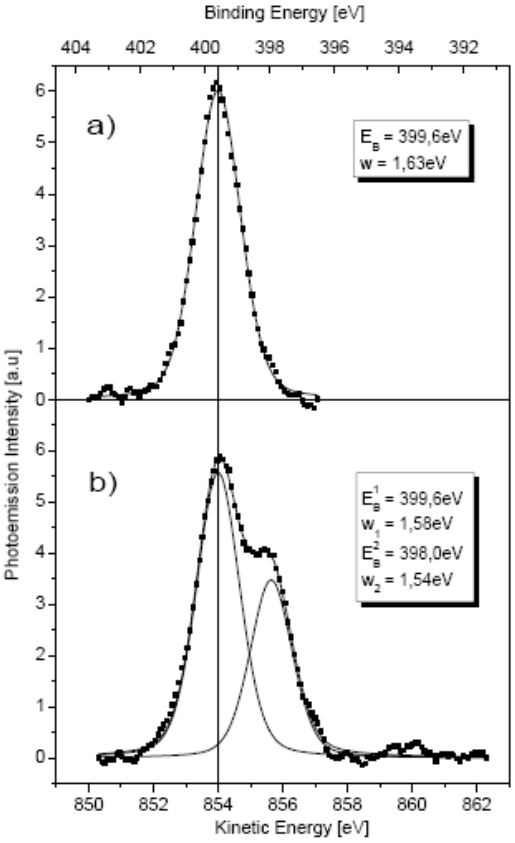

Fig. 2 Measured Nitrogen 1s photoemission signals of pyrrole evaporated in vacuum at room temperature on 6H SiC(0001) (√3 x √3) R30° (a) before and (b) after heating in ultrahigh vacuum at 700 K. The peak positions on the binding-energy scale and the peak widths are given in the insets.

While the geometries of the clean Si-face of SiC(0001) with (√3x√3) R30° or 3x3 translational symmetries are well established and agreed upon, no such models exist for the corresponding C faces. One partial aim of this study was to use pyrrole to probe the surface composition of the 3x3 phase of the C face: the x-ray photoemission spectra hinted at the formation of a covalent N-Si bond and, as such, to the presence of Si at the C face.

References:

[1] M. Preuss, F. Bechstedt, W.G. Schmidt, J. Sochos, B.Schröter, W. Richter, Phys. Rev. B 74 235406 (2006).

[2] B. Schröter, K. Komlev, W. Richter, Mater. Sci. Eng. B **88** (2002) 259 – 263.

[3] A. Winkelmann, B. Schröter, W. Richter, J. Phys: Condens. Matter 16 (2004) S1555-1578.

Growth and characterization of carbon nanotubes on silicon carbide

R. Volkmer, A. Hartung, B. Schröter

The defined growth of carbon nanotubes (CNTs) is an essential requirement for their utilization in nanoelectronics and nanooptics. Though CNTs with various parameters such as diameter, length, chirality or number of walls can already be produced in great quantities by standard processes like arc discharge, chemical vapor deposition (CVD) and laser ablation, the task of placing single tubes with the desired properties like chirality at defined positions is a problem not yet solved.

Besides using catalyst-assisted chemical vapor deposition (CCVD), we investigate an alternative fabrication technique of growing carbon nanotubes on SiC(0001) surfaces in ultra high vacuum (UHV).

Kusunoki et al. achieved films of aligned CNTs perpendicular to the surface on the carbon face of SiC$(000\bar{1})$ by heating the substrate at 1700°C in a low vacuum. On the other hand, they got several sheets of graphite parallel to the surface, when applying the same procedure to a Si-face SiC(0001) substrate [1].

However, single horizontal CNTs were grown on a 6H-SiC(0001) (Si face) substrate at temperatures above 1500°C in ultrahigh vacuum by Derycke et al. [2].

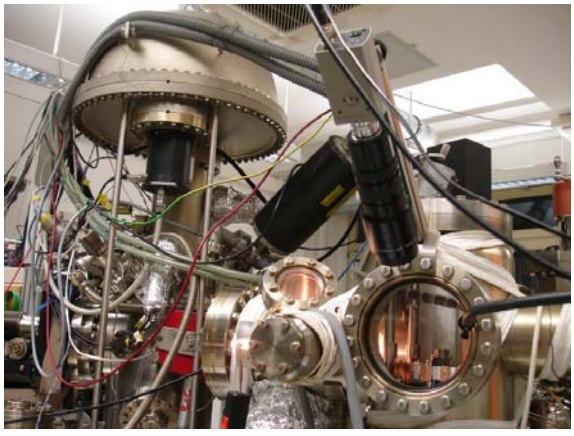

Figure 1: UHV multichamber equipment for surface preparation and characterization by STM, XPS and LEED

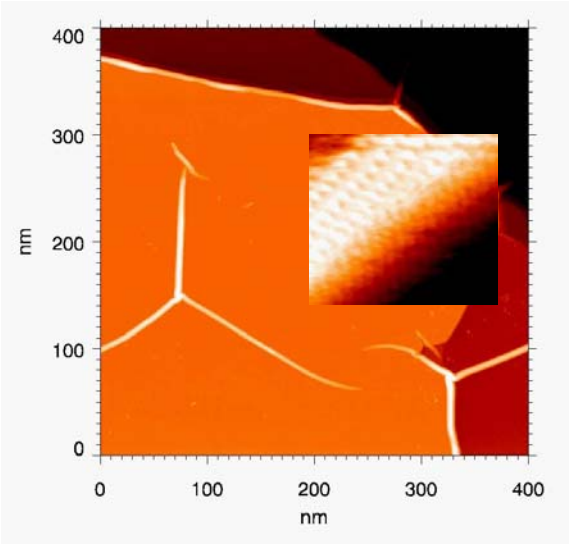

Figure 2: STM image of a SiC surface with single-wall carbon nanotubes grown on atomically flat terraces and alongside steps. The insert shows the atomic structure of a CNT.

We use high-temperature hydrogen etching of our SiC single-crystalline samples in a CVD reactor to get clean atomically flat terraces on the surface. The preparation continues in a multi-chamber UHV facility (figure 1) where designated surface reconstructions can be obtained by heating samples under a silicon vapor flux and verified by low energy electron diffraction (LEED). While heating in a silicon flux at temperatures <1000°C leads to a silicon rich (3×3) surface structure, annealing at higher temperatures causes a carbon rich, e.g. $(6\sqrt{3}\times6\sqrt{3})$R30°, surface structure.

Depending on the SiC polytype, cutting angle and heating conditions (usually temperatures >1500°C), various CNT arrangements can be attained on the substrate. Growth results are mainly gathered by in-situ scanning tunneling microscopy (STM).

Figures 2 and 3 show how CNTs can arrange on a SiC surface. They often attach alongside steps on the substrate and prefer to grow in the substrate's symmetry directions which you can take from the typical 120° angles at nanotube junctions. Y-junction CNTs as seen in figure 3 are of special interest for future nanoelectronic devices.

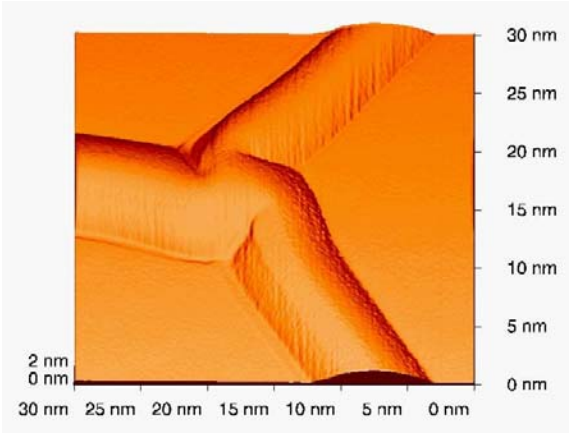

Figure 3: High-resolution STM image of Y-junction CNTs grown on SiC surfaces

Tube diameters can be determined by measuring the height in STM images, whereas width is usually broadened due to the tip shape. Taking their diameters of 1-2nm into consideration, the tubes turn out to be single-walled. CNTs grown on SiC tend to show a high purity in comparison to other techniques, because of the high growth temperature and the omission of catalysts that generally remain as defects in the tube structure.

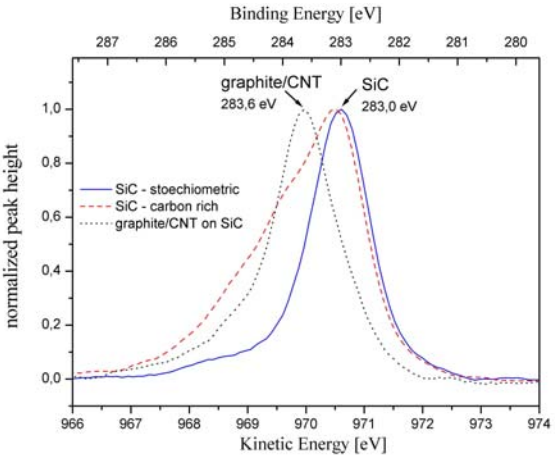

Figure 4: XPS spectra of the C 1s photoelectron signals after different SiC surface treatments

Complementing surface state information within the same vacuum is available by the use of x-ray photoelectron spectroscopy (XPS) from which you can gather quantitative information about surface composition and occurence of different bonding states. Thus, XPS provides an easy way to not only distinguish between carbon in the sp3-bonded SiC and the sp2-bonded graphite/CNT by comparing C1s photoelectron signals (figure 4), but also to gain knowledge about the top atomic layers' constitution.

Other treatments of silicon carbide are available in our SiC molecular beam epitaxy chamber (figure 5). In an UHV environment, heating the substrate up to 1600°C is possible. The in situ monitoring of the top surface regions of the sample via reflection high-energy electron diffraction (RHEED) is a main advantage of this facility, complementing our microscopy techniques.
With the built-in electron-beam heated evaporation sources, a well defined flux of silicon or carbon can be offered to prove new ways of generating carbon nanostructures. In addition, effusion cells for metals and semiconductor materials can be used to prepare nanostructures at surfaces and to investigate alternative catalytic growth procedures of carbon nanotubes.

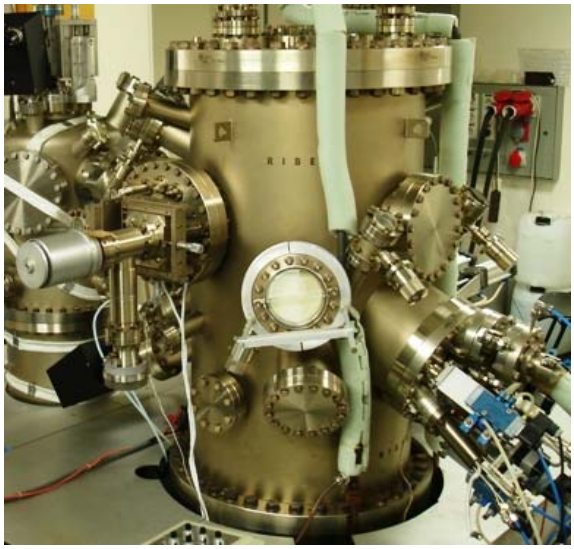

Figure 5: MBE growth chamber equipped with solid-source electron beam evaporators for carbon and silicon, effusion cells and RHEED

References:

[1] M. Kusunoki, T. Suzuki, T, Hirayamam N. Shibata, K. Kaneko: A formation mechanism of carbon nanotube films on SiC(0001), Appl. Phys. Lett. 77 (2000) 531.

[2] V. Derycke, R. Martel, M. Radosavljević, F.M. Ross, Ph. Avouris: Catalyst-Free Growth of Ordered Single-Walled Carbon Nanotube Networks, Nano Lett. 2 (2002) 1043.

Characterization of carbon nanotubes by X-ray photoelectron and Raman spectroscopy

M. Janietz, M. Steglich, T. Reichel, B. Schröter

Carbon nanotubes (CNTs) are unique nano-structures with exceptional electronic and mechanical properties [1]. Their assembling with selected features (diameter, chirality) at well-defined positions is an ultimate goal in nanotube research. Unfortunately, this has not been achieved yet. In consequence it is inevitable to study the properties and fabrication processes of CNTs.

Catalyst-assisted chemical vapor deposition (CCVD) is a technique most commonly used to grow carbon nanotubes on solid surfaces at about 700 to 1000°C. In our CCVD experiments a surface of SiO_2 covered with the catalyst (e.g. iron, cobalt, nickel) is placed in a quartz tube and heated inductively whilst flooding the reactor with methan as carbon feedstock and argon as carrier gas.

The CCVD technique can be optimized to grow CNTs of any low or high density on various substrate surfaces (fig.1).

Controlling the diameter of the nanotubes is more sophisticated. For this purpose it is necessary to control the size of the catalyst clusters as there is a close connection between nanotube diameter and catalyst particle size.

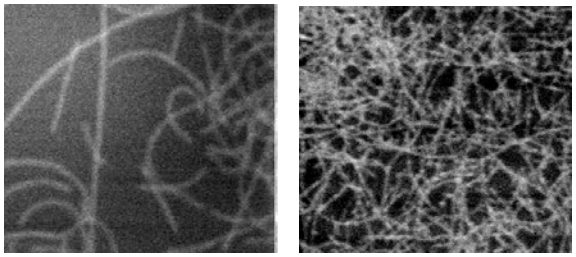

Figure 1: SEM images of CNTs grown by CCVD on silicon dioxide substrate.
Left: low density (10µm x 10µm),
right: high density (10µm x 10µm)

To characterize the samples we use scanning electron microscopy (SEM), X-ray photo-electron (XPS) and Raman spectroscopy.

XPS is based on the photoeffect, which means that electrons escape from the top atomic layers of the analysed material when it is irradiated by X-rays. The number of electrons and their kinetic energy is measured. Therefor XPS requires ultra-high vacuum conditions.

The high surface sensitivity of XPS (fig. 2 and 3) allows us to analyse qualitatively and quantitatively the state of the surface (bonding state and morphology as well as carbon modification and contaminations) before and after CCVD growth (fig. 4).

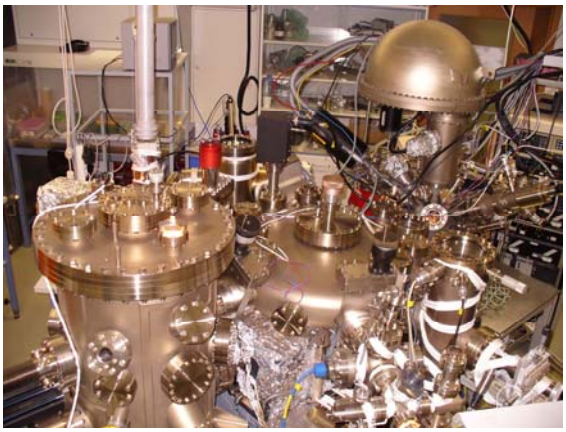

Figure 2: UHV multichamber equipment for surface preparation and characterization by electron spectroscopy and scanning tunnelling microscopy

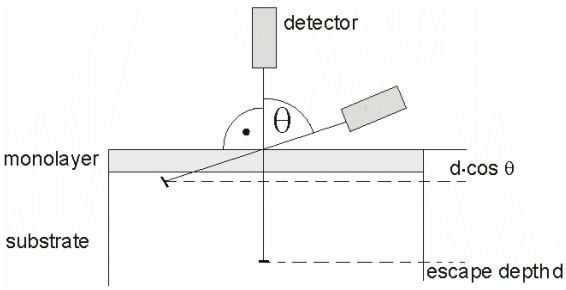

Figure 3: The electron escape depth grows with the angle between detector and sample. According to the very short inelastic mean free path the escape depth is only a few nanometers.

This information is provided by the peak intensity, position (electron binding energy) and line shape, respectively. Unfortunately, the difference of the C1s binding energies in carbon nanotubes and in graphite is rather small and difficult to resolve by XPS. Alternatively, by measuring the photoelectron intensities at various emission angle, we are able to differentiate between CNTs and layers of amorphous carbon or graphite deposited during CCVD growth.

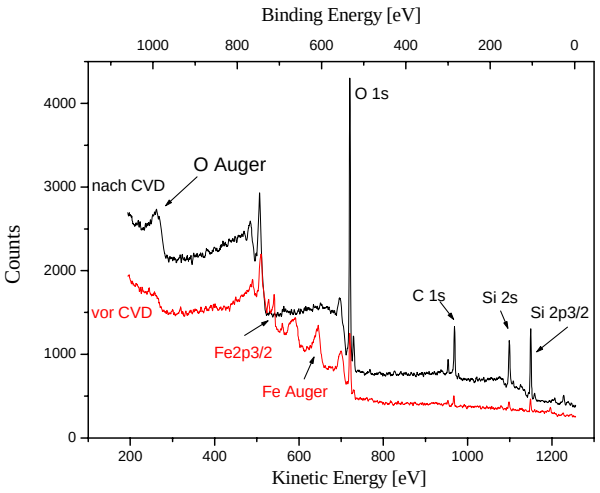

Figure 4: Wide range XPS scans of iron catalyst (lower curve) and carbon nanotubes on SiO_2 substrate. (X-ray excitation: Mg Kα :at 1253eV)

Raman spectroscopy is a powerful tool to investigate the electronic and phonon properties of CNTs (fig.5). Moreover, short-time measurements (a few minutes) in air make it the most common characterization tool for nanotube samples. It relies on inelastic scattering because of phonon excitation. This energy shift gives information about the phonon modes of the analysed system.

Figure 5: Raman spectrometer DILOR XY //*

A typical Raman spectrum of a CNT sample (fig.6 and 7) allows us to determine the quality and quantity of CNTs and the presence of further carbon modifications (graphite, amorphous carbon, fullerene) which show specific raman spectra.
It is even possible to distinguish between single- and multi-walled CNTs and to estimate the diameter distribution by studying the radial breathing mode (RBM, see fig.7), a concentric, breathing-like, in-phase oscillation of all carbon atoms, which is specific for CNTs. The frequency of the RBM is inversely proportional to the diameter. Another feature, the disorder induced D-mode, can be used to appreciate the defect concentration.

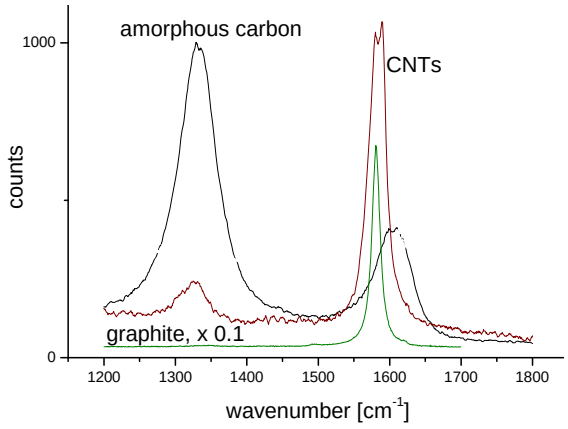

Figure 6: Raman spectra of different carbon modifications: CNT, graphite, amorphous carbon. (HeNe-laser excitation: λ = 632 nm)

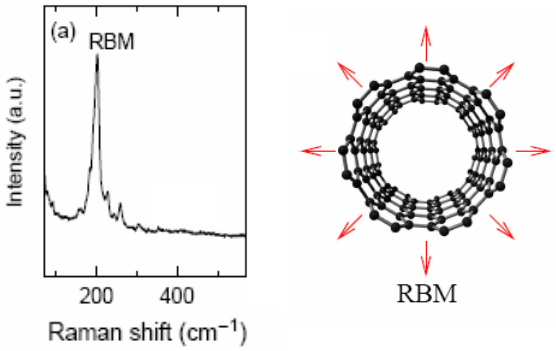

Figure 7: Exemplary Raman spectrum, which shows the RBM of single-wall CNTs, λ = 488 nm [2]

Optimizing and understanding the growth processes for CNTs with the help of characterization methods like XPS and Raman spectroscopy remain future challenges.

References:
[1] M. S. Dresselhaus, G. Dresselhaus, and P. Avouris, Carbon nanotubes: Synthesis, Structure, Properties and Applications, Berlin, Springer-Verlag, 2001.
[2] S. Reich, C. Thomsen, J.Maultzsch, Carbon nanotubes. Basic concepts and physical properties, Wiley-VCH, 2004.
* We thank the Astrophysics Institute for the possibility to accomplish Raman measurements.

The Growth of Carbon Nanotubes on Prestructured Substrates by Chemical Vapour Deposition

Thomas Reichel, Helga Rudolph, Matthias Steglich, Bernd Schröter

One-dimensional structures like carbon nanotubes (CNTs) are ideal materials for optical and electrical applications. We investigate the growth of aligned nanotubes or nanotube arrays to optimize their structure for optical, nonlinear-optical and luminescence applications. Furthermore, lithographic techniques have to be used to form contacts for electrical measurements.

CNTs are seamless cylinders composed of one or more concentric layers of carbon atoms in a honeycomb lattice arrangement. CNTs with more than one concentric layer are called multiwall carbon nanotubes (MWCNT). Single-walled nanotubes (SWCNT) typically have a diameter of about 0.7 nm to 5 nm and a length up to several micrometers.

Most of all applications require aligned carbon nanotubes at well-defined positions showing selected properties (like diameter, chirality, bandgap). However, a “directed assembling” or “controlled growth” of nanotubes is not possible so far.

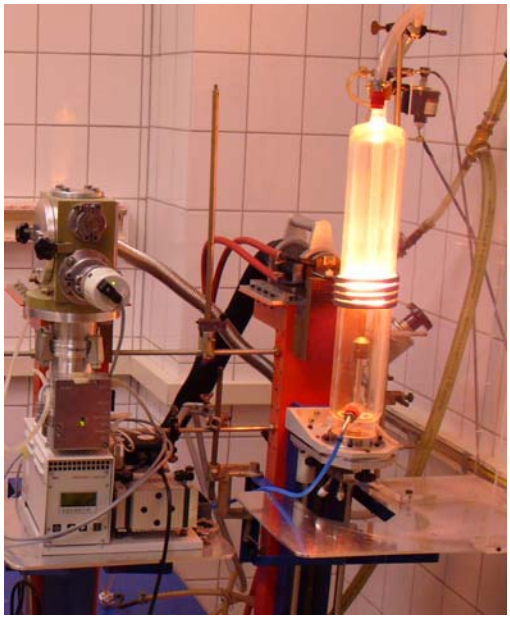

Figure 1: CVD reactor used to grow carbon nanotubes

Catalyst-assisted chemical vapour deposition (CCVD) is a growth technique most commonly used to grow carbon nanotubes on solid surfaces at about 500 to 1000°C. This method may be more or less compatible with standard thin-film and semiconductor technology. To catalyze the CNT growth metallic nanoclusters (e.g., iron, cobalt, nickel) are deposited on a surface. There seems to be a direct relation between the size of the catalyst cluster and the diameter of the nanotubes.

In our CCVD growth experiments we have used methan as carbon source and argon or hydrogen as carrier gas inductively heated in a quartz tube (figure 1).

A controlled growth of carbon nanotubes with particular properties like chirality at predefined positions is a prerequisite to utilize CNTs in electronic or nanooptical devices. CVD is the favored fabrication technique to grow CNTs directly on substrates with prestructured catalysts.

Our CVD facility consists of an inductively heated double-wall quartz tube furnace where we can supply different hydrocarbon gas mixtures. It allows to grow nanotubes in a temperature range up to 2000K, using argon and hydrogen as carrier gas and methane as carbon source. The Fe or Ni catalyst is vacuum evaporated onto the substrate and can be patterned by lithography or direct masking (figure 2).

By changing the partial pressures of carrier gas and carbon source, CNTs with high or low density can be grown on various substrate surfaces.

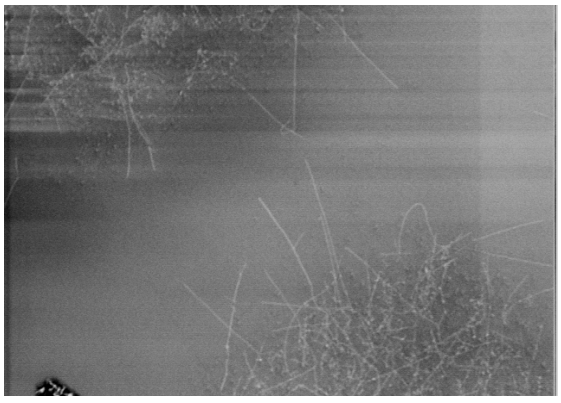

Figure 2: SEM images of CNT on SiO_2 substrate (100µmx80µm). Single long nanotubes can cross the patterned catalyst regions.

Synthesis and Measurement of Cobalt Cluster

Matthias Grube, Frank Schmidl, Paul Seidel

In order to synthesize carbon nanotubes (CNT) the presence of a catalysts is essential. The basic growth mechanism involves dissolving of carbon in metal clusters heated to high temperatures (600°C-1000°C) [1]. The three most important catalytic materials are the transition metals iron, nickel and cobalt. The metal clusters are created by a great variety of techniques, for example by vapour deposition of thin metal films, deposition of solutions or suspensions of different cobalt compounds on the substrate or by injection of organometallic substances into the growing chamber [2,3,4]. If one wants to control the growth of CNT's, it is necessary to control the catalyst. For example in CVD experiments one single walled carbon nanotube (SWNT) is formed from each catalyst particle and the diameter of the SWNT matches the size of the cluster [5,6].
In collaboration with the group "Dünne Schichten" within our institute the CNT's were grown by thermal CVD [7] using previously deposited thin Co films. Studies of annealed Co films were performed in order to understand the behaviour of the Co films during the CVD process.

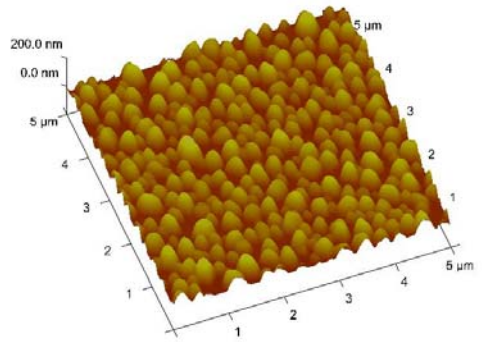

Figure 1: AFM-Image of a 11 nm thick Co film after annealing to 970°C (sample Co132-2)

Thin Co films (3 nm to 27 nm) were deposited by thermal evaporation. The Co was deposited on Si substrates covered by a 100 nm thick sputtered SiO2 layer and directly onto the Si. Afterwards the samples were annealed employing a boron nitride sample heater to different temperatures (600°C to 1000°C) in vacuum and at air atmosphere. We used an AFM to obtain images of the sample surfaces and evaluated the size distribution of the Co clusters of the different samples, see figures 1 and 2.

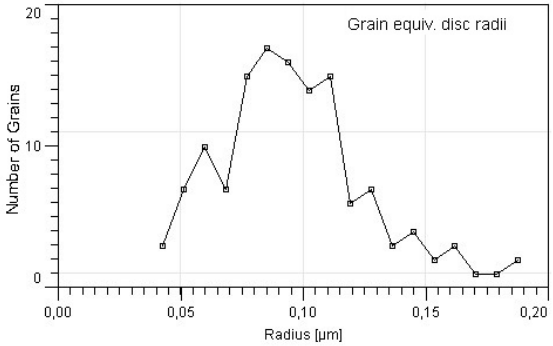

Figure 2: Distribution of the equivalent disk radius of the cluster (sample Co132-2)

We compared the results with respect to the temperature and film thickness for plain Si substrates and Si substrates with a sputtered SiO_2 layer. The results will be published in a diploma thesis soon.

[1] X. Fan, R. Buczko, A. A. Puretzky, D. B. Geohegan, J.Y. Howe, S.T. Pantelides, and S. J. Pennycook, 2003, Phys. Rev. Lett., 90, 145501

[2] Shengdong Li, Zhen Yu, Christopher Rutherglen, and Peter J. Burke, 2004, Nano Letters, 4, 2003-2007

[3] Pavel Nikolaev, Michael J. Bronikowski, R. Kelley Bradley, Frank Rohmund, Daniel T. Colbert, K.A. Smith, Richard E. Smalley, 1999, Chem. Phys. Lett., 313, 91

[4] N.M. Bulgakova, A.V. Bulgakov, J. Svensson, E.E.B. Cmpbell, 2006, Appl. Phys. A 85, 109

[5] T. Danis, M. Kadlecikova, A. Vojackova, J. Breza, M. Michalka, D. Buc, R. Redhammer and M. Vojs; 2006, Vaccum, 81, 22

[6] Y. Zhang, Y. Li, W. Kim, D. Wang and H. Dai, 2002, Appl. Phys. A, 74, 325

[7] B. Schröter, Th. Reichelt, H. Rudolph and W. Richter, *Directed growth of carbon nanotubes on solid surfaces,* Annual Report, 2005

Thin film systems for the growth of carbon nanotubes

M. Büenfeld, M. Grube, F. Schmidl, A. Tünnermann and P. Seidel*

** Insitute of Applied Physics, Albert-Einstein-Straße 15, 07745 Jena*

Since their discovery in 1991 carbon nanotubes (CNTs) show promising properties for electronic or optical applications. The nanotubes can be described as rolled up graphite layers. Therefore nanotubes can be divided in three groups: zigzag (a), armchair (b) and chiral (c) nanotubes depending on the rolling vector (figure 1; (d) shows the bonding structure of a nanotube) [1].

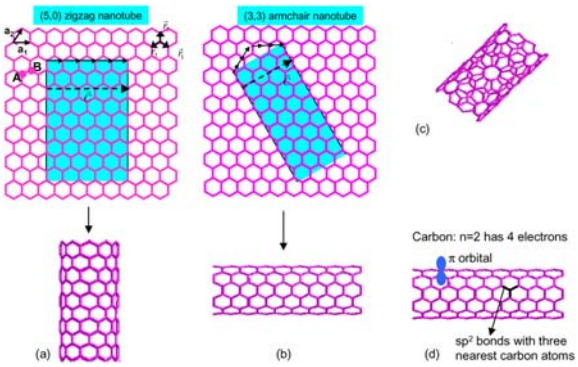

Fig. 1: *Possible "roll up" of carbon nanotubes [1]*

Carbon nanotubes can be divided in two types: single-walled CNTs (SWNTs) with one graphite layer or multi-walled CNTs (MWNTs) with multiple graphite layers. The typical diameter of SWNTs is about 1-3 nm. The nanotubes can be metallic as well as semiconducting depending on their graphite layer. This is caused by the structure of the nanotube and the electronic structure of the graphite layer.

The growth of carbon nanotubes needs nanoclusters of iron, cobalt, nickel or special compounds of these metals.

Combination of different materials (especially oxides or metals) show influence on the growth of the nanotubes.

The growth of the nanotubes itself is done by catalyst-assisted chemical vapor deposition (CCVD) at the group of Professor Richter within our institute [2]. Methane (CH_4) is used as carbon source.

At first 100 nm silicon dioxide (SiO_2) were sputtered on silicon substrate (Si). As catalyst a thin film of cobalt (Co) was evaporated on the layer of SiO_2 (figure 2). After this the structure has been placed in the CVD reactor. The CVD is performed by a temperature of about 1000 °C. Therefore the thin film of cobalt is melting and nanoparticles result from this film on the surface of the silicon dioxide.

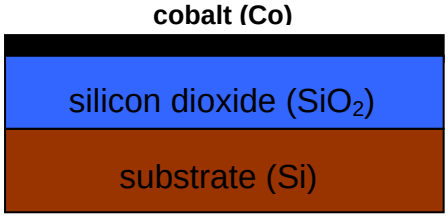

Fig. 2: *First structure to prove growth of carbon nanotubes*

After the CVD the growth of nanotubes is controlled by scanning electron microscopy (SEM). Nanotubes were found on the whole substrate.

The next investigated layer system has a structured silicon dioxide layer whereas cobalt is still evaporated on the whole system (figure 3).

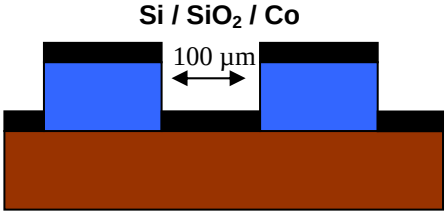

Fig. 3: *Structure to prove selective growth of carbon nanotubes.*

SEM pictures after CVD show that the nanotubes always starts to grow from the

silicon dioxide (figure 4). Additionally some of the CNTs grow over the edge of the silicon dioxide on the silicon substrate. The width of the trench is 100 µm. Some nanotubes had a length of this trench.

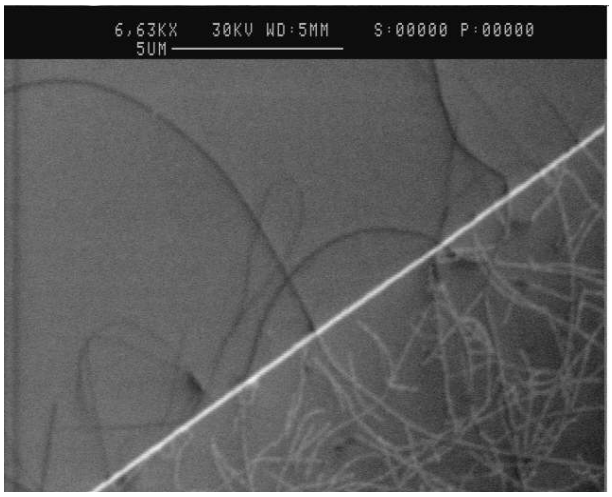

Fig. 4: *SEM picture of selective growth of carbon nanotubes. The CNTs always start to grow from the SiO_2 layer.*

Further on a silicon dioxide capped cobalt layer system was fabricated and the growth of CNTs was analyzed (figure 5).

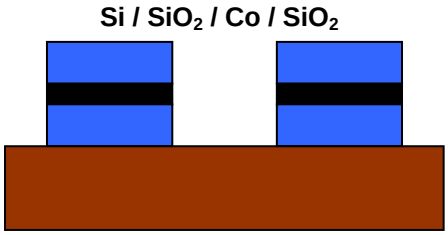

Fig. 5: *Layout with capped cobalt layer*

High resolution SEM pictures under a tilt of 20° show that the nanotubes do not start between the two silicon dioxide layers but at the top of the upper one (figure 6).

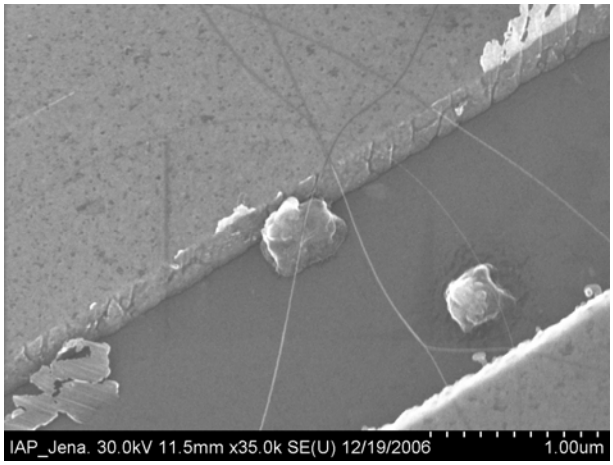

Fig. 6: *SEM picture of carbon nanotubes grown with the structure shown in figure 5*

The reason for this could be either diffusion of cobalt particles through the SiO_2 layer or the formation of a porous SiO_2 layer during the CVD process.
Additionally figure 4 shows that the nanotubes tend to form bundles, but the nanotubes disband again on the SiO_2 as well as on the Si. Other SEM pictures show that this bundling and disbanding happens very often.

In summary the first structures und material combinations show growth of carbon nanotubes with the possibility of selective growth starting points. Next steps are going to be the analysis of nanoparticles from different materials and the influence of other oxides.

References

[1] M. Anantram and F. Leonard, *Physics of carbon nanotube electronic devices*, Reports on Progress in Physics, 2006, 69, 507

[2] B. Schröter, Th. Reichelt, H. Rudolph and W. Richter, *Directed growth of carbon nanotubes on solid surfaces*, Annual Report, 2005

Electrical characterisation of Carbon Nanotubes

René Geithner, Holger Mühlig, Frank Schmidl, and Paul Seidel

Carbon Nanotubes (CNTs) are one-dimensional nanoscopic conductors with unique mechanical and electrical properties [1].
The electrical measurements are done on single-walled carbon nanotubes (SWNTs), which are electrically connected with gold (fig. 1).

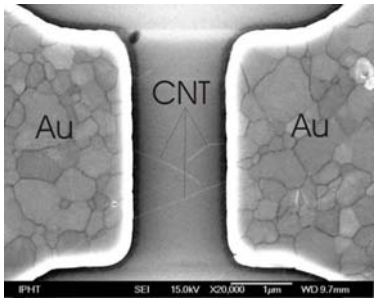

Fig. 1: *SEM image of CNTs contacted with gold*

A carbon nanotube field effect transistor (CNT-FET) is realized with a back-gate (fig. 2). Source-Drain voltage (V_{SD}) and gate voltage (V_G) is applied and the resulting source-drain current (I_{SD}) is measured.

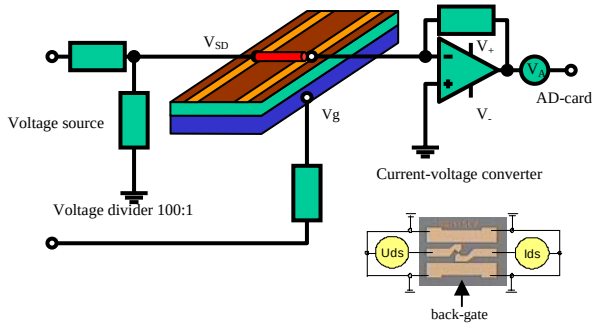

Fig. 2: *Measurement setup used for the electrical characterisation of CNT*

Measurements at room temperature show conductance of CNTs, which is dependent as well as independent from an applied gate voltage (figs. 3, 4). These results correspond to the picture of metallic and semiconducting CNTs. In the case of semiconducting CNTs, conductance variations about some order of magnitudes are achieved (fig. 3).

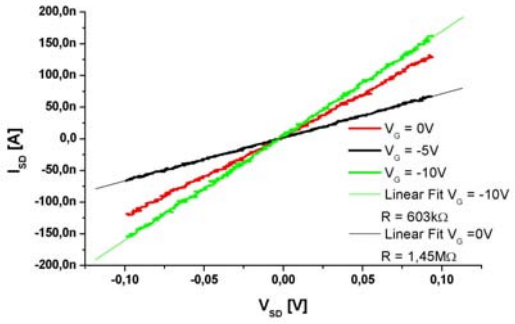

Fig. 3: *Semiconducting CNT at room temperature*
Source-Drain current as a function of source-drain voltage at different gate voltages
Conductance depends on gate voltage.

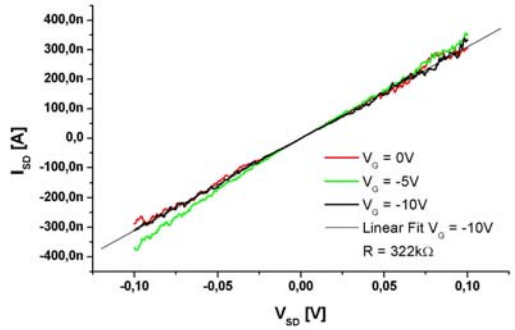

Fig. 4: *Metallic CNT at room temperature*
Source-Drain current as a function of source-drain voltage at different gate voltages
Conductance is almost independent from gate voltage.

At low temperatures a gap appears for all samples, where no source-drain current is detectable although a source-drain voltage is applied (figs. 5, 6). Quantum effects might be evidenced on a few samples [2]. These CNTs show Coulomb-blockade characteristics, which means that the conductance and the gap width oscillate with varying gate voltage (figs. 5 – 8).
Two types of measurements are done at low temperatures.

1. Source-drain current is measured by varying source-drain voltage and holding gate voltage constant (figs. 5, 6).
2. Source-drain current is measured by varying gate voltage and holding source-drain voltage constant (figs. 7, 8).

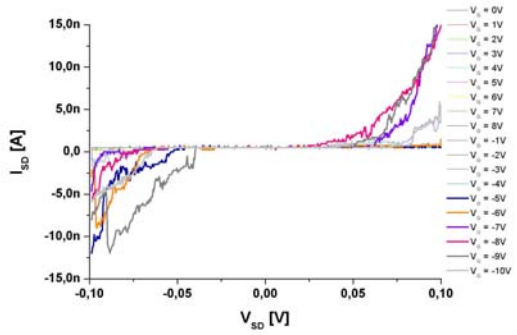

Fig. 5: *Semiconducting CNT at temperature below 20mK*
Source-Drain current as a function of source-drain voltage at different gate voltages
Conductance and gap width depends on gate voltage. CNT is blocking above applied gate voltage V_G = -5V.

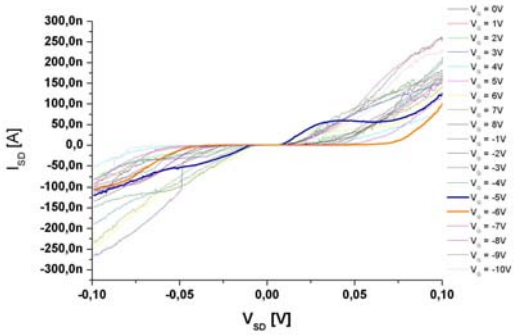

Fig. 6: *Metallic CNT at temperature below 20mK*
Source-Drain current as a function of source-drain voltage at different gate voltages
Conductance and gap width depends on gate voltage. CNT is conductive over the whole range of applied gate voltage.

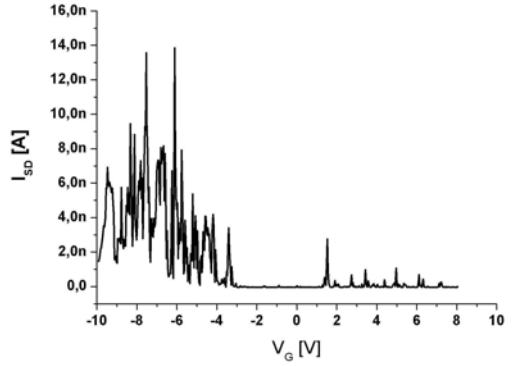

Fig. 7: *Semiconducting CNT at temperature below 20m*
Source-Drain current as a function of gate voltage at constant source-drain voltage V_{SD} = 100mV
Conductance oscillates with varying gate voltage. CNT is blocking above applied gate voltage V_G = -3V.

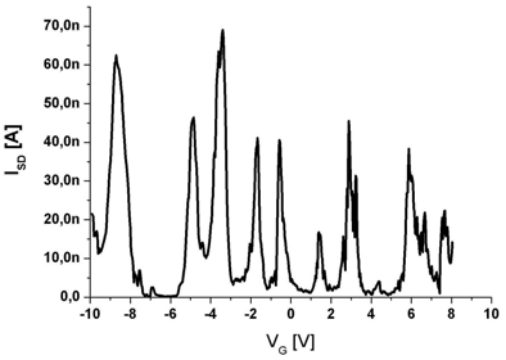

Fig. 8: *Metallic CNT at temperature below 20m*
Source-Drain current as a function of gate voltage at constant source-drain voltage V_{SD} = 25mV
Conductance oscillates with varying gate voltage over the whole rang of applied gate voltage.

For a metallic CNT the results of the two types of measurements are plotted together in a colourscale-graph. This shows so called “Coulomb-diamonds” (fig. 9).

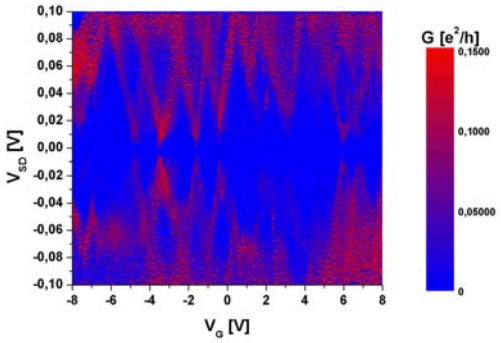

Fig. 9: *Conductance $G = dI_{SD}/dU_{SD}$ as a function of source-drain voltage and gate voltage for a metallic CNT. G is normalized to the maximum conductance of a mesoscopic conductor $G_0 = e^2/h$ (Landauer-Büttiker).*

Further work will concentrate on quantum effects and the appearing gap on other CNTs and their temperature depend behaviour.

[1] M. P. Anantram et al., Reports on Process in Physics 69, 507 -561, 2006
[2] B. Babic, Electrical Characterization of Carbon Nanotubes grown by the Chemical Vapor Deposition Method, Diss., University of Basel, 2004

Giant collective switching operations in current-voltage characteristics of Tl-2212 microbridges on vicinal $LaAlO_3$

Michael Mans, Henrik Schneidewind [a], *Matthias Büenfeld, Frank Schmidl, Paul Seidel*

a) *Institute for Physical High Technology (IPHT) Jena, P.O. Box 100239, D-07702 Jena, Germany*

We measured current-voltage characteristics of serial intrinsic Josephson junction (IJJ) arrays in a $Tl_2Ba_2CaCu_2O_{8+x}$ (Tl-2212) film microbridge on a 25° vicinal cut $LaAlO_3$ substrate. For electrical measurements, we used a low-noise source and measurement unit from Keithley. The wires were shielded by grounded covers. The samples were placed in liquid helium.

Experimental results

We measured IV characteristics with multibranch behaviour, which is typical for IJJs. For a few of the bridges we found giant collective switching operations over a voltage range of 1 to 5 V, which represents a simultaneous or nearly simultaneous switching of 50 to 300 junctions from the superconducting state into the resistive state (Fig. 1). Voltage driven measurements (Fig. 2) show the existence of branches inside the giant hysteresis. These branches are not stable in current-driven measurements. With current-driven time-resolved measurements (Fig. 3) we could identify the giant collective switching events as a fast succession of smaller collective events (2–50 junctions). Here "fast" is used comparable to the time resolution of current-driven measurements of the current-voltage dependence. The mean values of upward switching current $I_{S\uparrow}$ are typically in the range around 30 µA, with a standard deviation of 1.5 µA. The R_N values of single junctions range from 500 to 1000 Ω. The I_CR_N products are 10–20 mV and values of β_C range between two and ten.

Cause considerations

For T=0 all Josephson junctions are in the superconducting state and their phase difference rests in a local minimum of the washboard potential. In the case of intrinsic Josephson junctions, the superconducting CuO_2 planes are thin in comparison to the charge screening length. If the critical current is exceeded for one junction, its phase difference starts to rotate. This causes charging effects [1,2] in adjacent junctions and the phase differences of these junctions in turn begin to oscillate. This oscillation leads to a coupling of the junctions, which can no longer be considered to be independent from each other. Different quasiparticle branches are associated with different patterns of rotating and oscillating junctions [3]. For small finite temperatures, the superconducting state shows thermal activated oscillations of the phase difference.

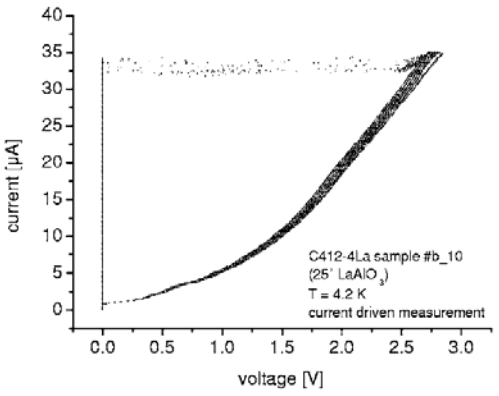

Figure 1: Accumulated (10 single bidirectional measurements) current-voltage dependencies of 2x2 µm microbridges of Tl-2212 films on vicinal $LaAlO_3$ with a misorientation angle of 25°. Measurements are current driven.

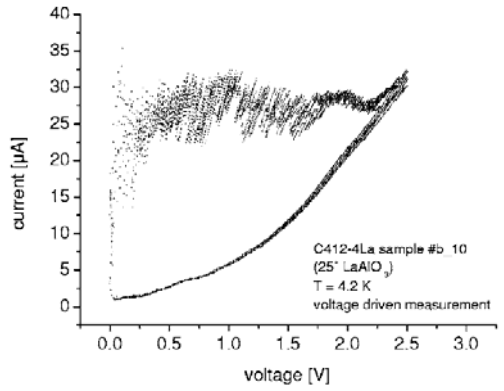

Figure 2: Accumulated (10 single bidirectional measurements) current-voltage dependencies of 2x2 µm microbridges of Tl-2212 films on vicinal $LaAlO_3$ with a misorientation angle of 25°. Measurements are voltage driven.

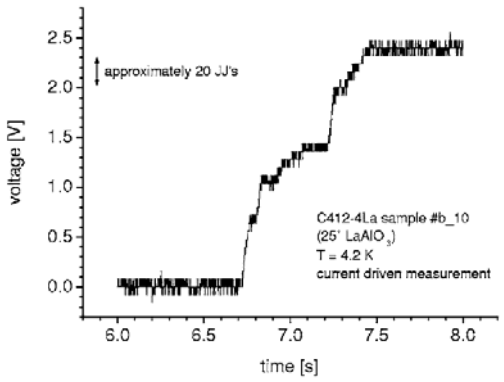

Figure 3: Time dependent measurement of the giant collective switching events reveals their successive character. It comprises a number of smaller collective switching operations.

The collective switching events can be explained as follows:
An initial junction starts to rotate, which causes oscillating phase differences in the neighbouring junctions. The strength of these oscillations increases the closer these neighbours are to the rotating junction. These neighbours have only a slightly higher critical current than the rotating junction. This assumption is consistent with the model of the microbridge as an array of subarrays as described in Ref 6. We assume that the spread of the critical currents between the junctions in a subarray is very small. This again is consistent with the results of the voltage-driven measurements. If the neighbours of the rotating junction have only a slightly higher critical current, their washboard potential is so far tilted that even a small perturbation, such as an induced additional oscillation, is sufficient to raise these neighbouring junctions also into the rotating state [4]. The β_C values from two to ten are sufficient to keep the return current small enough for the stabilization of the rotating state. The process of a successive switching of the neighbouring junctions will continue until a junction with a much higher critical current is reached.

One attribute of giant collective switching is the very small spread of the critical currents of the Josephson junctions which switch together. Due to this small parameter spread, the occurrence of phase locking is very likely [5], which is an important precondition of future applications.

Further details of this work are published in Ref. 6.

This work was partially supported by the German DFG, Contracts Nos. Se 664/10-3 and Schn 599/2-3. Michael Mans is grateful to the Foundation of the Evangelisches Studienwerk Villigst e.V. for their support.

References:

1 T. Koyama and M. Tachiki, Phys. Rev. B **54**, 16183 (1996)

2 D. A. Ryndyk, Phys. Rev. Lett. **80**, 3376 (1998)

3 H. Matsumoto, S. Sakamoto, F. Wajima, T. Koyama, and M. Machida, Phys. Rev. B **60**, 3666 (1999)

4 T. A. Fulton and L. N. Dunkleberger, Phys. Rev. B **9**, 4760 (1974)

5 A. N. Grib, P. Seidel, and J. Scherbel, Phys. Rev. B **65**, 094508 (2002)

6 M. Mans, H. Schneidewind, M. Büenfeld, F. Schmidl, and P. Seidel, Phys. Rev. B **74**, 214514 (2006)

Influence of microwave irradiation power on current–voltage characteristics of intrinsic Josephson

Yuri M. Shukrinov [a] *, Michael Mans, Jens Scherbel* [b] *, Paul Seidel*

a) Permanent adress: BLTP, JINR, Dubna, Moscow Region, 141980, Russia
b) Now at: X-FAB Semiconductor Foundries AG, Haarbergstr. 67, 99097 Erfurt, Germany

For our experiments [1] we used a serial intrinsic Josephson junction (IJJ) array in a $Tl_2Ba_2CaCu_2O_{8+x}$ (Tl-2212) film submicron bridge on a 20° vicinal cut $LaAlO_3$ substrate.

For electrical measurements, we used a low-noise source and measurement unit from Keithley. The wires were shielded by grounded covers. The samples were placed in a continuous-flow-type cryostat with a window for microwave input. The RF irradiation of 93 GHz was supplied by a Gunn diode connected with a tunable attenuator and a horn antenna. A MgO lens was glued on the sample for direct measurement of the RF response. The use of the MgO lens only allowed measurements in two-probe geometry. However, this is not a problem due to the small contact resistance and the use of superconducting feed lines to feed-in the microbridge.

We measured current-voltage characteristics (IVC) with multibranch behaviour, which is typical for IJJs. For the junctions with the smallest I_C values we found a collective switching operation. The typical I_C values are in the range of some μA, the R_N values are range from 2 to 3 kΩ and β_C is approximately 10.

For no and small microwave irradiation power P < 15 μW (see figure 1) we can verify a collective switching operation for 4 IJJs.

Irradiation with a higher power of 100 μW effects a splitting of the collective into smaller groups, where the switching current of the lower group is decreased, while the switching current of the upper group is increased.

The IV curve for a microwave power of 400 μW shows a further splitting with the same behaviour for the switching currents.

For a microwave power of 1100 μW, the IV curve shows that the increasing switching current of the upper is not related to the splitting but to the increasing irradiation power itself. The superconducting branch is fully suppressed.

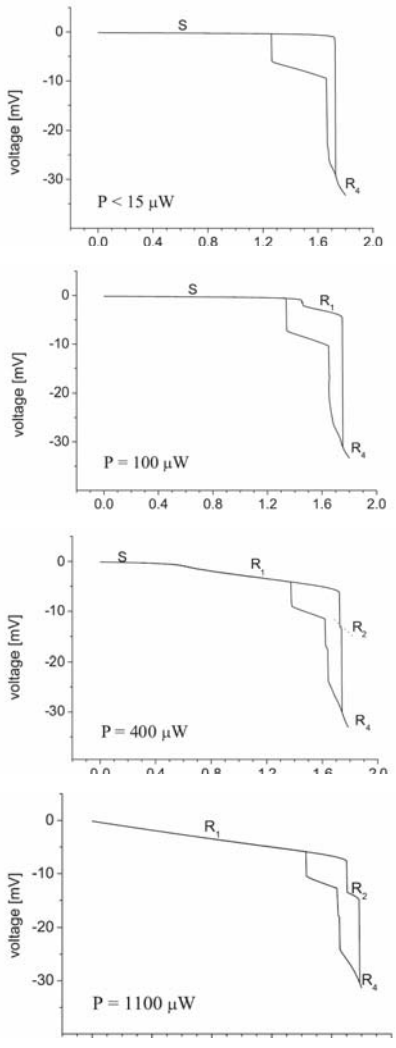

Figure 1. The current-voltage characteristics of microbridge IJJs. The characteristic is recorded by one current sweeping from 0 to 1.8 μA and backward. The Rn denote the number of resistive junctions.

For a better understanding of this behaviour, we simulated the current-voltage characteristics in the framework of the capacitively coupled Josephson junction model (CCJJ). In the CCJJ model [2, 3] the resistive state in IJJs is realized as a state with a definite number of rotating (R-) or oscillating (O-) states. If the l^{th} junction has a rotating phase, the time average of $\partial\varphi(l)/\partial t$ is constant and that of $\sin(\varphi(l))$ is zero. If the l^{th} junction has an oscillating phase, the time average of $\partial\varphi(l)/\partial t$ is zero and that of $\sin(\varphi(l))$ is constant, where $\varphi(l)$ is the gauge invariant phase difference of the l^{th} Josephson junction and t is the time. The O-state is one of the new elements which appear in IJJs in comparison with the case of a single JJ. The O-state can be realized if there are more than two junctions in the stack.

The shape of the current–voltage characteristic is determined by the McCumber parameter β_C and by the competition of the 'current effect', the 'gap suppression effect' [7] and gap (critical current) suppression by radiation. If one of the intrinsic junctions switches into the R-state, then a non-equilibrium quasiparticle distribution is induced in the neighbouring junctions which are in O-states.

Inhomogeneity of the distribution of charge imbalance leads to the quasiparticle current through the neighbouring junctions, and because of that the supercurrent through these junctions is decreased and a larger external current is needed to switch these junctions into the R-state. This is the 'current effect'.

The decrease in the gap leads to a decrease of the critical Josephson current. So, transition to the R-state occurs at smaller value of the superconducting current. This is the 'gap suppression effect'.

If the current effect is more effective than the gap suppression effect we find an enhancement of the branching in the IVC. In the opposite case, when the gap suppression effect is more effective than the current effect we measure single hysteresis in the IVC.

This effects and the influence of microwave irradiation can be described by dynamic equations with generalized Josephson relations.

$$\frac{\hbar}{2e}\dot{\varphi}_l = V_l + \alpha\left(2V_l - V_{l-1} - V_{l+1}\right)$$

$$with \quad \alpha = \varepsilon\mu^2/sd$$

$$\beta_C\,\partial^2\varphi_l/\partial t^2 = I/I_C + A\cos ft - \partial\varphi_l/\partial t - \sin\varphi_l + \alpha\left(\sin\varphi_{l+1} + \sin\varphi_{l-1} - 2\sin\varphi_l\right)$$

Here I and V_l are the current through and voltage over the l^{th} junction, I_C is the critical current, ε and d are the dielectric constant and the width of the insulating layer, μ and s are the charge screening length and the width of the superconducting layer, A and f are the amplitude and the frequency of the microwave irradiation.

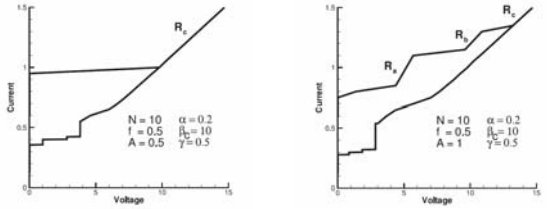

Figure 2. The IVC of 10 IJJs with parameters N = 10, β_C = 10, α = 0.2, γ = 0.5 under irradiation with frequency f = 0.5 and amplitudes A = 0.5 (left) and A = 1 (right).

Numerical simulation based on the framework of the CCJJ model [4] could reproduce our measurements (see figure 2).

This work was supported by Heisenberg–Landau Program, by the German DFG, contract no. Se 664/10-3. Michael Mans is gratefully acknowledged for financial support of the Foundation of the Evangelisches Studienwerk Villigst e.V

References:

1 J. Scherbel , M. Mans, H. Schneidewind, U. Kaiser, J. Biskpek, F. Schmidl and P. Seidel, Phys. Rev. B **70**, 104507 (2004)
2 T. Koyama and M. Tachiki, Phys. Rev. B **54**, 16183 (1996)
3 M. Machida, T. Koyama and M. Tachiki, Physica C **300**, 55 (1998)
4 Yu. M. Shukrinov, M. Mans, J. Scherbel, P. Seidel, Supercond. Sci. Technol. **20** S74 (2007)

Influence of internal shunts on current-voltage characteristics of Tl-2212 microbridges on vicinal $LaAlO_3$ substrates

Michael Mans, Henrik Schneidewind [a], *Matthias Büenfeld, Frank Schmidl, Paul Seidel*

a) *Institute for Physical High Technology (IPHT) Jena, P.O. Box 100239, D-07702 Jena, Germany*

We measured current-voltage characteristics of serial intrinsic Josephson junction (IJJ) arrays in a $Tl_2Ba_2CaCu_2O_{8+x}$ (Tl-2212) film microbridge on a 15° vicinal cut $LaAlO_3$ substrate. For electrical measurements, we used a low-noise source and measurement unit from Keithley. The wires were shielded by grounded covers. The samples were placed in liquid helium.

Experimental results

We measured current-voltage characteristics with multibranch behaviour, which is typical for IJJs.

The 15° microbridges show small collective switching operations mostly between 10 to 20 mV(see Figure 1) In the lower part of the characteristic, the backward tracing of the current-voltage dependency show that these collective events are due to two to six single junctions, which return into the superconducting state both individually as well as collectively. In current-driven measurements these collective switching operations appear as zones without branches in the hysteretic regions. However, voltage-driven measurements show that branches exist in this region, which are not stable in the current-driven case. The branch which is associated with the lowest backward switching current $I_{S\downarrow}$ shows the largest return interval in the voltage range. All other return intervals in the lowest hysteretic region are smaller. In the upper part of the characteristic we found branches which become narrower and narrower. Both are typical behaviour for a serial array of Josephson junctions with a shunt [1]. The critical current density of our Josephson junctions can be estimated as 50 kA/cm^2 which is much higher than the typical values of 8 kA/cm^2 for vicinal Junctions on 20° or 25° substrates.

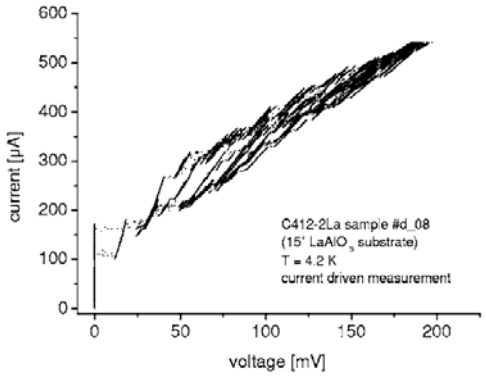

Figure 1: Accumulated (20 single bidirectional measurements) current-voltage dependencies of 2x2 µm microbridges of Tl-2212 films on vicinal $LaAlO_3$ with misorientation angles of 15°

Cause considerations

Two types of resistive shunts are possible: external and internal shunts. The existence of an external shunt can be explained by an incomplete removal of a gold layer, which is necessary for film protection during the fabrication process and for the electrical contacting. The angular dependence of the sputter plasma during the film deposition is different from that of the Ar^+ ion beam during the etching process. This may lead to shadowing effects, which would leave small areas on the sample with incomplete gold removal. Since no gold residues could be found by light microscopy and since the resistivity of the bridges at room temperature did not indicate the presence of resistant shunts, these areas must be very small. If there are such gold residues, they will act as resistive shunts for a small group of Josephson junctions, which is not necessarily a disadvantage.

We showed in several publications [1,2] that such resistive shunts are able to promote phase locking if their resistances are in the range of the normal resistance of the Josephson junctions.
A second possibility is the existence of internal shunts. Such internal shunts may be provided by several kinds of disturbed areas. In films with 15° misorientation angle, we found areas that show the typical morphology of c-axis films, i.e., with the c-axis perpendicular to the surface normal. This can be observed by light microscopy. We cannot exclude the possibility that besides such microscopic c-axis fractions, nanoscopic c-axis fractions might exist as well, which are not detectable in light or secondary electron microscopy. In the same manner, we can discuss other disturbed areas such as interface layers and grain boundaries.[3] If such areas are located alongside or on top of the bridge, they act as resistive or even as superconducting shunts and could explain the branch narrowing. The higher critical current densities of the 15° films can also be explained with such nanoscopic shunts.

Further details of this work are published in Ref. 4.

This work was partially supported by the German DFG, Contracts Nos. Se 664/10-3 and Schn 599/2-3. Michael Mans is grateful to the Foundation of the Evangelisches Studienwerk Villigst e.V. for their support.

References:

1 A. Grib, M. Mans, J. Scherbel, M. Büenfeld, F. Schmidl, and P. Seidel, Supercond. Sci. Technol. **19**, S200 (2006)

2 A. Grib, M. Mans, J. Scherbel, F. Schmidl, and P. Seidel (Phys. Rev. B submitted)

3 J. Scherbel, M. Mans, H. Schneidewind, U. Kaiser, J. Biskupek, F. Schmidl, and P. Seidel, Phys. Rev. B **70**, 104507 (2004)

4 M. Mans, H. Schneidewind, M. Büenfeld, F. Schmidl, and P. Seidel, Phys. Rev. B **74**, 214514 (2006)

Temperature dependent Néel relaxation (TMRX) measurements for characterization of nanoparticle distributions

M. Buettner, T. Mueller, S. Prass, M. Mans, F. Schmidl and P. Seidel

We conducted measurements on magnetic nanoparticles produced by project partners to determine the energy barrier distribution and the resulting particle size.

The average particle size can be calculated from the position of the peak (or the peaks, if several were found) of the energy barrier distribution according to [1] :

$V_{\max} = \frac{20 k_B T}{K}$, where k_B is the Boltzmann constant, K the anisotropy constant taken from literature, T the temperature of the peak in the energy barrier distribution, and the factor 20 resulting from the magnetization time that was used. The particles are assumed to have a spherical shape for the calculation of their diameter and radius.

To determine the average particle volume in the maximum of the energy barrier distribution more accurately as well as to adjust the results for the uncertainties originating in the temperature dependence of the anisotropy constant (due to the temperature dependence of the coercive field strength used to calculate the anisotropy constant), it is necessary to measure the susceptibility of the samples with high accuracy in a temperature range from room temperature to 4.2 K. In cases where this was not possible, numbers from literature were used (values for K are usually given for bulk material, so it is not clear if these values hold true for the nanoparticles used).

The preparation of the nanoparticles is of great importance to ensure that the theoretical requirements for the samples are met.

The currently favoured preparation is lyophilisation with Mannitol (a sugar substitute), this method was also recommended to our partners [2].

This method is necessary to ensure sample stability over the whole measuring range of 4 K to 330 K. The lyophilisation should also ensure that the particles have the required minimum distance of ≥ 5d [2]. If this criterion is not met, the signal from the relaxation of the individual nanoparticles is more and more overshadowed by the interaction between the magnetic fields of the different particles. This effect would render the theoretical model used as basis for the calculation of the nanoparticle diameter from the energy barrier distribution useless and therefore lead to wrong values for the diameter.

The optimal quantity of material to be measured is between 1 µmol and 10 µmol (10^{-5} mol to 10^{-6} mol) iron (Fe). In principle, it would be possible to measure in a much larger range of 10^{-4} mol to 10^{-7} mol iron, but very low quantities of iron lead to difficulties with signal detection (the unshielded measurements may be subject to large external disturbances) while large quantities overload the input sensitivity of our SQUID system and require changes in our measurement setup.

The samples analysed until now in the Biodiagnostics project were produced by the Royal Institute of Technology (KTH) in Stockholm. According to the accompanying data sheet, the particles consist of γ-Fe_2O_3 and were coated with a shell of oil-acid. 60.8mg of their sample were filled into our 30 µl sample holder.

We conducted temperature dependent magnetorelaxometry measurements which yielded the following magnetic flux densities given in Fig. 1.

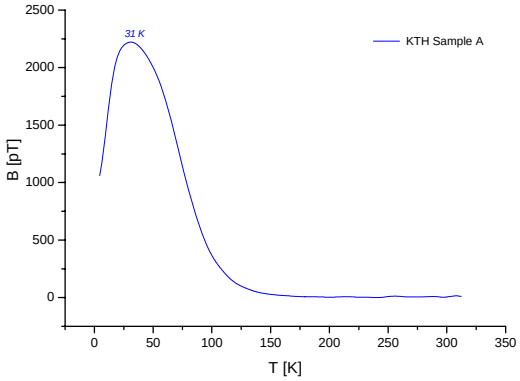

Figure 1: measured flux densities at different temperatures

The measured B(T) were then converted into the equivalent values for the energy barriers. The result is shown in the energy barrier distribution given in Fig. 2.

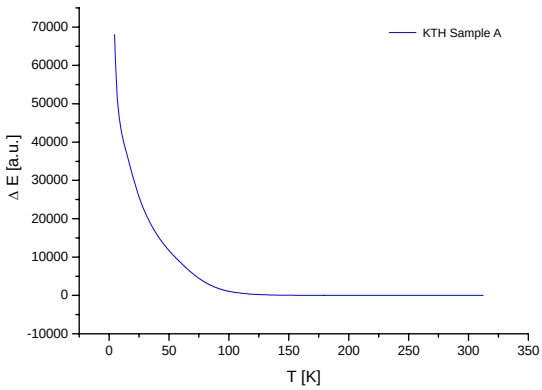

Figure 2: Energy barrier distribution

From the peak of the energy barrier distribution at $T \leq 5$ K we calculated that the average particle diameter must be $\leq$ 6 nm. The TEM analysis conducted by the project partner (KTH) yielded an average particle diameter of 10 nm. As our measurement is only sensitive to the magnetic part of the nanoparticles while the TEM detects both the magnetic core as well as the unmagnetic shell, we suspect a significant magnetic dead layer.

Another possibility would be that the prerequisite of particle distances of $\geq$ 5d is not met in the sample, leading to interactions between the magnetic fields of different particles and therefore a shift of the peak in the energy barrier distribution to smaller temperatures. If this interpretation is correct, the diameter calculated from our TMRX measurements would be closer to the 10 nm result from TEM measurements [2].

Further research concerning the interaction of the nanoparticles will be done as one of our next steps.

This work was partially supported by the EC (project BIODIAGNOSTICS , contract no. 017002).

References

[1] E. Blums, A. Cebers, M.M. Maiorov, *Magnetic Fluids,* Walter de Gruyter Berlin New York, S. 22 ff. (1997)

[2] F. Schmidl, M. Büttner, T. Köttig, S. Prass, C. Becker, M. Mans, J. Heinrich, M. Röder, K. Wagner, D. V. Berkov, P. Görnert, P. Weber, G. Glöckel, W. Weitschies, P. Seidel, accepted for publication in J. Magn. Mag. Mater.

[3] D.V. Berkov, *Evaluation of the energy barrier distribution in many particle systems using the path integral approach*, J. Phys.: Condens. Matter 10, L89-L95 (1998)

[4] F. Schmidl, M. Büttner, T. Müller, S. Prass, T. Köttig, P. Weber, M. Mans, C. Bocker, J. Heinrich, K. Wagner, M. Röder, D.V. Berkov, P. Görnert, G. Glöckel, W. Weitschies, P. Seidel, *Temperature dependent Néel relaxation (TMRX) measurements for characterization of nanoparticle distributions,* 7th German Ferrofluid workshop, Benediktbeueren, 2006

Characterization of the energy barrier distribution of Fe_2O_3 – particles imbedded in a glass matrix by temperature dependent Néel relaxation (TMRX) measurements

T. Müller, M. Büttner, F. Schmidl, S. Prass, M. Mans, C. Worsch[1], P. Seidel

[1] *Otto-Schott-Institut für Glaschemie, Friedrich-Schiller-Universität Jena, D-07743 Jena Germany*

The energy barrier distribution of a system containing magnetic nanoparticles is one of the most important parameters, for information about magnetic properties, particle size distributions and particle interactions can be derived from it. One way to obtain the energy barrier distribution of such a complex particle system is the interpretation of Néel relaxation signals [1]. For ferrofluid systems, this method has delivered acceptable results and thus was utilized to characterize the magnetic properties of magnetic particles imbedded in a glass matrix as well.

The available glass samples were manufactured in the Otto – Schott – Institute for glass chemistry by melting down a mixture of the following oxides at 1400 °C for 60 minutes:

Oxide	quantity [Mol%]
Na_2O	12
Al_2O_3	12
B_2O_3	14
SiO_2	37
Fe_2O_3	25

Table 1: composition of glass mixture

The obtained molten material was quenched in cold water and the resulting flakes were used for further analyses, see Fig. 1.

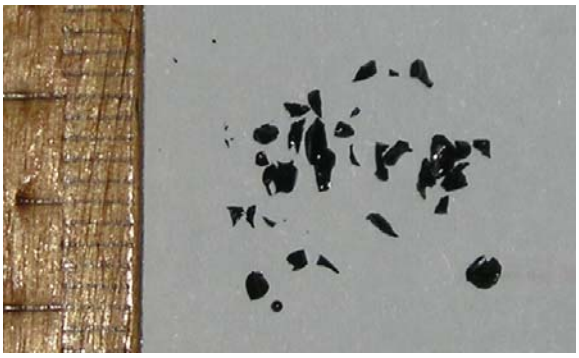

Figure 1: glass flakes, fabricated by melting down the raw mixture (table 1)

TEM – examinations (Fig. 2) showed roughly spherical resolidified areas, where Fe_2O_3 particles are presumed to be concentrated.

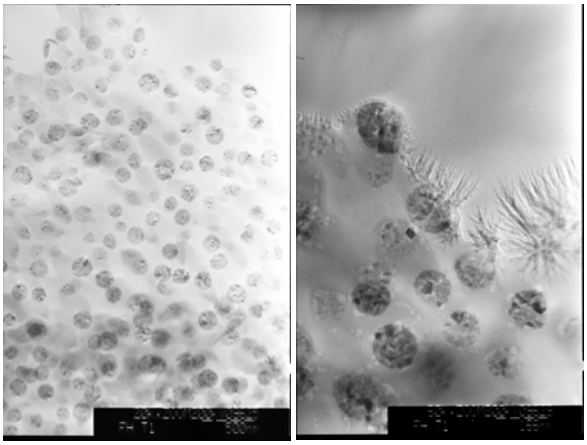

Figure 2: TEM – picture of glass sample designated V7

TMRX – measurements of the glass samples delivered interesting results for the energy barrier distribution, see Fig. 3.

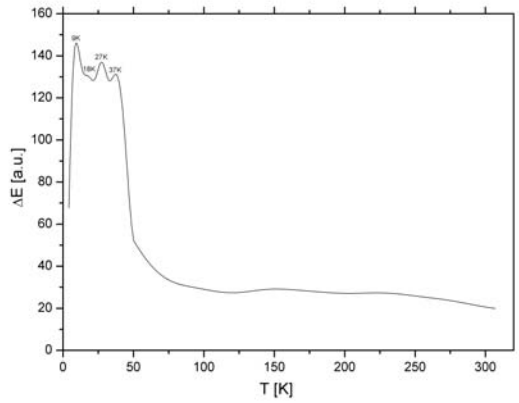

Figure 3: Energy barrier distribution of Fe_2O_3 – particles in glass matrix

The large peak from 4,2 K to 50 K could result from magnetic interaction between the particles [2].

Just as interesting, however, is the existence of the smaller local maxima on top of the primary peak. They occur at 9K, 18K, 27K and 37K and thus appear to be roughly periodically.

Outlook

For better interpretation of the measurement results as shown in figure 3, further analyses of the examined glass flakes are inevitable. Especially structure detecting measurements of the glass samples, preferably at cryogenic temperatures, could prove themselves to be invaluable in the process of finding an explanation for the observed sample behavior.

This work was partially supported by the EC within contract no. 017002 (BIODIAGNOSTICS).

References

[1] E. Romanus, D.V. Berkov, S. Prass, C. Groß, W. Weitschies, P. Weber, *Determination of energy barrier distributions of magnetic nanoparticles by temperature dependant magnetrelaxometry*, Nanotechnology 14 (12), 1251 – 1254, (2003)

[2] D.V.Berkov, *Evaluation of the energy barrier distribution in many - particle systems using the path integral approach*, J. Phys. Condens. Matter 10, 89-95, (1998)

Improvement of the spatial resolution of a magnetic relaxation measurement system (MRX)

F. Schmidl, M. Büttner, S. Prass, T. Müller, C. Becker, A. Steppke, T. Grumpelt, P. Seidel

The measurement setup for the determination of Néel relaxation of immobilized magnetic nanoparticles consists of a single-channel second order dc-SQUID gradiometer operating at 4.2 K and a Helmholtz coil system to magnetize the sample [1].
To improve the spatial resolution of the system down to the mm range, we focused on two features: decrease of the warm-cold distance and use of an additional flux concentrator.
For the determination of the spatial resolution of the system it is necessary to use well-defined test samples as calibration standards. The samples must be lyophilized, thereby immobilizing the particles to avoid Brownian relaxation in the sample.
The measurement system initially had a spatial resolution of about 20 mm due to the large warm-cold distance between sensor (at 4.2 K) and sample surface (room temperature) of about 20 mm in the old He dewar. A test measurement with two blocks (20x20x20 mm^3, distance from each other: 54 mm) of lyophilised ferrofluid materials with a concentration of 1 µmol iron is shown in Figure 1.

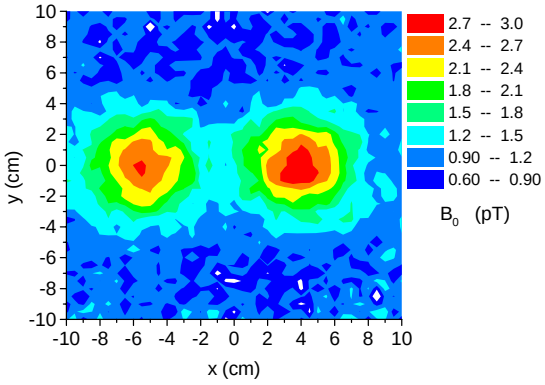

Figure 1: Measured spatial resolution of the old system

To overcome the obstacle of the large separation between sample and gradiometer, a new cryostat with a warm-cold distance of less than 5 mm was built. To determine the performance of the new arrangement, we are currently taking comparison measurements on one sample.
A second approach towards improving the special resolution was the use of ferromagnetic needles as flux concentrators of flux focusers in our measurement equipment (see Fig. 2)

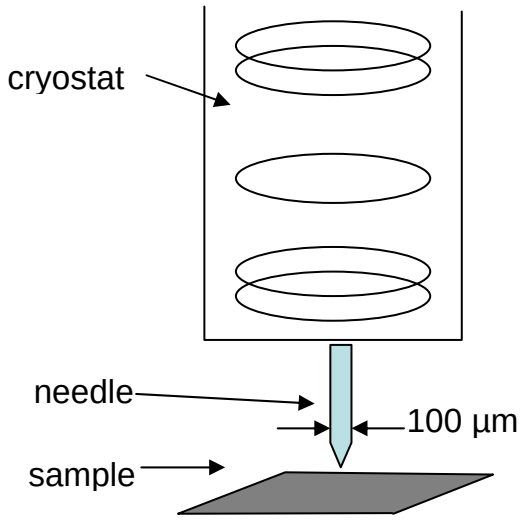

Figure 2: Scheme of the SQUID system with a ferromagnetic needle

The practical use of small ferromagnetic needles with a diameter down to several micrometers is well known from high-temperature SQUID microscopy [2].
This setup is commonly used only for measurements of static fields with planar gradiometers/magnetometers. Our idea was to transfer this setup with ferromagnetic needles, see Fig. 3, to magnetorelaxometry measurements.

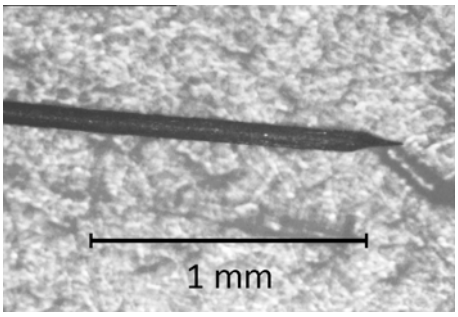

Figure 3: Light microscope picture of the needle

To determine the magnetic properties (with and without a magnetization field), we characterized them in our system for nondestructive testing [3]. Figure 4 shows the measurement of the magnetic field distribution of a needle which was placed vertically on the sample holder and then scanned underneath the HTSL gradiometer in the cryostat [4].

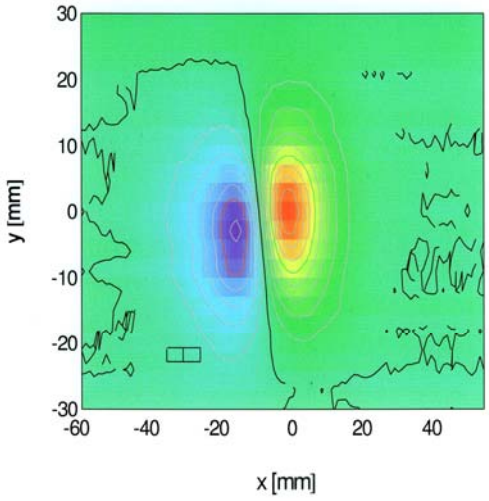

Figure 4: Scan of a ferromagnetic needle in our test system for non-destructive evaluation [3]. The planar SQUID gradiometer is oriented perpendicular with respect to the needle

The balance of the high-sensitivity second-order gradiometer is severely disturbed by the ferromagnetic needle. The position of the needle with respect to the gradiometer's rotationally symmetrical antennas as well as the distance between needle and gradiometer had be individually adjusted and optimized for each single needle dependently upon the needle's shape, size and magnetic properties.
We therefore designed a nonmagnetic and non-metallic adjustable needle holder, similar to those employed in optical systems for lenses and mirrors. This enabled us to reliably reproduce the positioning of a needle while allowing modifications for different needles.
First measurements with well-adjusted needles showed an improvement of the spatial resolution of about one order of magnitude with the same or even better sensitivity as before.

Acknowledgments

This work was supported by the EU project BIODIAGNOSTICS (contract No. 17002)

References

[1] E. Romanus, M.Höckel, C.Groß, S.Prass, W.Weitschies, R.Bräuer, P.Weber, J.Magn.Mag.Mater 252 (2002) 387
[2] S.A. Goudoshnikov, B. Yu. Luibimov, Yu. V. Deryuzhkina, L.V. Matveets, O. V. Snigirev, A. S. Kalabukhov, M.L. Ranchinski, F. Schmidl, P.Seidel, Physica C 372-376 (2002) 166
[3] F. Schmidl, S. Wunderlich, L. Dörrer, H. Specht, S. Linzen, H. Schneidewind, P. Seidel, IEEE Trans. Appl. Supercond. 7, 2756-2759 (1997)
[4] P. Seidel, S. Wunderlich, F. Schmidl, L.Dörrer, S. Linzen, F. Schmidt, F. Schrey, C. Steigmeier, K. Peiselt, S. Müller, A. Förster, S. Lösche, S. Goudoshnikov, IEEE Trans. Appl. Supercond. Vol. 11 (2001) 1176

LTS-SQUID based measurement tool for characterization of superconductive RF cavities

W. Vodel, R. Neubert, S. Nietzsche, R. Nawrodt, K. Knaack[†], K. Wittenburg[†], and A. Peters[††]

[†]Deutsches Elektronen Synchrotron Hamburg, [††]Gesellschaft für Schwerionenforschung Darmstadt

I. Introduction

Due to development of the TESLA technology [1] there was a large increase of the gradient of superconducting cavities. Criterion for good performance is not only the quality factor Q, but also a low rate of field emission. The field emission is the reason for the so-called dark current, which consists of particles emitted by field emission, which are captured by the accelerating fields of the cavity. Since this current can be emitted at arbitrary locations in the accelerator, dark current does not fit in energy, and thus gets lost in focusing elements close to its origin. This results in additional cryogenic loss and activation of components. Therefore, dark current often is the parameter that puts practical limits to the cavity performance.

In order to develop the preparation procedures for further increase of the technically possible gradients, or guarantee a given performance during a larger production series, field emission or dark current has to be controlled during the fabrication process. The device presented here provides the necessary resolution and bandwidth to measure on the pA level. Due to the already existing cryogenic environment there is no additional complication.

The linear accelerator technology, based on superconducting L-band (1.3 GHz) cavities, is currently under study at DESY [1]. The two 10 km long main LINACs (linear accelerator) are equipped with a total of nearly 20,000 cavities. A gradient of 23.4 MV/m is required for a so-called superstructure arrangement of couples of 9-cell cavities, higher gradients up to the physical limit at 50 MV/m are desired. The dark current, due to emission of electrons in these high gradient fields, is an unwanted particle source. Therefore, the mass production of high-gradient cavities with minimum field emission requires a precise, reliable measurement of the dark current in absolute values. The presented apparatus senses dark currents in the nA range. It is based on the cryogenic current comparator (CCC) principle, which includes a highly sensitive LTS SQUID system as magnetic field sensor. Further on the setup contains a Faraday cup and will be housed in the cryostat of the CHECHIA cavity test stand and mounted at a temperature of 1.8 K.

II. Cryogenic Current Comparator

In principle, the Cryogenic Current Comparator (CCC) is composed of three main components:

– The superconducting pick-up coil,
– the highly effective superconducting shield, and
– the high performance LTS-SQUID system (for more details see [2]).

The CCC, first developed by Harvey in 1972 [3], is a non-destructive method to compare two currents with high precision using a meander shaped flux transducer. Only the azimuthally magnetic field component, which is proportional to the current in the wires, will then be sensed by the pick-up coil. All other field components are strongly suppressed. The very small magnetic flux coupled into the coil is mostly detected by a SQUID.

The design of the CCC for measuring of dark currents is realized as co-operation of DESY Hamburg, Jena University and GSI Darmstadt. The apparatus will be placed in the CHECHIA cavity test stand and operated at 4.2 K.

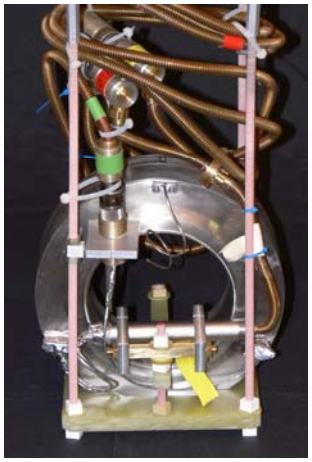

Fig. 1. Nb pick-up coil prepared for preliminary

III. Results

Test measurements of the completed pick-up coil with all special cabling and feed throughs (see Fig. 1) at 4.2 K were successfully done in a wide-neck cryostat at the cryogenic laboratory of Jena University. As signal source a current generator was used to simulate the expected dark electron beam pulses. Supplying the calibration coil with a calibrated current pulse the current sensitivity of the CCC system of 200 nA/Φ_0 was achieved which is in a good agreement with the designed value of 175 nA/Φ_0.

Fig. 2 shows a plot of the simulated beam signal generated by a programmable current generator with the amplitude of 340 nA (rise time: 300 µs, flat top: 950µs, fall time: 300 µs). The response signal of the SQUID system was 1.7 Φ_0 corresponding to a current sensitivity of 200 nA/Φ_0.

The spectral flux noise density of the

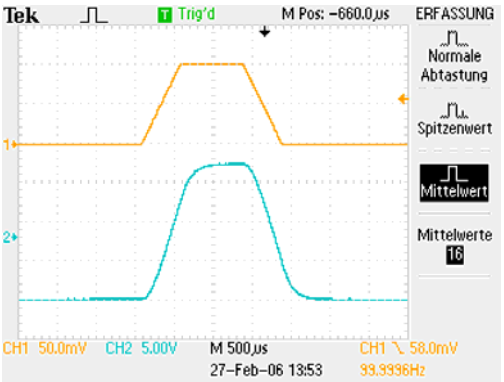

Fig. 2. Simulated beam signal (upper curve) and SQUID output signal (lower curve).

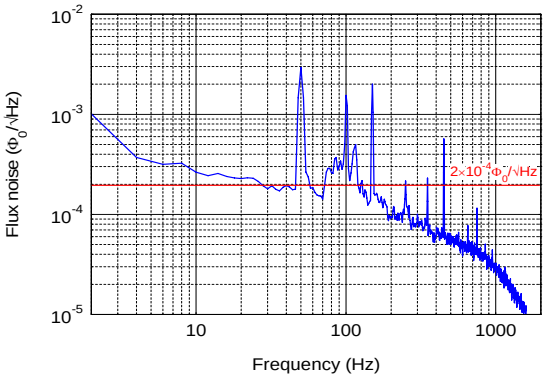

Fig. 3. Noise spectrum of the CCC within a bandwidth from 1 Hz to 1600 Hz. Low pass filter: 1 kHz.

system in the frequency range between 1 and 1600 Hz was measured using a HP spectrum analyzer in the laboratory at Jena University and a level of 2×10^{-4} $\Phi_0/\sqrt{\text{Hz}}$ was observed (see Fig. 3). For these measurements a low pass filter with a cut-off frequency of 1 kHz was used. This flux noise level corresponds to a noise limited current resolution of 40 pA/√Hz.

Preliminary tests of the CCC at DESY were successfully done. As a result of the rough measurement conditions at DESY a noise limited current resolution of the CCC of 500 pA/√Hz could be achieved. This is, above all, a result of the external electrical disturbances and mechanical vibrations caused by numerous machines and other equipment of the test facility.

Long-term measurements of the output voltage of the CCC to detect flux drifts, caused for instance by temperature drifts of the core material, showed a sufficient small drift of $< 2 \times 10^{-5}$ Φ_0/s.

The complete CCC is now ready for use and the final commissioning of the apparatus in the CHECHIA test stand is planned within the next months. The start of the dark electron beam measurements to qualify the superconductive accelerator r.f. cavities is foreseen in spring 2007.

IV. References

[1] R. Brinkmann, TESLA Technical Design Report.

[2] W. Vodel, K. Mäkiniemi, "An ultra low noise SQUID system for biomagnetic research", ***Measurement Science and Technology***, Vol 3, No 2, pp. 1155-1160, Dec. 1992

[3] I. K. Harvey, "A precise low temperature dc ratio transformer", ***Rev. Sci. Instrum.***, vol. 43, p. 1626, 1972.

Characterization and measurements with HTSL Flip-Chip gradiometers

C. Becker, A. Steppke, T. Foerster, H. Schneidewind, V. Grosse, R. Pietzcker, F. Schmidl, and P. Seidel*

*Institut für Physikalische Hochtechnologie e.V. (IPHT), Bereich Magnetik-Quantenelektronik, Albert-Einstein-Straße 9, D-07745 Jena

We have fabricated planar dc-SQUID gradiometers and flux transformers operating in different environments. The design allows the independent fabrication and optimization of readout gradiometers on one side and flux transformers based on a single superconducting layer on the other side.

Our flip-chip configuration consists of a readout dc-SQUID gradiometer made from $YBa_2Cu_3O_{7-x}$ (YBCO) on a 10x10 mm² $SrTiO_3$ (STO) bicrystal substrate which is inductively coupled to a flux transformer [1]. The $Tl_2Ba_2CaCu_2O_{8-x}$ (TBCCO) thin films of the flux transformer were prepared on 2" lanthanum aluminate (LAO) substrates in a two step process [2].

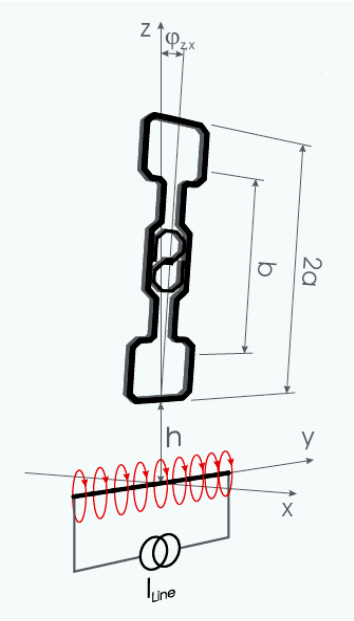

FIGURE 1: Schematic view for determination of effective area with known magnetic field of the wire line with current I_{Line}. B is the baseline and 2a is the length of the flux transformer.

The most important parameter for practical applications is the field gradient resolution of the investigated dc-SQUID sensor combinations [4]. To determine this parameter for different gradiometer layouts we measured their noise properties in unshielded as well as magnetically or electrically shielded environments.
With the values of the noise spectrum $\sqrt{S_\phi}$ we can calculate the field gradient resolution $\sqrt{S_G}$ with

$$\sqrt{S_G} = \frac{\sqrt{S_\Phi}}{b \cdot A_{EFF}}.$$

Our goal is to optimize the layout and properties of the read-out gradiometer together with the flux transformer to reach a high field gradient resolution in unshielded environments for the non-destructive evaluation (NDE) [3].

We measured the signal of a known magnetic field distribution (shown in figure 1) with a line scan. With a fit of this graph (figure 2) we can calculate the effective areas of our sensors.

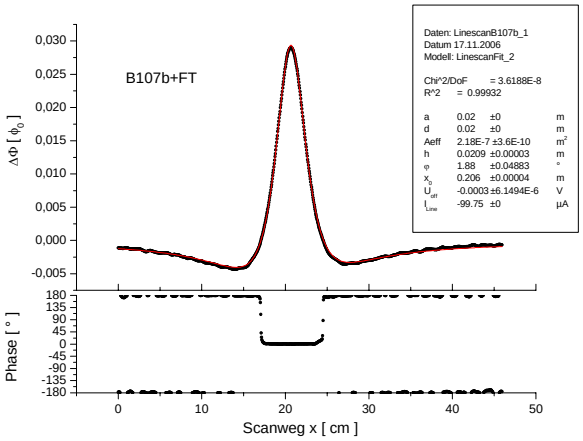

FIGURE 2: Line scan characteristic of a flip-chip-gradiometer for determination of effective area. The insert shows fit of the interesting parameters.

To increase the spatial resolution we have to decrease the distance between the sensors and the sample.

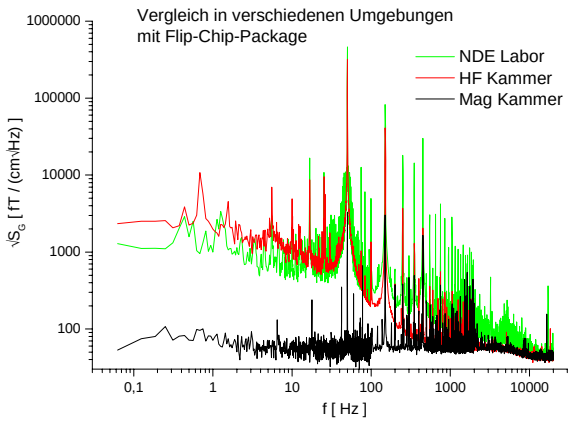

FIGURE 3: Field gradient resolution characteristic of a flip-chip-gradiometer (YBCO ~200 nm thickness on a 10x10 mm²STO substrate) with flux transformer (TBCCO ~280 nm thickness on a 40x8 mm² LaAlO substrate) in unshielded environment, magnetically and electrically shielded environments.

With a fixed warm-cold distance it is not possible to increase the spatial resolution by decreasing the distance between sensor and measured object.
Therefore have to increase the signal amplitude in the sensor. With a ferromagnetic probe we could have increase the signal with factor 5. Figure 4 shows an area scan from a magnetic field of a cylinder coil, measured with a flip-chip gradiometer and a ferromagnetic probe.

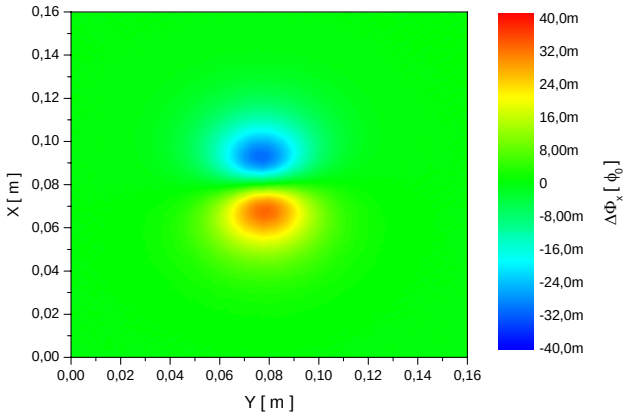

FIGURE 4: Area scan of magnetic field gradient from a cylinder coil with the flip-chip package. To increase the spatial solution [5,6] used a ferromagnetic probe.

Further we designed a new planar dc-SQUID gradiometer layout for area scans. The characterization of these new sensors with I-U-curves and noise measurements were successful finished.

√S_B [fT/(cm√Hz)]	unshielded @1 Hz	unshielded white	magnetically shielded @1 Hz	magnetically shielded white
B107B	3000	2500		
B107B with FT	880	110	65	50

Table 1: Field gradient resolution of the flip-chip-gradiometer with flux transformer and without, in unshielded and magnetically shielded environments.

We are able to characterize our sensors by measuring the effective areas and the field gradient resolution. With these results it was possible to measure magnetic field distributions of various samples. To increase the spatial resolution we used a ferromagnetic probe as a flux concentrator.
The authors would like to thank L. Redlich (IPHT Jena) for laser patterning of our samples. Partially supported by EU commission (contract BIODIAGNOSTICS 017002)

[1] P. Seidel, F. Schmidl, C. Becker, U. Springborn, S. Biering, V. Grosse, T. Foerster, P. Lorenz and R. Bechstein, *Planar high-temperature superconducting dc-SQUID gradiometers for different applications*, Supercond. Sci. Technol. **19** (2006) pp. 143-148

[2] P. Seidel, T. Foerster, H. Schneidewind, C. Becker, V. Grosse, A. Steppke, P. Lorenz, R. Pietzcker, and F. Schmidl, *Comparison of high temperature superconducting gradiometers using flip chip YBCO and TBCCO antennas*, IEEE Trans. Appl. Supercond (submitted)

[3] M. J. Zhang, P. L. Lang, Z. H Peng, Y. F. Chen, K. Chen, and D. N. Zheng, *High-Tc planar SQUID gradiometer for eddy current non-destructive evaluation*, Chinese Physics **15** (2006) pp. 1903-1906

[4] P. Seidel, C. Becker, A. Steppke, T. Foerster, S. Wunderlich, V. Grosse, R. Pietzcker, F. Schmidl, *Noise properties of high-temperature superconducting dc-SQUID gradiometers*, Physica C (will be published)

[5] B. Baek, S. H. Moon, Su-Young Lee, S. M. Lee, J. I. Kye, H. J. Lee and Z. G. Khim, *Investigation of a magnetic flux-guide for a HTS scanning superconducting quantum interference device microscope*, Supercond. Sci. Technol. **17** (2004) pp. 1022-1025

[6] T. Hayashi, H. Wang and H. Itozaki, *High-sensitivity detection of static magnetic field in a SQUID probe microscope*, Supercond. Sci. Technol. **19** (2006) pp. 271–275

Noise properties and characteristic parameters of dc-SQUID gradiometers for a flip-chip configuration

Alexander Steppke, Christoph Becker, Tobias Förster, Veit Große, Frank Schmidl and Paul Seidel

Measuring small magnetic fields in unshielded environment is still a challenge for magnetic field sensors. For applications like magnetocardiography [1], low-field NMR, non destructive evaluation and the characterisation of magnetic nanoparticles [2], [3] high temperature superconducting (HTS) dc-SQUID magnetometers and gradiometers have been developed in the last years.

The field gradient resolution of our sensors depends on the effective area (A_{eff}) of the sensor which is sensitive to magnetic fields. The size of available bicrystal substrates ($SrTiO_3$) limits the size of the gradiometer antennas. To increase the sensitivity we developed dc-SQUID gradiometers in a flip-chip configuration[4].

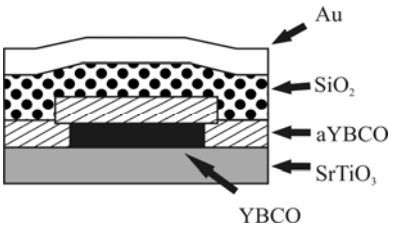

Fig. 1. Scheme of the multilayer system at the crossover region prepared in our new technology

In several steps we developed a new preparation technology for the readout gradiometers in a multilayer setup (see Fig. 1). This enables us to use a gold crossover to connect the sensor to the flux-locked-loop electronics without unwanted leakage current between the top gold layer and the superconducting antenna [5].

The readout gradiometers were characterized by measuring the critical current I_C, voltage modulation with different bias currents I_b. The measured values for the critical current density are in the range of $5 \cdot 10^3$ A/cm^2 to $5 \cdot 10^4$ A/cm^2 at 77 K for a 24° grain boundary angle. The corresponding $I_C R_N$ products from 90 µV up to 310 µV are in agreement with the experimental data from the planar dc-SQUID gradiometer without SiO_2 insulation.

As a first step to characterise the noise properties we measured the voltage noise (see Fig. 2). In a second step we measured the flux noise in shielded environment. The spectral density of white flux noise $\sqrt{S_\Phi}$ lies in the range of 13.5 $\mu\Phi_0/\sqrt{\text{Hz}}$ and at 1 Hz $\sqrt{S_\Phi}$ is in the range of 36 $\mu\Phi_0/\sqrt{\text{Hz}}$.

We used flux transformers with $Tl_2Ba_2CaCu_2O_{8-x}$ (TBCCO) and $YBa_2Cu_3O_{7-x}$ (YBCO) as superconducting thin film materials for the flip-chip antennas.

The combination of our new readout-gradiometer with the TBCCO antennas emerged as a suitable combination. The growth structure of TBCCO thin

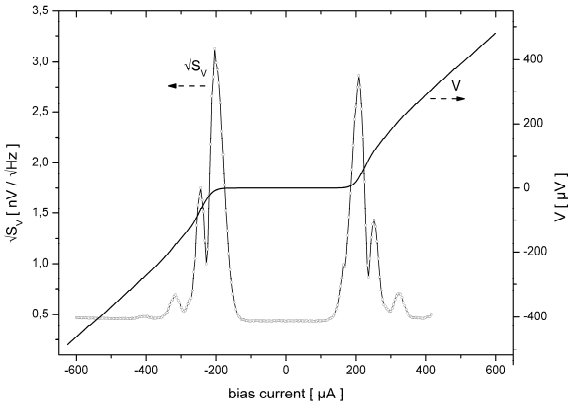

Fig. 2. Voltage noise and I-V-curve of the prepared readout gradiometers depending on the bias current at 77 K

films contains a number of structural defects which act as pinning centres for Abrikosov vortices. An enhanced pinning results in a decreased rate of vortex jumps in the film which leads to a lower noise.

With this sensor we can calculate a field gradient resolution of approximately 800 fT/cm/√(Hz) at 1 Hz in an unshielded laboratory environment for the complete device. This results show that the new sensor is suitable for high-sensitivity applications such as biomagnetism.

[1] R. Weidl, S. Brabetz, F. Schmidl, F. Klemm, S. Wunderlich, P. Seidel, *Supercond. Sci. Technol.*, 10 1997, 95

[2] E. Romanus, N. Matoussevitch, S. Prass, J. Heinrich, R. Müller, D.V. Berkov, H. Bönnemann, P. Weber. . *Appl. Organometal. Chem.* 18, 2004, 261

[3] M. Schmidt, H.-J. Krause, M.Banzet, D. Lomparski, J. Schubert, W. Zander, Y. Zhang, R. Akram, M. Fardmanesh. . *Supercond. Sci. Technol.*, 2006, 19, 261

[4] K. Peiselt, S. Wunderlich, F.Schmidl, F. Schrey, C. Steigmeier, U. Hübner, P. Seidel, *Physica C.* , 2002, 378-381, 1385

[5] P. Seidel, C. Becker, A. Steppke, T. Foerster, S. Wunderlich, V. Grosse, R. Pietzcker, F. Schmidl, *Physica C.* (accepted for publication)

Epitaxial Growth of ZnO films on YBCO by Pulsed Laser Deposition

R. Pietzcker, F. Schmidl and P. Seidel

Although the wide-bandgap semiconductor zinc oxide (ZnO) has been studied for 60 years, it has received much attention in very different fields over the last ten years: it seems a suitable replacement of GaN for optical applications in the blue and near-UV spectrum; its resistivity is tunable through doping over a wide range (10^{-4}-$10^{9}\Omega$cm), making it promising for both low-resistivity applications like transparent conducting oxides (TCO) and – together with its piezoelectric effect – high-resistivity applications like surface acoustic wave guides (SAW); furthermore, its large exciton binding energy of 60meV should allow lasing with a low threshold.

To contribute to the investigations on dielectric films on $YBa_2Cu_3O_{7-x}$ (YBCO), the growth of ZnO thin films on YBCO will be studied here.

Layer	p_{O2} [Pa]	T_S [°C]	I_L [Jcm^{-2}]	f [Hz]
YBCO	10	755	65	5
ZnO	10	350	45	5

Table 1: Parameters for the deposition of the YBCO and ZnOO films. p_{O2} is the oxygen partial pressure, T_S the substrate temperature during deposition, I_L is the laser fluence at the target and f is the pulse rate of the excimer laser (λ=248 nm).

The deposition parameters for on-axis Pulsed Laser Deposition (PLD) of YBCO films on 5x10 mm^2 strontium titanate (STO) substrates were optimised towards multilayer fabrication: Surface smoothness and good crystallinity took precedence over superconducting properties. 200 nm thin films produced with the determined parameters (see table 1) showed a good c-axis orientation with a full width at half maximum (FWHM) of the rocking curve of $\Delta\omega$<0.2° for $YBCO_{005}$ (several films had FWHM <0.1°). AFM measurements showed smooth surfaces with an rms-roughness of (4.5±1.5) nm. Four-point probe measurements were used to determine T_c^0 to (87±1) K and ΔT_c to 1K.

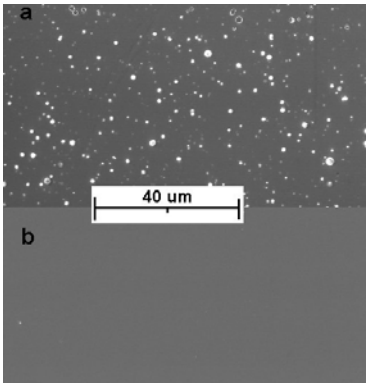

Figure 1: SEM pictures (SE mode) (a) YBCO film made with old PLD setup, showing high droplet density (b) almost droplet-free YBCO film after change of PLD setup

Part of the optimisation process was a change to the PLD setup to decrease droplet densities on the YBCO film. Through a decrease of laser fluence, the extension of the optical path and a slight defocusing of the laser spot on the target, the droplet density was decreased by a factor of about 20, down to 5*10^4 cm^{-2} for 200 nm thin films. The improvement can be seen in the SEM pictures shown in fig. 1.

On these YBCO layers 130-1000nm thin ZnO films were *in situ* deposited at temperatures between 200 and 500 °C and oxygen partial pressures of 1-10 Pa. All films showed c-axis growth, although the crystallinity varied widely and showed a strong dependence on the substrate temperature, as can be seen in fig. 2. The surfaces mostly showed an rms-roughness of (6 ± 2) nm. At high deposition temperatures, a deterioration of the YBCO base layer could be detected through XRD analysis. Therefore, the optimal deposition parameters were determined to the values seen in table 1.

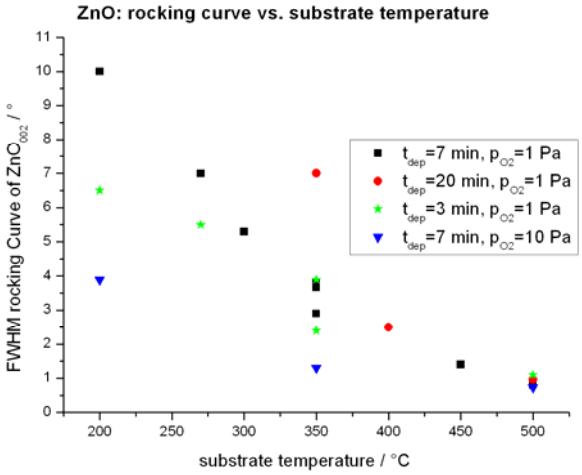

Figure 2: FWHM of rocking curves of ZnO_{002} plotted over the substrate temperature: A clear trend towards better crystallinity at higher temperatures is observed

In summary, we determined optimal deposition parameters for PLD of smooth YBCO and ZnO films with high crystallinity. Furthermore, we improved the PLD setup to drastically decrease the droplet density, making the films much more suitable for multilayer applications.

References:

[1] U. Ozgur, Y.I. Alivov, C. Liu, A.Teke, M.A. Reshchikov, S. Dogan, V. Avrutin, S. Cho, & H. Morkoc, *A comprehensive review of ZnO materials and devices*, J. App. Phys., 98, 041301 (2005)

Dielectric properties of thin $SrTiO_3$ films

V. Grosse, F. Schmidl and P. Seidel

Strontium titanate (STO) is a commonly applied material in association with high temperature superconductors (HTSC), like $YBa_2Cu_3O_{7-x}$ (YBCO). Due to its good lattice match and chemical compatibility it serves as substrate material and insulating layer in HTSC devices. In the last years recent studies on STO focus on resistive switching phenomena caused by electrochemical induced redox reactions on individual dislocations[1]. This effect and its high dielectric constant makes the material interesting for the application in semiconducting devices, like field effect transistors or electronic memory devices. In this work, we present detailed investigations on the dielectric properties of thin epitaxial STO films with thicknesses ranging from 25 to 70 nm in an YBCO-STO-Au system.

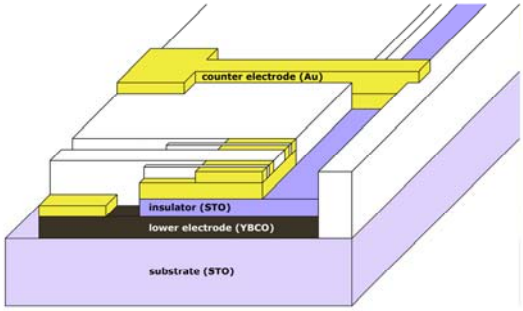

Figure 1: Sample layout for our electrical measurements.

The tri-layer system was grown *in situ* by pulsed laser deposition an STO substrates. All process parameters are included in table 1. The films showed a good c-axis orientation with a full width at half maximum of the rocking curve of $\Delta\omega<0.25°$ and $\Delta\omega<0.40°$ for YBCO (005) and STO (002), respectively. The rms-roughness of the YBCO films was approximately 11 nm, and 2 nm for the STO films. After deposition the tri-layer was patterned according to figure 1 to obtain plate capacitor like structures.

Layer	p_{O2} [Pa]	T_S [°C]	E_L [mJ]	f [Hz]
YBCO	40	750	65	5
STO	15	710	45	5

Table 1: Parameters for the deposition of the YBCO and STO film. p_{O2} is the oxygen partial pressure, T_S the substrate temperature during deposition, E_L is the laser energy at the target and f is the pulse rate of the excimer laser (λ=248 nm).

We measured the temperature dependence of the capacitance of our films using a Keithley LCZ Meter 3330 at f=5000 Hz. The results are shown in figure 2a. At temperatures below 50 K the capacitance rises distinctively and saturates below 10 K. The same behaviour we observed at thin CeO_2 films deposited on STO substrates[2]. We therefore attribute it to an additional capacitance arising from stray fields through the substrate. The dependence of the capacitance C on the contact area A and temperature T can be written as follows:

$$C(A,T) = \varepsilon_r(T)\frac{\varepsilon_0}{d}A + C_0(T). \qquad (1)$$

The additional offset capacitance C_0 is independent of the contact area and rises with lower temperatures according to the mean-field theory of Barrett[3] describing the behaviour of STO single crystals (see figure 2b), which supports our assumption.

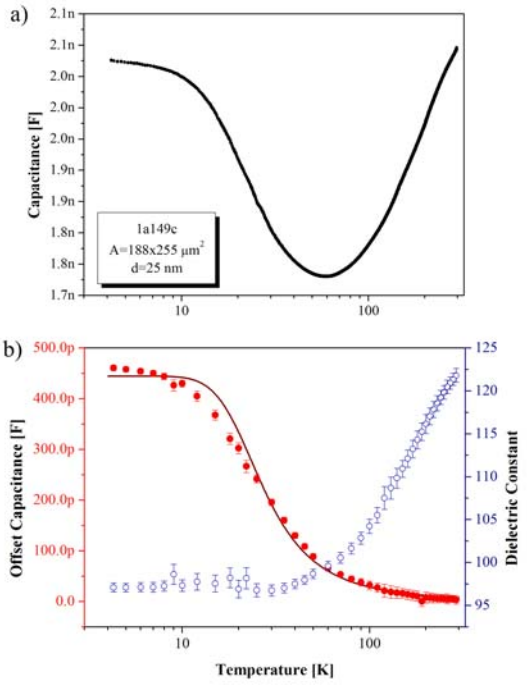

Figure 2: (a) Capacitance versus temperature plot as measured at a single contact of the 25 nm thick sample. (b) Calculated offset capacitance (dots) compared to the mean-field theory of Barrett (line, left scale) and dielectric constant of this film versus temperature (circles, right scale).

In figure 4 we plotted the temperature dependence of the dielectric constant for two of our STO films. The sample with a thickness of 70 nm shows a maximum of ε_r at T≈220 K. This maximum is related to a paraelectric to ferroelectric phase transition, which shifts to higher temperatures at lower film thicknesses. Additionally, the dielectric constant is significantly higher for the thicker sample.

We tried to model this behaviour by assuming thin layers near the electrode showing a ferroelectric phase transition, while the centre of the film remains quantum paraelectric. Additionally, we assume the

Curie temperature to rise with a lower distance to the electrode (see figure 4). It is known, that the quantum paraelectric state can be destroyed by doping or applying mechanical stress or electric fields[5,6,7]. Electronic conditions at the interface introduce electric fields and space charges. Mechanical stress is introduced because of the lattice misfit between YBCO and STO. All of these influences are likely to increase at the electrode and result in a growing Curie temperature.

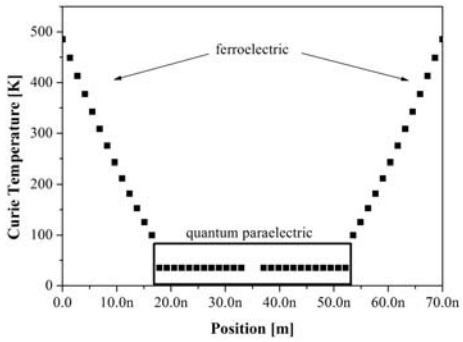

Figure 3: Distribution of the Curie temperature T_0 over the sample thickness. The inner part of the 70 nm thick film remains quantum paraelectric, while near the electrodes a paraelectric to ferroelectric phase transitions can occur.

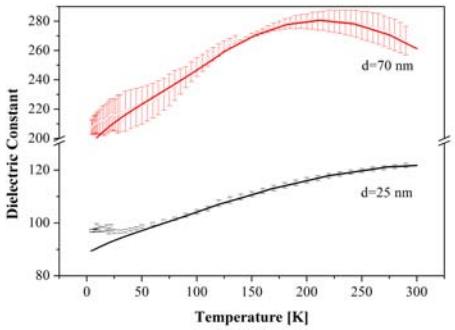

Figure 4: Dielectric constant versus temperature of two of our samples calculated from equation (1) (circles) and the respective theoretical curves according to our model (lines). We chose a medium Curie constant of $M=5.5\cdot10^4$ K (d=70 nm) and $M=4.2\cdot10^4$ K (d=25 nm) to fit our data.

The following relations were used to calculate the theoretical temperature dependence of the dielectric constant[3,4]:

$$\varepsilon_r(T) = \begin{cases} \dfrac{M}{T - T_0} & (2) \\ \dfrac{M}{2(T_0 - T)} & (3). \\ \dfrac{M}{(T_1/2)\coth(T_1/2T) - T_0} & (4) \end{cases}$$

Equation (2) describes the paraelectric state ($T>T_0$), equation (3) the ferroelectric state ($T<T_0$) and equation (4) is the Barrett formula for the quantum paraelectric state.

For temperatures above 50 K our model represents our measured data very well. But for lower temperatures the theoretical curve deviates significantly. Better fits may be obtained, if the relation proposed by Hemberger et al.[7] is used to describe the temperature and electric field dependence of the dielectric constant in the ferroelectric state. However, this relation is far more complex to evaluate.

In summary, we measured the temperature dependence of the static dielectric constant of STO. We were able to separate additional contributions to the capacitance arising from stray fields through the substrate. We successfully developed a model to describe the temperature dependence of ε_r of our films, which proposes thin layers near the electrodes showing a paraelectric to ferroelectric phase transition. In this model we allow a distribution of the Curie temperature rising towards the electrodes which explains the broad peak in the dielectric constant we measured.

References:

[1] K. Szot, W. Speier, G. Bihlmayer and R. Waser, *Switching the electrical resistance of individual dislocations in single-crystalline $SrTiO_3$*, Nat. Mater. **5**, 312-320 (2006).

[2] V. Grosse, R. Bechstein, F. Schmidl and P. Seidel, *Conductivity and dielectric properties of thin amorphous cerium dioxide films*, J. Phys. D: Appl. Phys. **40**, 1-4 (2007).

[3] J.H. Barrett, *Dielectric constant in perovskite type crystals*, Phys. Rev. **86**, 118-20 (1952).

[4] D. Fuchs, C. W. Schneider, R. Schneider and H. Rietschel, *High dielectric constant and tunability of epitaxial SrTiO3 thin film capacitors*, J. Appl. Phys **85**, 7362-9 (1999).

[5] K.C. Park and J.H. Cho, *Electric field dependence of ferroelectric phase transition in epitaxial $SrTiO_3$ films on $SrRuO_3$ and $La_{0.5}Sr_{0.5}CoO_3$*, Appl. Phys. Let. **77**, 435-37 (2000)

[6] C. Ang, Z. Yu and Z. Jing, *Impurity-induced ferroelectric relaxor behavior in quantum paraelectric $SrTiO_3$ and ferroelectric $BaTiO_3$*, Phys. Rev. B 61, 957-61 (2000).

[7] J. Hemberger, M. Nicklas, R. Viana, P. Lunkenheimer, A. Loidl and R. Böhmer, *Quantum paraelectric and induced ferroelectric states in $SrTiO_3$*, J. Phys.: Condens. Matter **8**, 4673-90 (1996).

Cryogenic Q-factor measurements on calcium fluoride

R. Nawrodt, A. Zimmer, S. Nietzsche, R. Neubert, M. Thürk, W. Vodel, P. Seidel

Interferometric gravitational wave detectors like GEO600 [1] are among the most sensitive instruments ever developed. One of the fundamental noise sources of these optical devices is thermal noise of crucial parts like the end-mirrors or the beam splitter. One approach to lower thermal noise is cooling these components down to cryogenic temperatures. Furthermore, it is possible to lower the thermal noise within the detection band of the gravitational wave detector by the use of high-Q materials. Here, most of the thermal noise energy is arranged around the mechanical resonant frequencies of the optical components. These resonances are typically in the range of a few 10 kHz and therefore far above the detection band. By shifting the thermal noise to higher frequencies the low frequency noise level is decreased and therefore the sensitivity of the detector enhanced. The thermal noise power spectrum far away from the resonances is directly linked to the mechanical Q-factor:

$$\left\langle x^2 \right\rangle \sim \frac{T}{Q(T)}. \qquad (1)$$

The mechanical Q-factor is a strongly temperature dependent parameter [2]. One of the most promising candidates as a substrate material for a cryogenic gravitational wave detector is calcium fluoride. This material has excellent optical properties and is available in large samples. The Q-factor of calcium fluoride samples with a diameter of 75 mm and a thickness of 75 mm was measured between 6 and 300 K. The samples were polished to an optical standard quality (front, back, circumference, and bevels). The test masses were suspended as a pendulum by means of a 75 µm tungsten wire. Figure 1 shows one of the samples in the special built cryostat [3].

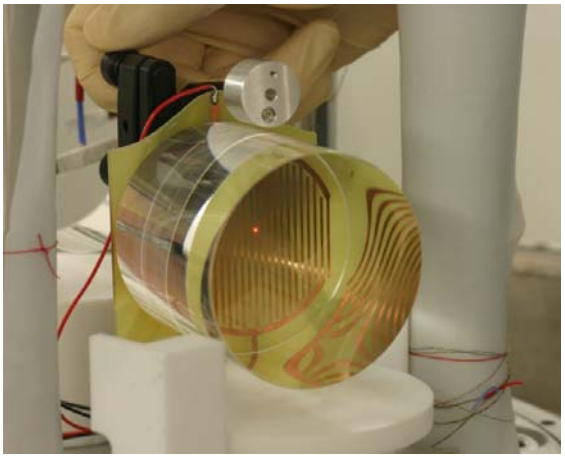

Figure 1: Calcium fluoride test sample (∅ 75 mm × 75 mm) suspended as a pendulum. In the background the electrostatic actuator for the excitation of the resonant frequencies can be seen.

The test mass was excited to resonant vibrations by the use of an electrostatic driving plate with an applied voltage up to 1600 volts. The resonant frequencies and the shapes of the different modes were calculated using the finite element analysis package ANSYS. In figure 2 two representative modes are plotted. Mode A is called a drum mode – mode B a butterfly mode. While mode A has approximately zero movement at the suspension area in the middle of the circumference mode B has a large movement in the middle of the substrate. Therefore, a strong interaction between the test mass and the suspension

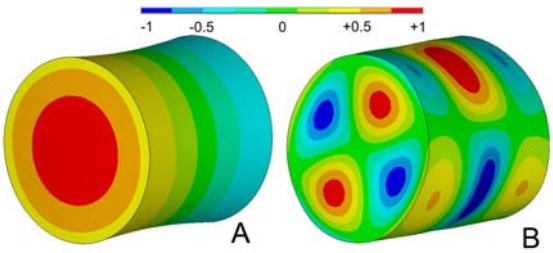

Figure 2: Calculated shapes of two modes. The substrate is suspended by means of a tungsten wire around the middle. While mode A has zero movement at the midplane, mode B has large fluctuations around the middle of the circumference.

wire - which surrounds the sample in the middle - can be expected for mode B.
The free ring-down of the different modes was observed using a Michelson interferometer with a resolution of better than 0.3 nm. Figure 3 summarizes the results for 3 different modes.

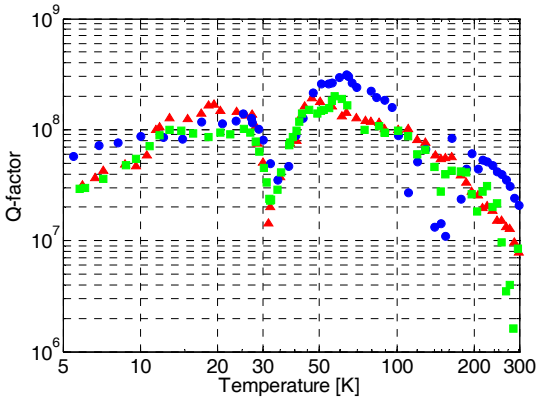

Figure 3: Compilation of the measured Q-factors for 3 different modes. Blue circles – 41302 Hz drum mode, red triangles – 40310 Hz butterfly mode, green squares – 57421 Hz butterfly mode (resonant frequencies at 300 K).

The highest Q-factor was achieved for the drum mode at 64 K with 3.2×10^8. Below this temperature the Q-factors decrease reaching 5.8×10^7 at 5.5 K. Between 25 and 50 K a resonant dip can be observed for all modes. The lowest Q-factor corresponds to a temperature which seems to be dependent on the resonant frequency. This might be an indication for relaxation processes which were already observed in crystalline quartz samples [4]. The current measurements are due to the investigation of these processes. More modes are measured to compare the temperature dependence of the resonant effects to the well known behaviour of relaxation processes. Between 75 and 200 K the measurements showed scattered data. A second test run was performed to investigate this behaviour. The temperature range was analysed with much more data points. The results are plotted in figure 4 for two modes. Two major resonances can be observed. These resonances correspond to a substrate resonant frequency of 41010.6 Hz for the first mode and 41720.5 Hz for the second mode due to the fact that the resonant frequencies of the substrate are also a strong temperature dependent value [5]. The difference of the

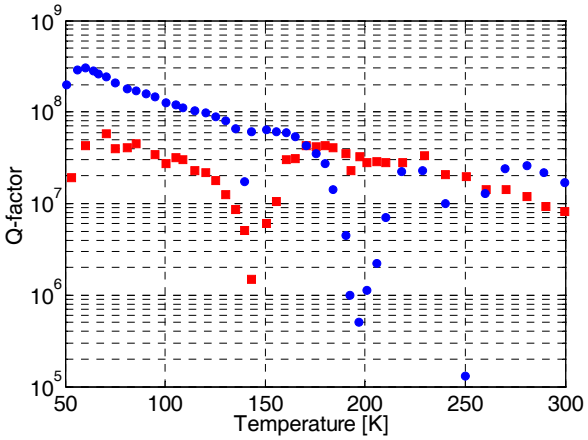

Figure 4: Detailed analyse of the temperature dependence of the Q-factor between 50 and 300 K. Two major resonant dips can be observed corresponding to resonances between the substrate mode and a violin mode of the suspension. Red squares – 40310 Hz, blue circles – 41302 Hz (resonant frequencies at 300 K).

two frequencies corresponds very well to the separation of the suspension wire resonances (so called violin modes). Therefore, this resonant effect is not an intrinsic effect of calcium fluoride but a limitation of the measuring setup. From the frequency-temperature dependence of the different substrate modes it can be concluded that at temperatures below 50 K no other resonance with the suspension can occur. This is a strong evidence that the origin of the resonant dip at around 30 K is within the substrate material (e.g. relaxation processes).

This work was supported by the DFG under contract SFB Transregio 7.

References:

[1] H. Lück et al., Class. Quantum Grav. 23 (2006) S71-S78.
[2] S. Nietzsche et al., Journal of Physics: Conf. Series 32 (2006) 445-450.
[3] R. Nawrodt, A. Zimmer, S. Nietzsche, M. Thürk, W. Vodel, P. Seidel, Cryogenics 45 (2006) 718-723.
[4] A. Zimmer et al., annual report 2006, solid-state-physics devision, Jena University.
[5] R. Nawrodt et al., accepted for publication in Eur. Phys. J. Appl. Phys.

Mechanical losses in crystalline solids at low temperatures

A. Zimmer, R. Nawrodt, R. Neubert, S. Nietzsche, M. Thürk, W. Vodel, P. Seidel

Mechanical losses and thermal noise are correlated by the fluctuation dissipation theorem [1]. Lowering thermal noise of components of high precision experiments and thus enhancing their sensitivity requires decreasing the mechanical losses in their detection frequency band. Interferometric gravitational wave detectors (IGWDs) measure between 10 Hz and 10^4 Hz. A further reduction of the thermal noise of their mirrors and beamsplitters, which act as test masses, can be achieved by lowering the operating temperature to the cryogenic range. As the mechanical loss factor is in general dependent on frequency and temperature, $\phi(f,T)$, materials offering low losses in the detection frequency band at low temperatures are desired.

The origin of mechanical losses are manifold microscopic processes. They dissipate energy by withdrawing it from a passing acoustic wave and transferring it to the thermal bath. Besides external damping as for instance due to the suspensions of the test masses or residual gas damping, internal processes are responsible for the losses. The internal losses can be further divided into dissipation processes occurring in an 'ideal' solid such as thermo-elastic damping or interactions of elastic waves with thermal phonons and additional loss processes occurring in a 'real' solid caused by defects.

These dissipation phenomena are also called relaxation processes as establishing a new equilibrium after the perturbation takes some time, therefore named relaxation time.

For small losses the mechanical loss angle caused by a single relaxation effect can be described by [2, 3]:

$$\phi \approx \Delta \frac{2\pi \cdot f \cdot \tau}{1+(2\pi \cdot f \cdot \tau)^2}, \qquad (1)$$

where Δ is the relaxation strength, f is the frequency, and τ is the relaxation time.

The measurement of these small losses in the detection frequency range of the IGWDs is a problem as the materials have been selected for mechanical losses as low as possible.

It is easier to measure the reciprocals of the small losses as they are of huge values. They are measurable at the particular resonant frequency of the test mass f_0 in the form of the mechanical quality factor Q of this mode,

$$\frac{1}{\phi(f_0)} = Q(f_0). \qquad (2)$$

For low-loss systems the Q factor is obtained by measuring the ring-down time of the amplitude of the freely vibrating sample at a resonant frequency. Details concerning the experimental setup can be found in [4].

To transfer the results obtained at the resonant frequencies to the mechanical loss factors at the frequencies of the IGWD's detection band a theoretical approach has to be developed. Combining eq. (1) and (2) a single relaxation effect causes a damping at the resonant frequency f_0 of the sample:

$$Q_{rel}^{-1}(f_0,T) = \Delta(f_0,T)\frac{2\pi \cdot f_0 \cdot \tau}{1+(2\pi \cdot f_0 \cdot \tau)^2}. \qquad (3)$$

The temperature dependence of the resonant frequency has been omitted as it changes less than 2 % between 5 K and 300 K for the up to now investigated materials crystalline quartz [5], silicon, and calcium fluoride [6] and such is a minor effect regarding the damping.

The total damping at f_0 is the sum over all relaxation losses and a background damping Q_{bg}^{-1} due to, for example, losses in the suspension of the sample:

$$Q^{-1}(f_0,T) = \sum_i Q_{rel,i}^{-1}(f_0,T) + Q_{bg}^{-1}(f_0,T). \qquad (4)$$

Therefore, by measuring the damping or rather the Q factor it should be possible to gain the relaxation parameters Δ and τ of the dominating processes.

To extrapolate the loss at the detection frequencies of the IGWDs by using equation (4) in this frequency range the dependences of the relaxation strength on temperature, frequency and on the directions of the crystal, respectively the mode shape are needed. Further, the temperature and frequency dependences of the relaxation times have to be investigated as well as that of the background losses. For the IGDWs' mirrors their special environment, e.g. mirror suspensions, has to be considered. Also the losses of the mirrors' coatings have to be included.

Many relaxation phenomena, in particular the defect related, result from a stress-induced tran-

sition of the crystal between two configurations. Their potential energy landscape consists of two valleys separated by a wall. Its height is equal to the activation energy of a jump to the other valley. The relaxation time exponentially depends upon the reciprocal temperature [3]:

$$\tau = \tau_0 \cdot e^{\frac{E_a}{k_B \cdot T}}, \qquad (5)$$

where k_B is the Boltzmann constant and E_a is the activation energy for an elementary jump process involved in the relaxation with the reciprocal jump frequency τ_0.

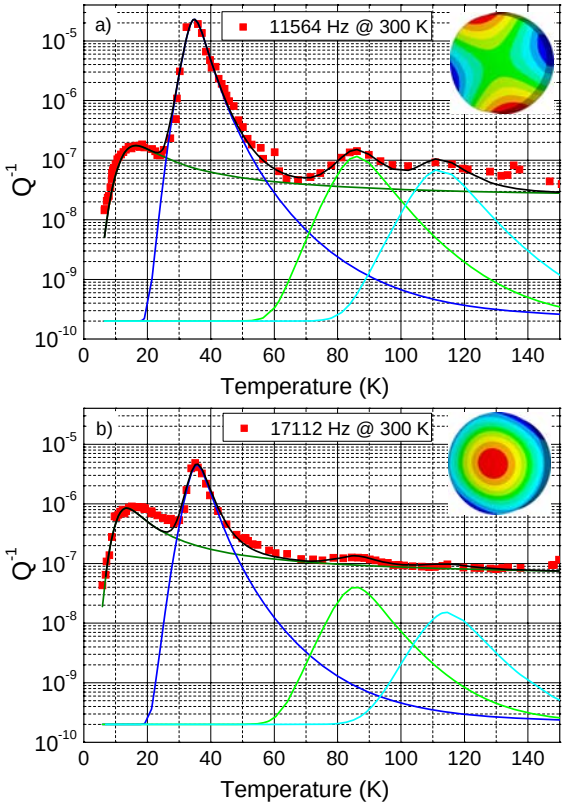

Fig. 1a+b: Damping of a crystalline quartz sample in dependence on temperature. Mode shapes are included as insets on the upper right (details in text below):
measurement,
relaxation peaks: 1, 2, 3, 4,
sum of peaks 1, 2, 3 and 4.

Relaxation parameters of the dominating processes in the low temperature range have been determined by measuring the damping curves for a z-cut crystalline quartz cylinder (74.8 mm in diameter and 12.05 mm thick) for 5 different mode shapes. For two characteristic mode shapes see fig. 1 a and b and the corresponding relaxation parameters in tab. 1. The relaxation constants differ about 6 magnitudes comparing the first relaxation effect to processes 2 to 4. This indicates at least two types of interactions.

Relax. peak	f_0 [Hz]	Δ ($\times 10^{-8}$)	τ_0 [s] ($\times 10^{-14}$)	E_a [meV]
1. (dark green)	11564 17112	35 170	80000000 30000000	4 4
2. (dark blue)	11564 17112	4600 900	30 80	53 50
3. (light green)	11564 17112	23 8	44 44	128 124.5
4. (light blue)	11564 17112	14 3	4 4	190 190

Tab. 1: Relaxation parameters of selected modes, Q_{bg}^{-1} in every case max. 2×10^{-10}.

Whereas the first relaxation peak is due to interactions of the acoustic waves with thermal phonons [7], the other damping peaks are caused by defect induced losses [8]. For simplicity reasons the relaxation strength of the first damping process was assumed to be constant over temperature. The coupling of the thermal phonons to the acoustic waves is more than 4 times stronger for the second mode ('drum') than for the other 4 modes measured. Regarding the losses induced by alkali ions (peak 2-4) this mode shows however smaller losses and the first mode ('butterfly') possesses the strongest ones. Work concerning the dependence of the relaxation processes on mode shape is in progress.

This work was supported in part by the DFG, contract SFB/TR7 (C4).

References

[1] H. B. Callen and T. A. Welton, *Irreversibility and Generalized noise*, Phys. Rev. 83 (1951) 34-40.
[2] C. Zener, *Elasticity and Anelasticity of Metals*, University of Chicago Press, Chicago, 1948.
[3] R. de Batist, *Internal Friction of Structural Defects in Crystalline Solids*, North-Holland, Amsterdam, 1972.
[4] R. Nawrodt, A. Zimmer, S. Nietzsche, M. Thürk, W. Vodel and P. Seidel, *A new apparatus for mechanical Q-factor measurements between 5 and 300 K*, Cryogenics 46 (2006) pp. 718-723.
[5] A. Zimmer, R. Nawrodt, R. Neubert, S. Nietzsche, M. Thürk, W. Vodel and P. Seidel, *Measurements of the mechanical Q-factor at low temperatures: crystalline quartz*, submitted to Phys. Rev. B.
[6] R. Nawrodt et al., Annual Report 2006, Institut für Festkörperphysik, Friedrich-Schiller-Universität Jena.
[7] T. O. Woodruff and H. Ehrenreich, *Absorption of Sound in Insulators*, Phys. Rev. 123 (1961) pp. 1553-1559.
[8] D. B. Fraser, in *Physical Acoustics: Principles and Methods Vol. V*, Academic, New York, 1968.

LOW NOISE PULSE TUBE REFRIGERATOR IN AN ENTIRE COAXIAL TWO-STAGE CONFIGURATION

T. Koettig, R. Nawrodt, S. Moldenhauer, M. Thürk, and P. Seidel

Two stage pulse tube refrigerators (PTR) in U-tube design are the standard for cooling devices at temperatures below 10 K down to 2 K. Cooling capacities in the range of 100 mW at 4.2 K are reached by several research prototypes and commercially available two-stage PTRs in U-tube design [1-7]. In the U-tube configuration, vibrations perpendicular to the axis of the coldfinger cannot be avoided because they are inherent by the design. This problem is the topic of current research [8]. The well-known coaxial configuration has the ability to avoid this disadvantage. The coaxial arrangement of the pulse tube and the regenerator combines the advantages of the pulse tube concept (non-existing moving part within the coldfinger) and the compact design of a GM-type refrigerator. Therefore, the two-stage PTR in coaxial configuration opens up the areas of GM-type application.

A new type of a two-stage PTR in an entire coaxial configuration is introduced [9]. We report on the inhomogeneous set-up of the second stage regenerator matrix, which consists of our self-made electroplated lead screen material [10]. Without using any rare earth compounds in the coldest part of the regenerator the new two-stage PTR reaches a no load temperature of 6.5 K and provides a cooling capacity of 2 W at 9.5 K. Fig.1 shows a sectional view of the three dimensional CAD-layout of the PTR.

Due to the coaxial design an additional thermal contact occurs between the two pulse tubes and the respective regenerators at intermediate temperatures. The resulting heat transfer could reduce the refrigerator efficiency seriously. To prevent losses in the cooler efficiency to a greater extent we had to match the coldfinger-components properly. We use corresponding results from various sources [11, 12].

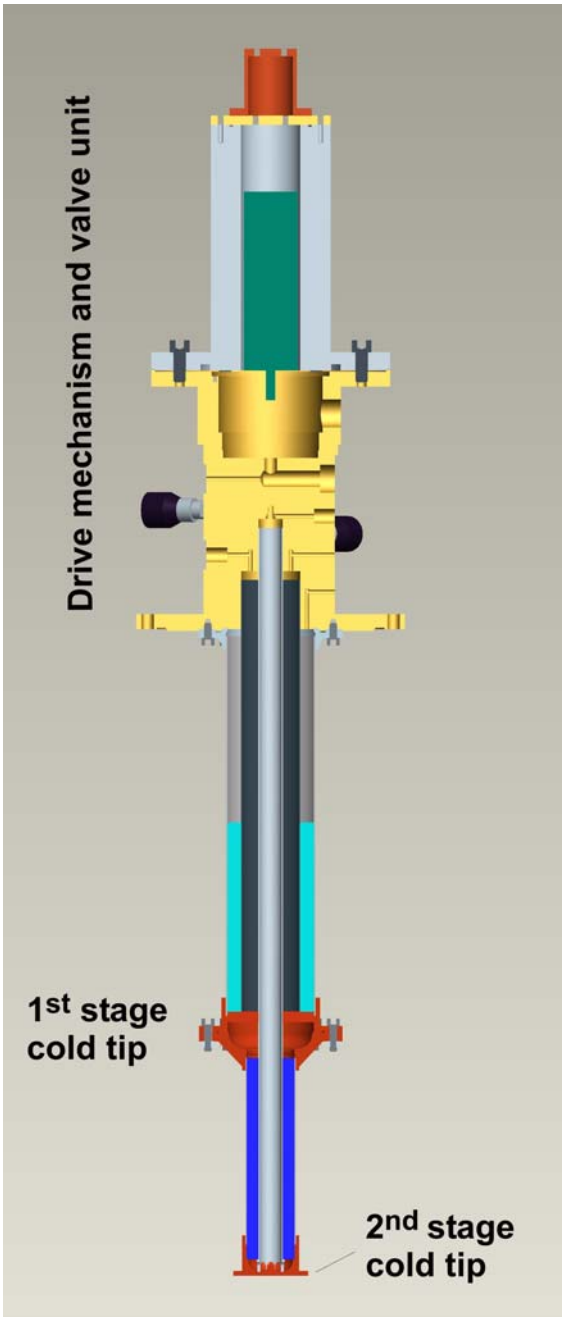

FIGURE 1 Sectional view of the new developed two stage PTR in coaxial design. The 2nd stage pulse tube is located inside the respective regenerator and additionally inside 1st stage pulse tube.

The 1st stage regenerator is filled with 1250 disks of 200 mesh stainless steel screens. The 2nd stage regenerator consists of an inhomogeneous matrix of self-made lead coated screens [13, 14].

EXPERIMENTAL RESULTS

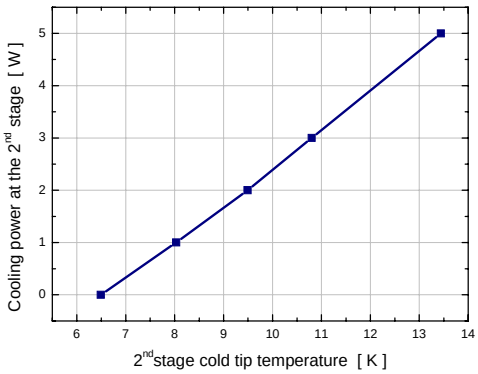

FIGURE 2 Cooling performance at the 2nd stage. No heat input at the 1st stage. Compressor unit Leybold RW 6000 6.2 kW nominal electrical input power.

Fig. 2 illustrates the cooling performance at the 2nd stage cold tip. The cold tip temperatures oscillates with an maximum amplitude smaller than ± 0.2 K. The plotted temperatures are time averaged values. The whole cryocooler performance including a heat input at the 1st stage cold tip is shown in Fig. 3.

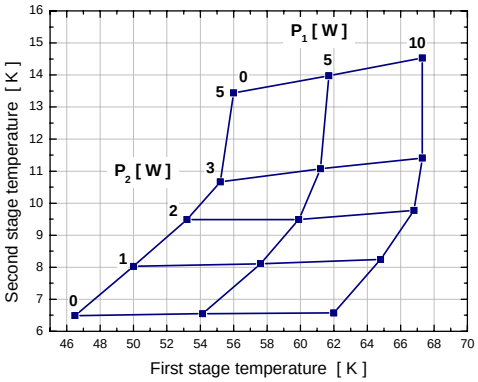

FIGURE 3 Two parametric plot of the cooling performance of the two stage PTR. The parameters are the values of heat input P_1 and P_2 at the respective stages. Compressor unit Leybold RW 6000 - 6.2 kW of input power.

CONCLUSIONS

We demonstrate a new type of a two-stage PTR, successfully. The achieved cooling performance is comparable with standard PTRs in U-tube design. By using lead coated screens in the 2nd stage regenerator a no load temperature of 6.5 K can be reached. The PTR provides a cooling capacity of 2 W at 9.6 K in an entire coaxial design. The intermediate thermal contact between the proper arranged pulse tubes and regenerators is able to stabilise the cryocooler-operation.

REFERENCES

[1] Jiang N, Lindemann U, Giebeler F, Thummes G, A 3He pulse tube cooler operating down to 1.3 K. Cryogenics 2004;44:809-816.
[2] Wang C, Thummes G, Heiden C, Experimental study of staging method for two-stage pulse tube refrigerators for liquid 4He temperatures. Cryogenics 1997;37:857-863.
[3] Wang C, Helium liquefaction with a 4 K pulse tube cryocooler. Cryogenics 2001;41:491-496.
[4] Tanaka M, Nishitani T, Kodama T, Araki T, Kawaguchi E, and Yanai M, Experimental and Analytical Study of Two Stage Pulse Tube Refrig., Adv Cryo Eng 41 B, 1995, pp. 1487-1494.
[5] Inoue T, Matsui T, Kawano S, Ohasi Y, Experimental Research on Two-Stage Pulse Tube Refrigerator, Proceedings of the ICEC 16, Japan, 1996, pp. 299-302.
[6] Hofmann A, Pan H, and Oellrich L, GM-Type Two-Stage Pulse Tube Cooler with High Efficiency, Cryocoolers, Vol. 11. Kluwer; 2001, pp. 221-227.
[7] Chen G et al., Experimental study on a double-orifice two-stage pulse tube refrigerator. Cryogenics 1997;37:271-273.
[8] Tomaru T et al., Vibration analysis of cryo-coolers. Cryogenics 2004;44 :309-317.
[9] Koettig T, Moldenhauer S, Nawrodt R, Thürk M, Seidel P, Two-stage pulse tube refrigerator in an entire coaxial configuration, Cryogenics 2006;46: 888-891.
[10] Waldauf A, Köttig T, Moldenhauer S, Thürk M, and Seidel P, Improved Cooling Power by Means of a Regenerator Made from Lead Wire Mesh, Cryocoolers, Vol. 13, Springer, 2005, pp. 389-394.
[11] de Waele ATAM, Tanaeva IA, Ju YL, Multistage pulse tubes. Cryogenics 2000;40:459-464.
[12] Koettig T, Moldenhauer S, Patze M, Thürk M, and Seidel P, Investigation on the Internal Thermal Link of Pulse Tube Refrigerators. Cryogenics; to be published.
[13] Köttig T, Waldauf A, Thürk M, and Seidel P, Developments on GM-Type Pulse Tube Cryorefrigerators with Large Cooling Power, Adv Cryo Eng 49 B, AIP Conf Proc Vol. 710, 2004, pp. 1445-1450.
[14] Koettig T, Nawrodt R, Moldenhauer S, Thürk M, Seidel P, Novel Regenerator Material Improving the Performance of a Single Stage Pulse Tube Cooler, , Adv Cryo Eng 51 A, AIP Conf Proc Vol. 823, 2006, pp. 35-40.

3. Technical reports and equipments

Operation of the Ion-accelerator JULIA and the Ion-implanter ROMEO

U. Barth, F. Jehn, G. Lenk, W. Wesch, W. Witthuhn

The 3 MV high current tandetron accelerator **JULIA** (***J***ena ***U***niversity ***L***aboratory for ***I***on ***A***cceleration) went in operation end of 1996. Since the beginning of the routine-operation in 1997 it has been used for different types of experiments requiring a broad spectrum of ion-beams. With the exception of Helium, where the duoplasmatron ion-source followed by a Lithium exchange channel was used, all ions were extracted from a sputter-type ion-source. The beam-on-target-time was about 1404 hours, in the same order as 2005. The 400 kV ion-accelerator **ROMEO** is in routine operation since 1998, here the beam-on-target-time was 979 hours, nearly identical to 2004.

Both accelerators can be operated separately or in combination. The ion-beams produced during the period 2006 are summarized in table 1. The ion-beam currents quoted are typical values of the ion source currents used for the experiments, the maximum currents available are significantly higher for most ions.

During 2006 both accelerators were operated routinely. Technical problems arose with (1) the vacuum system of the implantor and (2) the computer-controlling of the tandetron accelerator. In this context one has to realize that important parts of the accelerator facility are now running since 10 years. Here reinvestments will be necessary in the next future.

Some components of the equipment and the software were improved in 2006:

(1) The target chamber with simultaneous access for low-energy implantations (ROMEO) and hihg energy beams (JULIA) has been integrated into the computer-controlling of the accelerator facility. Hereby the status of different parameters as beam currents and vacuum values can be monitored. Additionally, the beam stop and the vacuum settings can be preselected by the computer. This improvement significantly increased the reliability of the apparatus.

Period	Element	Julia[1]	Romeo[2]
1	Hydrogen (H)	5 µA	4 µA
	Helium (He)	0,2 µA	4 µA
2	Lithium (Li)	2 µA	1 µA
	Boron (B)	0,2 µA	5 µA
	Carbon (C)	9 µA	10 µA
	Nitrogen (N)	10 µA	4 µA
	Oxygen (O)	17 µA	2 µA
3	Sodium (Na)	-	6 µA
	Magnesium (Mg)	-	5 µA
	Aluminium (Al)	-	4 µA
	Silicon (Si)	16 µA	4 µA
	Phosphorus (P)	-	4 µA
	Argon (Ar)	-	200 µA
4	Calcium (Ca)	-	5 µA
	Titanium (Ti)	0,7 µA	-
	Vanadium (V)	0,2 µA	1 µA
	Manganese (Mn)	-	5 µA
	Chromium (Cr)	0,2 µA	3 µA
	Iron (Fe)	0,8 µA	2 µA
	Cobalt (Co)	-	3 µA
	Nickel (Ni)	-	6 µA
	Zinc (Zn)	1 µA	6 µA
	Gallium (Ga)	1 µA	3 µA
	Germanium (Ge)	1,6 µA	4 µA
	Arsenic (As)	0,4 µA	10 µA
	Selenium (Se)	0,5 µA	15 µA
	Bromine (Br)	19 µA	8 µA
	Krypton (Kr)	-	10 µA
5	Rubidium (Rb)	0,075 µA	1 µA
	Zirconium (Zr)	0,3 µA	1,5 µA
	Rhodium (Rh)	0,2 µA	-
	Palladium (Pd)	0,095 µA	10 µA
	Silver (Ag)	-	10 µA
	Cadmium (Cd)	-	4 µA
	Indium (In)	5 µA	8 µA
	Tin (Sn)	-	3 µA
	Antimony (Sb)	-	4 µA
	Tellurium (Te)	-	2 µA
	Xenon (Xe)	-	10 µA
6	Praseodymium (Pr)	-	1 µA
	Samarium (Sm)	0,01 µA	1,5 µA
	Europium (Eu)	0,035 µA	2 µA
	Gadolinium (Gd)	0,03 µA	-
	Erbium (Er)	0,04µA	2µA
	Tantalum (Ta)	0,2µA	2 µA
	Tungsten (W)	0,3µA	0,01µA
	Osmium (Os)	0,05 µA	-
	Iridium (Ir)	0,3µA	6 µA
	Platinum (Pt)	0,2µA	-
	Gold (Au)	24µA	20µA
	Lead (Pb)	0,035 µA	15µA
	Bismuth (Bi)	-	3µA

Table 1. Ion-beams accelerated during 2006. The currents given are measured at the Q-Snout-Faradaycup after the low-energy mass separator (JULIA) and at the target position (ROMEO), respectively.

(2) The vacuum monitoring system of the implantor ROMEO was based on 10 year old components. Here, frequently failures resulted in stops of the experiments. Installation of a new vacuum monitoring and controlling system resulted in a higher reliability of the implantor.

(3) The main computer of the tandetron accelerator JULIA failed twice in 2006. Since the replacement of the rather old components is not anymore possible, modern hard-ware components were modified and could restore the functionality of the computer-controlling.

As in the preceding years the ion-beam facility was used by external research groups:

3MV-Tandetron "JULIA"
University Jena
University Minsk, Belarus
University Stuttgart
IPHT Jena
University of Pretoria, South-Africa

400kV Implanter „ROMEO"
CiS Institut für Mikrosensorik, Erfurt
Forschungszentrum Rossendorf, Dresden
iba e.V., Heiligenstadt
IPHT Jena
University Jena
University Aveiro, Portugal
University of Minsk, Belarus
University of Pretoria, South-Africa

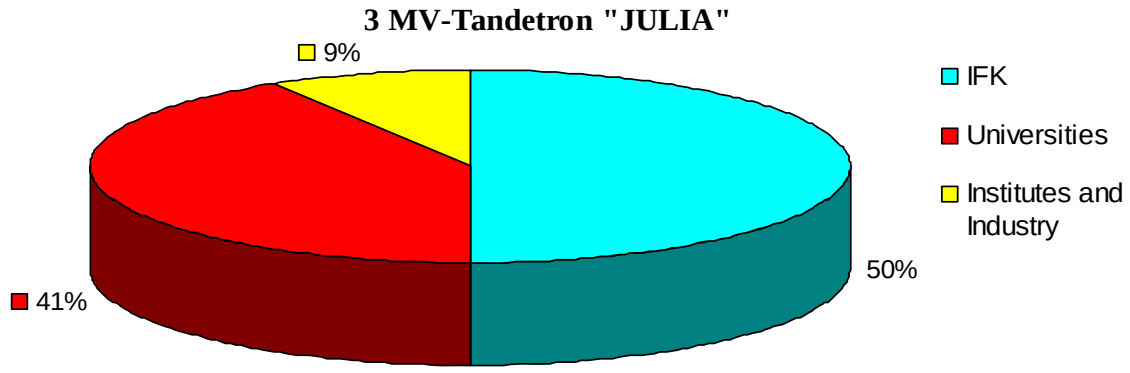

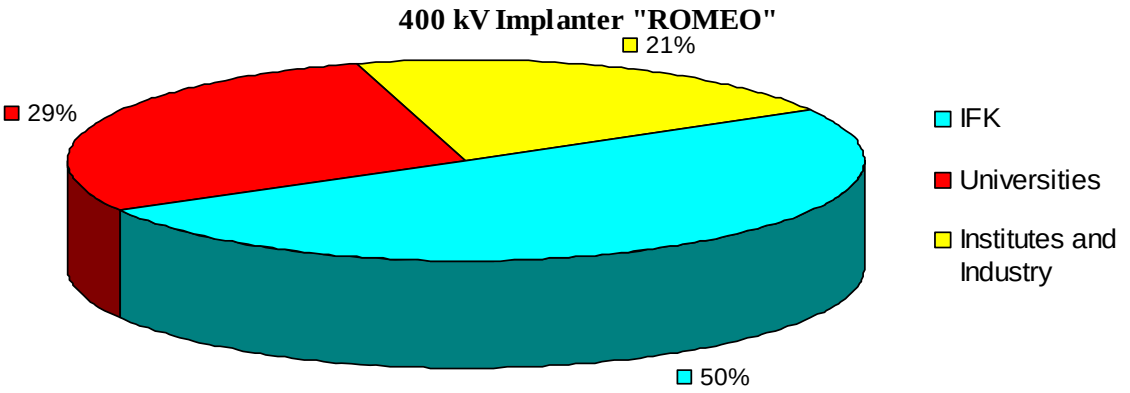

Cryogenic Services 2006

All in-house customers of cryogenic liquids like all faculties of natural sciences, the medical division of the university, including several hospitals, and other external scientific institutes (e.g. Institute for Physical High Technology Jena, , Leibnitz Institute Hans-Knöll Jena) as well as some private customers like the Innovent e.V. Jena or some medical practices were provided with liquid Helium (LHe), high purity gases (He, N_2) and with liquid nitrogen (LN_2) by the Cryogenic Services. More than 123 000 litres of LN2 were delivered by the cryogenic services this year.

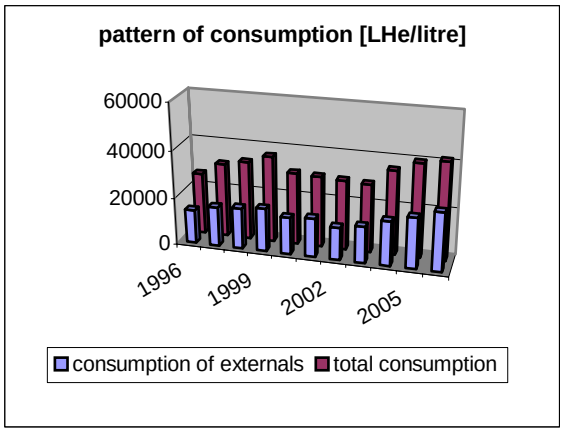

Fig 1.: Consumption of liquid helium

As illustrated in Figure 1, the production of LHe has increased in 2006, which is due to the increasingly modern and high technology equipment for scientific research as well as for the upgrading medical care in the high-technology region within and in the periphery of the city Jena.
More than **41 000** litres of LHe were produced which is the highest value ever reached with the installed liquefier LINDE LR-20 equipment. The considerable increase corresponds to an annual growth rate of more than 4%. Merely 29% of the whole output is used by the Physic faculty themselves this year. The liquefaction capacity of the facility has been increased since the beginning of the operation of the equipment starting from the design point of 10 litres/h up to 16 litres/h these days by our staff. But for all that we have to observe the fact that we have to cut down some experiments due to the limited liquefaction capacity of our equipment first time in the year 2006.

Fig. 2: Bottling of cryogenic fluid

The further increase of the LHe-production was prevented by various break downs of the main liquefaction unit which is mainly due to the uninterrupted operation time of 15 years and the permanent operation of the equipment well above the design point. During this critical shut-down periods all LHe-demanding activities had to be strictly limited to protect the scientific equipment against destruction in consequence of self-heating.

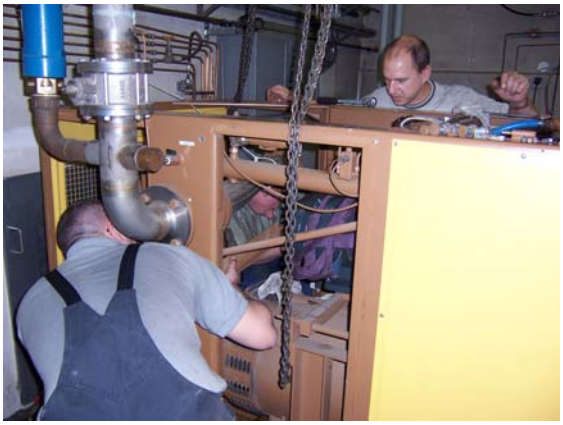

Fig. 3: The main He-compressor under repair

We would like to acknowledge the helpful financial backing of all users which sponsored the inevitable final repairs of the wrecked main compressor which was amounting to a value of 23 thousand €.

Equipment

Preparation of thin films and devices

- HV evaporation facilities for thermal evaporation and rf-sputtering with oxidation system
- UHV evaporation facilities, including electron gun and in situ RHEED system
- Equipment for laser deposition of thin films and material systems, especially high temperature superconductors (KrF excimer laser, $\lambda = 248$ nm)
- Molecular Beam Epitaxy (MBE) facilities:
- MBE for silicon carbide (RIBER EVA 32 R&D)
- MBE for III-V-semiconductors (RIBER EPINEAT III-V S)
- dc and ac sputtering systems for thin films and multilayers
- Ion beam etching with Ar ions at sample temperatures down to 80 K
- Reactive ion beam etching with sample diameters up to 6 cm
- Ultrasonic wire bonder
- Equipment for photolithographic patterning

Surface analysis systems

- AUGER electron spectrometer
- Surface analysis system UNISPEC with XPS, UPS, AES, LEED, STM
- Atomic force microscopes (AFM and Microstructure Measuring Device VERITEKT 3 with needle sensor)
- Surface profilometer DEKTAK 100
- Scanning electron microscopes

Electrical and optical measurement techniques

- Electrical transport measurements (resistance, critical current density, point contact and tunneling spectroscopy)
- Hall-effect and Four-point probe equipment
- Current-voltage characteristics ($2\ K < T < 300\ K$, $B \leq 5\ T$)
- Current-voltage characteristics by microwave irradiation ($2\ GHz < f < 300\ GHz$)
- Noise measurements (frequency range 60 μHz - 100 kHz) at low temperatures
- LTS-SQUID characterization at 4.2 K (current-voltage, flux-voltage, noise, screening properties)
- HTS-SQUID characterization up to 100 K (current-voltage, flux-voltage, noise)
- 2 Deep level transient fourier spectrometers (temperature range 80 K - 675 K, 19 K - 330 K)
- 2 Admittance spectrometers (frequency range 40 Hz - 100 kHz and 75 kHz - 30 MHz, temperature range 19 K - 675 K)
- Optical microscopes
- Optical spectrometers, wavelength region 200 nm to 40 μm
- Low temperature photoluminescence spectroscopy
- Microwave signal generator (frequency range 1 - 20 GHz, resolution: 1 kHz)
- Electrical and optical characterization of high power diode laser arrays

Equipment for thermal treatment

- Furnace for conventional thermal treatment in inert gas atmosphere or vacuum
- (temperatures up to 2050 K)
- RTA apparatus (double graphite strip heater) for short time annealing
- (annealing time in the order of seconds, temperature range 1000 K to 1950 K, temperature rise rate 100 K s^{-1})

Ion beam techniques

3 MV Tandetron accelerator "JULIA", equipped with

- Sputter ion source and Duoplasmatron source
- Universal beam line for ion implantation and ion beam analysis
- Second beam line for ion beam analysis, combined with implantation chamber of 400 kV implanter
- Irradiation chamber with cooled and heated sample holder and four axis goniometer

Application:

- Ion implantation: energy range 500 keV - 12 MeV, temperature range 15 K - 1500 K
- Ion beam analysis: RBS and PIXE in combination with channeling, ERDA, NRA

400 kV implanter "ROMEO", equipped with

- Hot filament, hollow cathode ion source
- Irradiation chamber with cooled and heated sample holder and four axis goniometer, combined with beam line of 3 MV Tandetron accelerator

Application:

- Ion implantation: energy range 20 keV - 400 keV, temperature range 15 K - 1500 K
- Ion implantation at low temperatures and subsequent RBS analysis using H- or He-ions from 3 MV Tandetron accelerator

Focused ion beam equipment IMSA 100 for ion implantation and sputtering

- Liquid metal ion sources delivering different ion species
- Acceleration voltage up to 60 kV resulting in 120 keV energy for doubly charged ions
- High-speed beam scanning and blanking system for patterning
- Laserinterferometric stage for sample movement: sample size 100 mm × 100 mm, lateral resolution of 2.5 nm
- Secondary - electron imaging
- Typical beam diameter 200 nm at a beam current of 100 pA

Low Energy implanter "LEILA", equipped with

- Colutron Ion source 100-Q
- Colutron Ion Gun System G-2-D
- Irradiation chamber with heated sample holder

Application:

- Implantation of Hydrogen: energy range sub-keV, temperature range 300 K - 750 K

Nuclear probe technique

- 4 Perturbed angular correlation spectrometers (NaI(Tl) and BaF_2 szintillation detectors, temperature range 4 K - 1200 K)
- HP Ge-spectrometers

Low temperature measuring equipment

- He-4 cryostats for temperatures down to 4.2 K
- He-4 refrigerator for the temperature range 1.3 K - 4.2 K
- He-3 cryostat for temperatures down to 300 mK
- He-3/He-4 dilution refrigerator with a base temperature of 35 mK
- He-3/He-4 dilution refrigerator with a base temperature of 7 mK
- Electronic equipment for characterization of cryoelectronic devices
- SQUID sensor systems for magnetic measurements under unshielded conditions
- SQUID sensor system for spatially resolved magnetorelaxometry
- Cryostats (2 K < T < 300 K; optical window; magnetic field)
- Cryocoolers (Gifford-McMahon and Stirling)
- Pulse tube refrigerators (for sensor cooling)

CIS-LAB

- MBE system GOBELIN for CIS-Layers with LEED, AES, PAC equipment
- MBE system NEBULA for CIS-Layers on 4" substrates including RHEED set up
- Two HV systems for closed-space sublimation (CSS)
- Solar simulator (AM 1.5) with Current-Voltage measurement
- RF reactive sputtering system for transparent conductive oxides (TCO's)

SQUID application laboratories

- Measurement system for non-destructive evaluation in unshielded environment based on high-T_C-SQUID gradiometers
- Heart monitoring system for biomagnetic investigation in unshielded environment based on high-T_C-SQUID gradiometers
- High precision position detection system based on low-T_C-SQUIDs
- Magnet-Relaxation-Measuring System in unshielded environment based on low-T_C SQUID gradiometers

Clean room (number of particles/cu/t < 100)

- Foto lithography
- Wet chemical etching
- minimum lateral resolution: few micrometers

Shielded rooms

- Faraday room
- Magnetic shielded room

Radionuclide laboratory

- for handling of radioactive substances

Laboratory for cryogenic measurement of mechanical quality factors of gravitational wave detector components

- room temperature stability of ± 0.2 K at best
- vibration isolation (decoupled foundation)
- acoustic isolation
- remote controlled operation of the measurement equipment
- separated room for disturbing machines (e.g. pumps)
- full supply of technical media to perform cryogenic measurements

4. Current research projects

(A) Supported by the Bundesministerium für Bildung, Wissenschaft, Forschung und Technologie (BMBF), Bundesministerium für Wirtschaft und Arbeit (BMWi), and Bundesministerium für Umwelt, Naturschutz und Reaktorsicherheit (BMU)

Characterization of irradiated GaN and ZnO
Prof. Dr. W. Wesch, Prof. M. Hayes 39.6.L1A.6.B 01/04 - 12/06

ISOLDE: Aufbau einer neuen Instrumentierung zur elektrischen Charakterisierung von Störstellen in Halbleitern
Prof. Dr. W. Witthuhn 05KK4SJ1/4 07/04 – 05/07

(B) Supported by the Deutsche Forschungsgemeinschaft (DFG)

Non-equilibrium phase transitions in crystalline semiconductors under swift heavy ion irradiation
Prof. Dr. W. Wesch WE 1707/8-1 01/05 - 12/06

Vertical, strained 1D silicon nanostructures and devices
Dr. E. Wendler WE 1648/6-1 04/05 - 06/08

Investigation of fast processes in condensed matter by time resolved X-ray diffraction
Prof. Dr. P. Seidel, Dr. I. Uschmann (IOQ) DFG US 17/3-1 10/02 - 04/07

Gütemessungen bei kryogenen Temperaturen
(Teilprojekt C 4 im SFB/TR 7 „Gravitationswellenastronomie“)
Prof. Dr. P. Seidel, Dr. W. Vodel DFG – SFB/TR7 01/03-12/10

Atomare Elektronik in intrinsischen Josephsonkontakten in strukturierten Hochtemperatursupraleitern
Prof. Dr. P. Seidel DFG Se 664/10-3 02/04 - 01/05

Strukturbildung und Lokalisierung in nichtinstantanen Medien
Prof. W. Richter RI 650/11-2 04/04 – 06/07

Spektroskopie von astrophysikalisch relevanten Molekülen in der Gasphase und in ultrakalten Helium-Tröpfchen
Prof. Dr. Fr. Huisken HU 474/13-4 07/03 – 02/07

Gas phase studies of astrophysically relevant biomolecules
Prof. Dr. Fr. Huisken HU 474/18-1 07/03 – 12/07

Silizium-Nanokristallite in Matrizen und ihre Beziehung zur Extended Red Emission
Prof. Dr. Fr. Huisken, Prof. Dr. W. Witthuhn HU-474/16-2 07/03 – 01/07

(C) Support by the EU

SCENET 2 - Superconducting European Network of Excellence (Node Uni Jena)
Prof. Dr. P. Seidel EU 04/02 - 07/06

TARGET Top Amplifier Research Groups in a European Team
Prof. Dr. W. Richter IST-1-507893-NOE 01/04 - 12/07

Biological diagnostic tools using microsystems and supersensitive magnetic detection (BIODIAGNOSTICS)
Prof. Dr. P. Seidel, Prof. Dr. J. Haueisen EU (6. Rahmenprogramm) 11/05 - 10/08

(D) Supported by the Thüringer Kultusministerium (TKM)

Ionenstrahlmodifikation und -analyse von Titanoberflächen
Prof. Dr. W. Wesch 02/9125 IBA Heiligenstadt 05/02 - 12/06

Dünnschicht Solarzellen der dritten Generation: transparente Dünnschicht Solarzellen/Tandem-Solarzellen
Prof. Dr. W. Witthuhn B 515-06012 10/06 – 09/08

(E) Supported by other institutions

Entwicklung, Aufbau und Erprobung eines schnellen DC-SQUID-Systems zur Messung von Dunkelströmen in supraleitenden Kavitäten für das TESLA-Projekt
Dr. W. Vodel DESY Hamburg 01/01 - 12/07

Untersuchungen zur plastischen Deformation von Halbleiter-Oberflächen durch hohen elektronischen Energieeintrag
Prof. Dr. W. Wesch HMI Berlin 09/02 - 02/06

Ionenstrahlinduzierte Synthese magnetischer Halbleiter für Spintronik-Anwendungen
Prof. Dr. W. Wesch DAAD D/04/42036 01/05 - 12/06

Herstellung, Charakterisierung und Anwendung unterschiedlicher Typen von Magnetfeldsensoren
PD Dr. F. Schmidl IMG Nordhausen 04/04-12/06

Experimente zur Labor-Astrophysik
Prof. Dr. Fr. Huisken MPI Heidelberg 01/02 – 05/12

CdTe-CdS-Dünnschichtsolarzellen
Prof. Dr. W. Witthuhn ANTEC Solar 09/06 – 08/07

Defekte in Solarsilizium (Defis)
Prof. Dr. W. Witthuhn CiS Institut für Mikrosensorik 09/06 – 12/07

STEP-Mission, F & E- Vorhaben mit dem ZARM Bremen
Dr. W. Vodel ZARM Bremen 07/05 -12/06

Charakterisierung von magnetischen funktionellen Nanopartikeln
PD Dr. F. Schmidl Innovent e.V. 06/06 - 12/06

The experimental, analytical and numerical investigation of the current – voltage characteristics of intrinsic Josephson junctions under microwave radiation
Prof. Dr. P. Seidel, Dr. Yu. M. Shukrinov Heisenberg-Landau Programm 01/05-12/06

5. Publications

5.1 Publications in scientific journals

Th. Höche, F. Schrempel, M. Grodzicki, P.A. van Aken, F. Heyroth
Experimental Assessment of Structural Differences between Amorphous and Amorphized Matter
Chem. Mater. 18 (22) (2006) 5351.

C.S. Schnohr, E. Wendler, K. Gärtner, K. Ellmer, W. Wesch
Ion-beam induced effects in alpha-Al_2O_3 at 15 K
Nucl. Instr. and Methods B 250 (2006) 85.

F. Schrempel, Th. Gischkat, H. Hartung, E.-B. Kley, W. Wesch
Ion beam enhanced etching of $LiNbO_3$
Nucl. Instr. and Methods B 250 (2006) 164.

F. Schrempel, Th. Gischkat, H. Hartung, E.-B. Kley, W. Wesch
High aspect ratio microstructures in $LiNbO_3$ produced by ion beam enhanced etching
Mater. Res. Soc. Symp. Proc. Vol. 908E (2006) 0908-OO16-01.1

F. Schrempel, G. Hildebrand, M. Frant, W. Wesch, K. Liefeith
Chemical behavior and corrosion resistance of medical grade titanium after surface modification by means of ion implantation techniques
Mater. Res. Soc. Symp. Proc. Vol. 908E (2006) 0908-OO14-22.1

F. Garrido, L. Nowicki, A. Stonert, A. Pietraszko, E. Wendler
^{4}He channelling studies of U_4O_9
Nucl. Instr. and Methods B 249 (2006) 497.

C.S. Schnohr, E. Wendler, K. Gärtner, W. Wesch, K. Ellmer
Ion-beam induced effects at 15 K in alpha-Al_2O_3 of different orientations
J. Appl. Phys. 99 (12) (2006) 123511.

Th. Stelzner, G. Andrä, E. Wendler, W. Wesch, R. Scholz, U. Gösele, S. Christiansen
Growth of silicon nanowires by chemical vapour deposition on gold implanted silicon substrates
Nanotechnology 17 (12) (2006) 2895.

N.A. Sobolev, M.A. Olivera, V.S. Amaral, A. Neves, M.C. Carmo, W. Wesch, O. Picht, E. Wendler, U. Kaiser, J. Heinrich
Ferromagnetism and ferromagnetic resonance in Mn implanted Si and GaAs
Materials Science Forum 514-516 (2006) 280.

A. Kamarou, W. Wesch, E. Wendler, A. Undisz, M. Rettenmayr
Swift heavy ion irradiation of InP: Thermal spike modeling of track formation
Phys. Rev. B 73 (18) (2006) 184107.

A. Hedler, S. Klaumünzer, W. Wesch
Swift heavy ion irradiation of amorphous silicon
Nucl. Instr. and Methods B 242 (1-2) (2006) 85.

M.C. Ridgway, G. de M. Azevedo, R.G. Elliman, W. Wesch, C.J. Glover, R. Miller, D.J. Llewellyn, G.J. Foran, J.L. Hansen, A. Nylandsted Larsen
Preferential amorphisation of Ge nanocrystals in a silica matrix
Nucl. Instr. and Methods B 242 (1-2) (2006) 121.

W. Wesch, A. Kamarou, E. Wendler, S. Klaumünzer
593 MeV Au irradiation of InP, GaP, GaAs and AlAs
Nucl. Instr. and Methods B 242 (1-2) (2006) 363.

W. Wesch, E. Wendler, Z.S. Hussain, S.M. Kluth, M.C. Ridgway
Rapid amorphization in $In_xGa_{1-x}As$ alloys at temperatures between 15 K and 300 K
Nucl. Instr. and Methods B 242 (1-2) (2006) 480.

R. Lauck, E. Wendler, W. Wesch
High-energy Au implantation of GaAs at 16 K
Nucl. Instr. and Methods B 242 (1-2) (2006) 484.

E. Wendler, W. Wesch
Ar implantation of InSb and AlN at 15 K
Nucl. Instr. and Methods B 242 (1-2) (2006) 562.

F.D. Auret, J.M. Nel, M. Hayes, L. Wu, W. Wesch, E. Wendler
Electrical characterization of growth-induced defects in bulk-grown ZnO
Superlattices and Microstructures 39 (1-4) (2006) 17.

N.A. Sobolev, M.A. Olivera, V.S. Amaral, A. Neves, M.C. Carmo, W. Wesch, O. Picht, E. Wendler, U. Kaiser, J. Heinrich
Ferromagnetism and ferromagnetic resonance in Mn and As co-implanted Si and GaAs
Materials Science and Engineering B 126 (2-3) (2006) 148.

K. Gärtner
MD simulation of ion implantation damage in AlGaAs: I. Displacement energies
Nucl. Instr. and Methods B 252 (2006) 190-196

S. Christiansen, R. Schneider, R. Scholz, U. Goesele, Th. Stelzner, G. Andrae, E. Wendler, W. Wesch
Vapor-liquid-solid growth of silicon nanowires by chemical vapor deposition on implanted templates
J. Appl. Phys. 100, (2006) 084323

A. Staicu, S. Krasnokutski, G. Rouillé, Th. Henning, and F. Huisken
Electronic spectroscopy of polycyclic aromatic hydrocarbons (PAHs) at low temperature in the gas phase and in helium droplets
J. Molec. Struct. 786**,** 105-111 (2006)

M.E. Gueunier-Farret, J.P. Kleider, F. Voigt, R. Brüggemann, G.H. Bauer, F. Huisken, and G. Ledoux
Transport properties and defects in silicon nanoparticles and effect of embedding in amorphous silicon layers
J. Non-Cryst. Solids, 352, 1101-1104 (2006)

C. Delerue, G. Allan, C. Reynaud, O. Guillois, G. Ledoux, and F. Huisken
On the origin of the multi-exponential photoluminescence decay of indirect gap semiconductor nanocrystals
Phys. Rev. B, 73, 235318-1-4 (2006)

C. Jaeger, H. Mutschke, F. Huisken, S. Krasnokutski, A. Staicu, Th. Henning, W. Poppitz, and I. Voicu
Identification and spectral properties of PAHs in carbonaceous soot produced by laser pyrolysis
Astrophys. J. Suppl. 166, 557-566 (2006)

C. Jäger, H. Mutschke, F. Huisken, R. Alexandrescu, I. Morjan, F. Dumitrache, R. Barjega, I. Soare, B. David, and O. Schneeweiss
Iron-carbon nanoparticles prepared by CO_2 laser pyrolysis of toluene and iron pentacarbonyl
Appl. Phys. A 85, 53-62 (2006)

Th. Hahn, J. Cieslak, H. Metzner, J. Eberhardt, U. Reislöhner, M. Gossla, J. Kräußlich, and W. Witthuhn
Metastability of $CuInS_2$ and its implications on thin-film growth
Applied Physics Letters 88 (2006) 171915

M. Preuss, F. Bechstedt, W.G. Schmidt, J. Sochos, B. Schröter, W. Richter
„Clean and pyrrole-functionalized Si- and C-terminated SiC surfaces: First-principles calculations of geometry and energetics compared with LEED and XPS"
Phys.Rev B **74**, 235406 (2006)

P. Seidel, F. Schmidl, C. Becker, U. Springborn, S. Biering, V. Grosse, T. Förster, P. Lorenz, R. Bechstein
Planar high-temperature superconducting dc-SQUID gradiometers for different applications
Supercond. Sci. Technol. 19 (2006) 5133-5148

A. Gryb, M. Mans, J. Scherbel, M. Büenfeld, F. Schmidl, P. Seidel
Synchronization of serial intrinsic Josephson junction arrays on vicinal substrates
Supercond. Sci. Technol. 19 (2006) 200–204

P. Seidel
ISEC 2005 – Conference summary and comments on SQUIDs and coolers
Supercond. Sci. Technol. 19 (2006) 179-181

S. Nietzsche, R. Nawrodt, A. Zimmer, R. Schnabel, W. Vodel, P. Seidel
Cryogenic Q-factor measurement of optivcal substrates for optimization of gravitational wave detectors
Supercond. Sci. Technol. 19 (2006) 293-296

S. Nietzsche, R. Nawrodt, A. Zimmer, W. Vodel, P. Seidel
Cryogenic Q-factor measurement of optical substrate materials
Journal of Physics: Conference Series 32 (2006) 445–450

T. Koettig, S. Moldenhauer, R. Nawrodt, M. Thürk, P. Seidel
Two-stage pulse tube refrigerator in an entire coaxial configuration
Cryogenics 46 (2006) 888–891

T. Koettig, S. Moldenhauer, M. Thürk, P. Seidel
Pulse tube refrigerator cryostat with an intrinsic top-loading system
Journal of Physics: Conference Series 43 (2006) 1421-1423

R. Nawrodt, A. Zimmer, S. Nietzsche, M. Thürk, W. Vodel, P. Seidel
A new apparatus for mechanical Q-factor measurements between 5 and 300K
Cryogenics 46 (2006) 718-723

Yu. M. Shukrinov, F. Mahfouzi, P. Seidel
Equidistance of branch structure in capacitively coupled Josephson junctions model with diffusion current
Physica C 449 (2006) 62–66

A. V. I. Shnyrkov,Th. Wagner, D. Born, S. N. Shevchenko, W. Krech, A. N. Omelyanchouk, E. Il'ichev, H. -G. Meyer
Multiphoton transitions between energy levels in a phase-biased Cooper-pair box
Phys. Rev. B 73 (2006) 024506

M. Mans, H. Schneidewind, M. Büenfeld , F. Schmidl , P. Seidel
Intrinsic Josephson junctions in misaligned $Tl_2Ba_2CaCu_2O_{8-x}$ thin films with different tilt angles
Phys. Rev. B 74 (2006) 214514

5.2 Conference contributions

NASA Laboratory Astrophysics Workshop, Las Vegas, USA, February 14 – 16, 2006

F. Huisken
Spectroscopic studies of PAHs in supersonic jets and liquid helium droplets

ILIAS meeting at the Laboratori Nazionale del Gran Sasso, Italy, February 27 – March 03, 2006

R. Nawrodt, A. Zimmer, S. Nietzsche, W. Vodel, P. Seidel
Cryogenic Q-factor measurements on Silicon

2nd Topical workshop of SCENET-2, and 11th CHEM-HTSC Workshop, Majorca, Spain, March 16 – 18, 2006

P. Seidel
Thin film technologies for HTS Josephson devices (invited)

GEO600 spring meeting, Hannover, March 20 – 21, 2006

R. Nawrodt, A. Zimmer, S. Nietzsche, W. Vodel, P. Seidel
Cryogenic Q-factor measurements

Frühjahrstagung der DPG, Dresden, March 27 – 31, 2006

A. Kamarou, W. Wesch, E. Wendler
Swift heavy ion irradiation of InP: Thermal spike analysis of ion track formation

W. Wesch, C.S. Schnohr, E. Wendler, K. Gärtner, K. Ellmer
Ion-beam induced effects at 15 K in α-Al_2O_3 of different orientation

T. Gischkat, F. Schrempel, H. Hartung, E.-B. Kley, W. Wesch
Ion beam enhanced etching of $LiNbO_3$

F. Schrempel, G. Hildebrand, M. Frant, K. Liefeith, W. Wesch
Chemical behaviour and corrosion resistance of medical grade titanium after surface modification by means of ion implantation

A. Zimmer, R. Nawrodt, S. Nietzsche, R. Neubert, M. Thürk, W. Vodel, P. Seidel
Low mechanical loss materials at cryogenic temperatures for interferometric gravitational wave detectors

T. Förster, H. Schneidewind, Ch. Becker, V. Große, R. Bechstein, F. Schmidl, P. Seidel
Characterization and Noise-Measurements on HTSC-Flip-Chip-Gradiometers with Different Antennas (Poster)

R. Nawrodt, A. Zimmer, S. Nietzsche, W. Vodel, T. Clausnitzer, E.-B. Kley, A. Tünnermann, P. Seidel
Internal Dissipation of Silicon at Cryogenic Temperatures (Poster)

C.Patzig, I.Uschmann, F.Schmidl, O. Wehrhan, M.Grube, P.Seidel
Abscheidung axial texturierter Wismutschichten auf amorphen Substraten

V. Grosse, R. Bechstein, R. Pietzker, F. Schmidl, I. Uschmann, P. Seidel
Fabrication and characterization of the electrical and dielectrical properties of insulating thin films for the application in superconducting devices (Poster)

European Workshop NanoLum IV, Tübingen, May 15 – 16, 2006

F. Huisken
Dynamical effects in semiconductor nanoparticles

Scientific and Clinical Applications of Magnetic Carriers, Krems, Österreich, May 16 – 21, 2006

F. Schmidl, P. Weber, T. Köttig, M. Büttner, S. Prass, J. Heinrich, M. Röder, K. Wagner, D.V.Berkov, P. Görnert, G. Glöckl, W. Weitschies, P. Seidel
Characterization of nanoparticle distribution of ferrofluids by magnetic relaxation measurements (Poster)

365th Heraeus Seminar, Callenges of Applied Cryoelectrics, Weilburg, Germany, May 22, 2006

T. Köttig, M. Thürk, P. Seidel
Two-Stage Pulse Tube Refrigerator in an Entire Coaxial Configuration

G.Glöckel, S.Prass, R.Hergt, S.Nagel, P.Weber, F.Schmidl, P.Seidel, W.Weitschies
Magnetic nanoparticles for hyperthermia: Determination and characterization of heating efficiency

International Workshop on *Carbon in Space*, Villa Vigoni, Loveno di Menaggio, Como, Italy, May 22 – 25, 2006

F. Huisken
Spectroscopic Studies of PAHs in supersonic Jets and Liquid Helium Droplets

C. Jaeger
Production and Properties of seed-like carbon particles

E-MRS 2006 Nizza, May 29 - June 02, 2006

J. Eberhardt
Epitaxial and polycrystalline $CuInS_2$ thin films: A comparison of opto-electronical properties

U. Reislöhner, M. Hädrich, N. Lorenz, H. Metzner, W. Witthuhn
Doping profiles in CdTe/CdS thin films solar cells

14th International Cryocooler Conference, Annapolis, USA, June 11 – 18, 2006

T. Köttig, R. Nawrodt, M. Thürk, P. Seidel
Two-Stage Pulse Tube Refrigerator in an Entire Coaxial Configuration

European Particle Accelerator Conference '06, Edinburgh, Scotland, June 26 – 30, 2006

W. Vodel, R. Neubert, S. Nietzsche, K. Knaack, K. Wittenburg, A. Peters
A new SQUID based measurement tool for characterization of superconducting rf cavities

8th International Conference on Superconductivity and High Temperature Superconductors (M2S-HTSC), Dresden, Germany, July 09 – 14, 2006

P. Seidel, C. Becker, A. Steppke, T. Förster, S. Wunderlich, V. Grosse, R. Pietzcker, F. Schmidl
Noise properties of high-temperature superconducting dc-SQUID gradiometers (invited)

Plasma 2006 – 5th International Symposium on the Intrinsic Josephson Effect in High T_C Superconductors, London, July 17 – 19, 2006

M. Mans, H. Schneidewind, M. Büenfeld, A. Grib, F. Schmidl, P. Seidel
Intrinsic Josephson junctions on Tl-2212 thin films on vicinal cut $LaAlO_3$ with misorientation angles of 15°, 20° and 25°

International Conference on Atomic Collisions in Solids (ICACS), Berlin, July 21 - 26, 2006

P.I. Gaiduk, S.L. Prokopev, W. Wesch, A. Nylandsted Larsen
Nanocluster formation in Ge^+ Sn-implanted SiO_2 layers

Applied Superconductivity Conference (ASC), Seattle, USA, August 28 – September 01, 2006

W. Vodel, R. Neubert, S. Nietzsche, K. Knaack, K. Wittenburg, A. Peters
LTS-SQUID based measurement tool for characterization of superconductive RF cavities (invited poster)

P. Seidel, T. Foerster, H. Schneidewind, C. Becker, V. Grosse, A. Steppke, P. Lorenz, R. Pietzcker, F. Schmidl
Preparation and characterization of high-temperature superconducting dc SQUID-gradiometers in flip-chip configuration (invited poster)

European Microwave Week, Manchester, UK, September 10 -15, 2006

W. Richter
Semiconductor materials for RF transistor applications

International Symposium of the European Materials Research Society (EMRS), Warsaw, Poland, September 04 - 08, 2006

M. Hayes, F.D. Auret, P.J. Janse van Rensburg, J.M. Nel, W. Wesch, E. Wendler
Electrical characterization of He^+ irradiated n-ZnO

European Microwave Week, Manchester, UK, September 10-15, 2006

W. Richter
Semiconductor materials for RF transistor applications

15th International Conference on Ion Beam Modification of Materials (IBMM 2006), Taormina, Italy, September 17 - 22, 2006

P.I. Gaiduk, W. Wesch, A. Nylandsted Larsen
Implantation in pseudomorphic SiGe/Si multilayers: effect of strain on defect evolution

A. Hedler, S. Klaumünzer, J.K.N. Lindner, T. Frosch, N. Darowski, I. Zizak, J. Popp, W. Wesch
Void formation in amorphous silicon during swift heavy ion irradiation

F. Schrempel, Ch. Beeker, W. Wesch
Waveguide barriers with adjustable refractive index produced in KTP by irradiation with He- and Li-ions

M. Hayes, F.D. Auret, J. Nel, W. Wesch, E. Wendler
Electrical characterization of low temperature proton irradiated n-ZnO

E. Wendler, W. Wesch
Ion-beam induced effects at 15 K in MgO

A. Kamarou, W. Wesch, E. Wendler, A. Undisz, M. Rettenmayr
Effect of high electronic excitation in swift heavy ion irradiated semiconductors

C.S. Schnohr, E. Wendler, K. Gärtner, W. Wesch
Room temperature annealing of low-temperature ion implanted sapphire

O. Picht, W. Wesch, J. Biskupek, U. Kaiser, M. Kawasaki, M.A. Oliveira, A. Neves, N.A. Sobolev
Ion beam synthesis of Mn/As nanoclusters in Si

P.I. Gaiduk, S.L. Prokophev, W. Wesch, A. Nylandsted-Larsen
Nanocluster formation in $Ge^{+}Sn$ implanted SiO_2 layers

P.I. Gaiduk, W. Wesch, A. Nylandsted-Larsen
Implantation in pseudomorphic SiGe/Si multilayers: effect of strain on defect evolution

Z.S. Hussain, W. Wesch, E. Wendler, M.C. Ridgway
Amorphous phase formation in ion implanted $In_xGa_{1-x}As$

3. Ferrofluid Workshop, Benediktbeuren, Germany, September 26 – 30, 2006

F. Schmidl, M. Büttner, T. Müller, S. Prass, T. Köttig, P. Weber, M. Mans, Christian Worsch, J. Heinrich, K. Wagner, M. Röder, D.V. Berkov, P. Görnert, G. Glöckel, W. Weitschies, P. Seidel
Temperature dependent Néel relaxation (TMRX) measurements for characterization of nanoparticle distributions

Kryoelektronische Bauelemente 06, Gabelbach, Germany, October 03 – 05, 2006

M. Thürk
Kleinkühler für kryoelektronische Anwendungen

F. Schmidl, M. Büttner, T. Müller, S. Prass, P. Weber, A. Steppke, C. Becker, P. Seidel
Temperaturabhängige Magnetorelaxationsmessungen mit SQUID Systemen

R. Geithner, H. Mühlig, M. Büenfeld, M. Grube, F. Schmidl, B.Schröter, W. Richter, P. Seidel
Elektrische Messungen an Kohlenstoff-Nanoröhren

C. Becker, T. Foerster, H. Schneidewind, A. Steppke, V. Grosse, F. Schmidl, P. Seidel
Charakterisierung von HTSL-dc-SQUID-Gradiometern in Flip-Chip-Konfiguration für ungeschirmte Messungen

European Workshop NanoLum V, Troyes, France, October 13 – 14, 2006

F. Huisken
Photoluminescence studies of silicon-based nanostructures

STREGA annual meeting, Imperial College, London, October 25 – 28, 2006

R. Nawrodt, A. Zimmer, S. Nietzsche, W. Vodel, P. Seidel
Cryogenic Q-factor measurements on calcium fluoride

A. Zimmer, R. Nawrodt, R. Neubert, S. Nietzsche, M. Thürk, W. Vodel, P. Seidel
Relaxation mechanisms in solids

PV-Uni-Netz Jahrestagung 2006, TU Hamburg-Harburg, November 23 - 24, 2006

J. Eberhardt
Epitaxial and polycrystalline $CuInS_2$ thin films: A comparison of opto-electronical properties

U. Reislöhner, M. Hädrich, N. Lorenz, H. Metzner, W. Witthuhn
Doping profiles in CdTe/CdS thin films solar cells (Poster)

Gruppenseminar des Hahn-Meitner-Instituts, Berlin, Germany, December 12, 2006

A. Kamarou
Radiation damage formation and annealing in semiconductors due to fast heavy ions

International Workshop on *Carbon in Space*
Organized by Friedrich Huisken, Thomas Henning, and Luigi Colangeli
Villa Vigoni, Loveno di Menaggio, Como, Italy, May 22 – 25, 2006

5.3 Theses

Diploma Theses

Ralf Bechstein	*Untersuchung unterschiedlicher Isolatormaterialien für die Herstellung intrinsicher Josephson-Kontakte*
Christian Beeker	*Untersuchungen zur gezielten Änderung des Brechungsindex von $KTiOPO_4$ (KTP) durch Bestrahlung mit leichten Ionen und nachfolgender Temperaturbehandlung*
Roland Beyer	*Aufbau und Entwicklung von Neutronen-Flugzeit-Detektoren für die Untersuchung astrophysikalisch relevanter (γ,n)-Reaktionen*
Gerald Broenstrup	*MD-Simulation von Ionenspuren in Halbleitern*
Matthias Büenfeld	*Untersuchung verschiedener Varianten von Josephson-Kontakten auf der Basis von TBCCO-Schichten*
Markus Büttner	*Untersuchungen zu einem Messsystem für den Nachweis magnetischer Nanopartikel*
Tobias Förster	*Hochempfindliche Gradiometer für unabgeschirmte Messungen magnetischer Felder*
Jan Gaber	*Computergestützte Projektion von räumlichen Bildern*
Thomas Gischkat	*Untersuchung zur Beeinflussung des chemischen Ätzverhaltens von $LiNbO_3$ durch Ionenbestrahlung*
Christian Herbst	*Festkörper-NMR-Untersuchungen an isotopen-markierten biologischen Systemen*

Tobias Huke	*Nachbau und Erprobung eines Raste-Tunneleffekt-Mikroskops*
Sebastian Mack	*Herstellung und Charakterisierung von CSS-CdTe-Dünnschicht-Solarzellen*
Sabine Ohser (extern)	*Ultraschnelle Dynamik von Elektronen in Halbleiterquantenstrukturen*
Christian Patzig	*Herstellung und Charakterisierung dünner Bi-Schichten auf nichtgitterangepassten Substraten*
Jakob Reinisch	*Einfluss der Prozessbedingungen auf das Ätzverhalten von ionenbestrahltem $LiNbO_3$*
Kristian Schulz	*Polykristalline $CuInS_2$-Schichten für Solarzellen: strukturelle und optische Untersuchungen*
Daniel Wittig (extern)	*Implementation of switching current control of classical and quantum superconducting Josephson-circuits*

Examenspreis 2006 der Friedrich-Schiller-Universität

Claudia Schnohr
Ion-beam induced effects in alpha-Al_2O_3 of different orientations at 15 K

PhD-Theses

Janko Cieslak	*Epitaxie von Cu(In,Ga)S_2 auf Si-Substraten*
André Hedler	*Untersuchungen zur Auswirkung des hohen elektronischen Energieeintrags in amorphem Silizium während der Bestrahlung mit schweren energiereichen Ionen*

Andrey Kamarou	*Radiation effects and damage formation in semiconductors due to high-energy ion irradiation*
Thomas Kups	*Transmissionselektronenmikroskopische Untersuchungen zur Gitterplatzbesetzung von Dotanden in Siliziumkarbid*
Ronny Stolz (extern)	*Supraleitende Quanteninterferenzdetektor-Gradiometersysteme für den geophysikalischen Einsatz*

5.4 Invited talks and colloquia

F. Huisken
Matrix-Spektroskopie im Molekularstrahl: Untersuchung von Clustern und astrophysikalisch relevanten Molekülen in Helium-Tröpfchen
Vortrag im Rahmen des Veranstaltungszyklus der Gesellschaft Deutscher Chemiker, Naturwissenschaftliche Fakultät IV (Chemie und Pharmazie) der Universität Regensburg, January 30, 2006

F. Huisken
Electronic spectroscopy of polycyclic aromatic hydrocarbons (PAHs) in supersonic jets and ultracold helium nanodroplets
Invited seminar lecture at the Max Planck Institut for Nuclear Physics, Heidelberg, 14.06.2006

F. Huisken
Halbleiter- und Metall-Nanoteilchen aus der Laserpyrolyse: Herstellung und Charakterisierung ihrer Eigenschaften
Vortrag im Rahmen des IPHT-Kolloquiums, Institut für Physikalische Hochtechnologien, Jena 21.06.2006

F. Huisken
Si nanocrystals embedded in silica matrices
Invited lecture at the Workshop of the DFG-Forschergruppe *Laborastrophysik* "Silicon-based dust in Space", Jena, 07.07.2006

Prof. P. Seidel
Supraleitende Quanteninterferometer für die Präzissionsmesstechnik
Kolloquium des Leibniz-Institutes für Festkörper- und Werkstofforschung, Dresden, 11.05.06

W. Vodel
Superconductivity - Basics and Applications in High Precision Measurements
3rd German Vietnam Summer School, Hanoi and Ho Chi Minh City, 18.-22.09.2006

6. Cooperations, guests and colloquia at IFK

The Institute of Solid State Physics collaborates with a large number of Institutes and Universities in Germany and around the world and has also close connections with several companies. In the framework of these wide spread contacts in 2006 a number of scientists from various countries visited our Institute to perform experiments, discuss scientific results obtained within joint projects and to give talks in the colloquium of the Institute of Solid State Physics.

6.1 Visiting scientists

Prof. Dr. R. Alexandrescu	Institute of Laser, Plasma and Radiation Physics, Bukarest, Romania
Dr. M. Belogolovskii	Physikalisch-Technisches Institut Donetsk, Ukraine
Dr. Geppo Cagnoli	Universität Glasgow
Elisabetta Cesarini	Universität Florenz
Maxim Chukharkin	Moskauer Staatliche Universität
Dr. A. Chuvilin	Institute of Catalysis, Novosibirsk, Russia
Prof. Dr. Jan Fulara	Polish Academy of Sciences, Warszawa, Polen
Prof. P.I. Gaiduk	Faculty of Radiophysics and Electronics, Minsk, Belarus
Dr. Federico Garrido	Centre de Spectrometrie Nucleare et de Spectrometrie de Masse, Orsay, France
Prof. Ya. Greenberg	Staatl. Techn. Univ. Novosibirsk
Dr. A. Gryb	Staatliche Universität Kharkov, Ukraine
Dr. Olivier Guillois	Laboratoire Francis Perrin, CEA Saclay, Gif-sur-Yvette, France
Prof. Dr. M. Hayes	University of Pretoria, Physics Department, South Africa
Prof. Jim Hough	Universität Glasgow
Dr. Kim Quang Hui	Kim II Sung University Pyongyang, Nordkorea
Dr. Maria Katsikini	Aristotle University of Thessaloniki, Thessaloniki, Greece
Dr. Y.-S. Kim	Korea Institute of Geology, Mining and Materials, Taejon, Korea
Prof. Dr. F. F. Komarov	Institute of Applied Physics Problems, Minsk, Belarus
Prof. Victor Kornev	Moscow State University, Moscow Russia
Dr. Istvan Kovacs	Research Institute for Technical Physics and Material Science Budapest, Hungary
Prof. Dr. Jacek Krelowski	University of Torun, Poland
Prof. Mikhail Kuprianov	Moskauer Staatliche Universität
Dr. Gilles Ledoux	Université Claude Bernard, Lyon, France
Dr. Katharina Lorenz	Instituto Tecnologico e Nuclear, Sacavem, Portugal
Matteo Lorenzini	Universität Florenz
Peter Murra	Universität Glasgow
Stuart Reid	Universität Glasgow
Dr. Cécile Reynaud	Laboratoire Francis Perrin, CEA Saclay, France
Prof. Sheila Rowan	Universität Glasgow
Dr. S. Shevchenko	Institut of Low Temperature Physic and Engineering, Kharkov, Ukraine
Prof. Dr. O. Snigirev	Moskow State University, Moscow, Russia
Prof. V. Shnyrkov	Institute of Low Temperature Physics and Engineering, Kharkov, Ukraine
Prof. Dr. N. A. Sobolev	Departamento de Fisica, Universidade de Aveiro, Aveiro,Portugal
Dr. E. Soldatov	Moscow State University, Moscow Russia
Dr. Yuri M. Shukrinov	Kernforschungszentrum Dubna

In the framework of a collaboration between the University of Pretoria, South Africa, and the Institute of Solid State Physikcs, supported by the Bundesforoschungsministerium (BMBF) and the National Research Foundation (NRF) South Africa, Prof. Michael Hayes spent a two-months fellowships in Jena. Together with Prof. Werner Wesch and his colleagues he investigated the primary process of damage formation during ion irradiation of several technologically relevant semiconductors using the two-beam radiation facility of the Institut of Solid State Physics. This facility enables irradiation at temperatures down to 15 K and subsequent ion beam analysis of structural modifications without warming up the samples. “Here I have the only opportunity to study the ion-beam induced materials modifications in one step”, said Prof. Hayes. “Another reason to collaborate with the Ion Beam Physics Group in Jena are the expertise and the international reputation of this group”, he added.

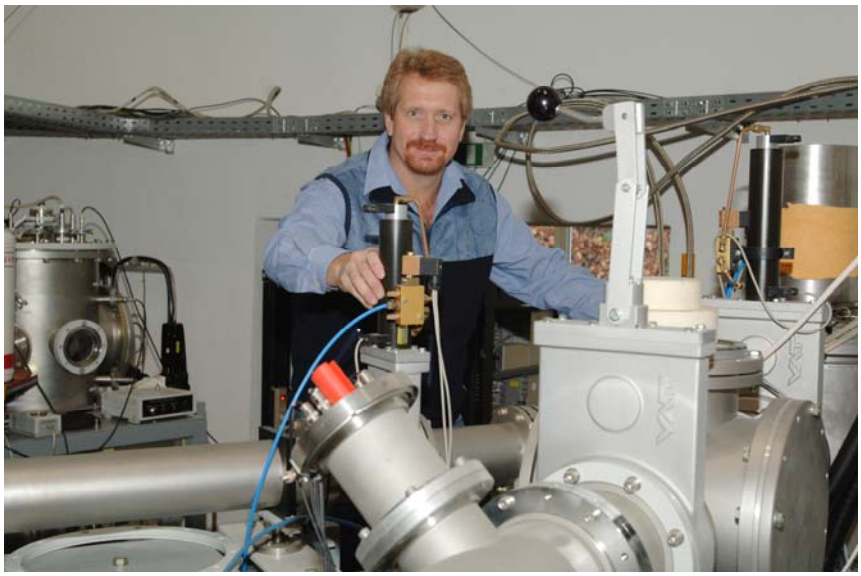

6.2 Colloquia at the Institute of Solid State Physics

Dr. Herbert Wolf
Fremdatome und Diffusion in CdTe
Universität Saarbrücken, 20. Januar 2006

Dr. Rainer Sielemann
Atomare Defekte und Magnetismus an Eisenatomen in Grafit
Hahn-Meitner-Institut Berlin, 27. Januar 2006

Prof. Dr. H.-E. Mahnke
Photoeffekt und Nanostrukturen - Röntgenabsorptionsspektroskopie
Ionenstrahllabor ISL, Hahn-Meitner-Institut Berlin, 07. Juli 2006

Dr. G. Hildebrandt
Modifizierung von metallischen Implantatoberflächen zur Verbesserung des Einwachstums in Knochengewebe
iba Heiligenstadt, 21.Juli 2006

Dr. Petra Meier
Entwicklung eines künstlichen Wurmes für die minimal invasive Chirurgie
Technische Universität Ilmenau, 10. November 2006

Dr. M. Dubiel
Struktur und Eigenschaften von Ag- und Ag/Au-Nanoteilchen in ionenimplantierten Gläsern
Universität Halle, 20. November 2006

7. Teaching activities

7.1 Lectures

Experimentalphysik I SS 2006, WS 2006/2007	Prof. Dr. P. Seidel
Experimentalphysik II für Physiker, Mathematiker, Chemiker und Lehramt, WS 2005/2006	Prof. Dr. W. Witthuhn
Experimentalphysik III für Physiker SS 2006	Prof. Dr. W. Witthuhn
Experimentalphysik III für Physiker WS 2005/2006	Prof. Dr. W. Wesch
Experimentalphysik für Biologen, Ernährungswissenschaftler und Pharmazeuten WS 2005/2006, WS 2006/2007	Prof. Dr. W. Wesch
Experimentalphysik für Mediziner und Biochemiker WS 2005/2006, SS 2006, WS 2006/2007	Prof. Dr. W. Richter
Kern- und Elementarteilchenphysik für Physiker SS 2006	Prof. Dr. W. Wesch
Elektronik WS 2005/2006, SS 2006, WS 2006/2007	PD Dr. F. Schmidl Dr. W. Vodel
Einführung in die Festkörperphysik WS 2005/2006, WS 2006/2007	Prof. Dr. P. Seidel PD Dr. F. Schmidl
Ausgewählte Kapitel der Quantentheorie WS 2005/2006, WS 2006/2007	PD Dr. K. Gärtner
Grundlagen des Quantum Computing WS 2006/2007	PD Dr. W. Krech
Kern- und Elementarteilchenphysik SS 2006	Prof. Dr. W. Richter
Halbleiterphysik SS 2006	Prof. Dr. W. Richter
Halbleiter-Optoelektronik, WS 2005/2006, WS 2006/2007	Prof. Dr. W. Richter
Schicht- und Oberflächenanalyse (FH Jena) WS 2005/2006, WS 2006/2007	Prof. Dr. W. Richter
Dünnschichtphysik I SS 2006	Prof. Dr. P. Seidel

Dünnschichtphysik II WS 2006/2007	Prof. Dr. P. Seidel
Supraleitende Quanteninterferometer WS 2005/2006	Prof. Dr. P. Seidel
Grundlagen und Anwendungen der Josephsoneffekte SS 2005	Prof. Dr. P. Seidel PD Dr. H.-G. Meyer
Nanophysik I: Cluster WS 2006/2007	Prof. Dr. Fr. Huisken
Cluster und Nanoteilchen II SS 2006	Prof. Dr. Fr. Huisken
Labor-Astrophysik WS 2006/2007	Prof. Dr. Fr. Huisken, Dr. H. Mutschke
Nukleare Festkörperphysik I SS 2005	Prof. Dr. W. Wesch, PD Dr. K. Gärtner, Dr. E. Wendler
Nukleare Festkörperphysik II WS 2004/2005	Prof. Dr. W. Wesch, Dr. F. Schrempel, Dr. E. Wendler
Festkörpermodifizierung mit Ionenstrahlen WS 2005/2006	Prof. Dr. W. Wesch PD Dr. K. Gärtner, Dr. E. Wendler
Analyse von Oberflächen und Schichten WS2004/5, WS2005/6 (FH Jena)	Dr. B. Schröter

7.2 Seminars

Experimentalphysik II	Dr. F. Schrempel
Experimentalphysik I und III	Dr. E. Wendler
Physik für Ernährungswissenschaftler	Dr. E. Wendler
Kern- und Elementarteilchenphysik	PD Dr. K. Gärtner
Kern- und Elementarteilchenphysik	Prof. Dr. W. Richter
Physik für Biologen	Prof. Dr. W. Wesch
Physik für Pharmazeuten	Prof. Dr. W. Wesch
Experimentalphysik für Biogeowissenschaftler	PD Dr. W. Krech
Institutsseminar	Prof. Dr. W. Witthuhn
Nukleare Festkörperphysik	Prof. Dr. W. Witthuhn, Prof. Dr. W. Wesch

Physik dünner Schichten	Prof. Dr. W. Richter
Tieftemperaturphysik und Supraleitung	Prof. Dr. P. Seidel
Elektronik (Lehramtsstudenten)	PD Dr. F. Schmidl
Elektronik (Physik-Diplom, Informatik)	Dr. W. Vodel, PD Dr. F. Schmidl
Einführung in die Festkörperphysik	PD Dr. F. Schmidl, A. Zimmer Dipl.-Phys. M. Büttner

7.3 Practica

Grundpraktikum	Prof. Dr. W. Wesch Dr. K. Gärtner, Dr. Th. Hahn, Dr. Ch. Hülsen, PD Dr. W. Krech
F-Praktikum	Dr. B. Schröter, Dipl.-Ing. M. Thürk Dipl.-Phys. M. Büenfeld, Dipl.-Phys. R. Nawrodt
F-Praktikum (Kernphysik)	Dr. U. Reislöhner Dr. F. Schrempel
Elektronikpraktikum	Dr. W. Vodel PD Dr. F. Schmidl, Dr. S. Nietzsche Dipl.-Phys. R. Nawrodt Dipl.-Phys. F. Perner, Dipl.-Ing. R. Neubert Dipl.-Ing. Mühlig Dipl.-Phys. V. Große Dipl.-Phys. Ch. Becker
Weihnachtsvorlesung	Prof. Dr. P. Seidel Prof. Dr. W. Wesch

Weihnachtsvorlesung 2006

8. Personnel

Professors

Prof. Dr. habil. Wolfgang Witthuhn (director)
Prof. Dr. habil. Wolfgang Richter
Prof. Dr. habil. Paul Seidel
Prof. Dr. habil. Werner Wesch
Prof. Dr. habil. Friedrich Huisken

Scientific Staff

PD Dr. habil. Konrad Gärtner
PD Dr. habil. Heinrich Metzner
PD Dr. habil Frank Schmidl
Dr. Olivier Debieu
Dr. Gaël Rouillé
Dr. Ernst Glaser
Dr. Thomas Hahn
Dr. Christian Hülsen
Dr. Cornelia Jäger
Dr. Sandor Nietzsche
Dr. Udo Reislöhner
Dr. Frank Schrempel
Dr. Bernd Schröter
Dr. Thomas Stelzner
Dr. Wolfgang Vodel
Dr. habil. Elke Wendler

PhD Students

Marco Arold
Christoph Becker
Daniel Baumgarten (Biomagn. Zentrum)
Matthias Büenfeld
Markus Büttner
Janko Cieslak
Oliver Debieu
Jens Eberhardt
Thomas Gischkat
Veit Große
Mathias Hädrich
André Hedler (to 10/06)
Rico Hohmuth (to 05/06)
Andrey Kamarou
Torsten Köttig
Mario Liehr (Biomagn. Zentrum)
Michael Mans
Stefan Moldenhauer (Air Liquide)
Ronny Nawrodt
Katja Peiselt (IPHT Jena)
Oliver Picht
Kerstin Riedel (Fritz-Lipmann Institut)
Ronny Stolz (IPHT Jena)
Anja Zimmer

Diploma Students

Ralf Bechstein
Roland Beyer (FZ Rossendorf)
Michael Blech
Gerald Brönstrup
Tina Clauß
Björn Hendrik Eisenhower (IPHT)
Tobias Förster
Rene Geithner
Matthias Grube
Alexander Hartung
Stefan Hechler
Daniel Heinert
Christian Herbst (Fritz-Lipmann Institut)
Matthias Hudl
Carsten Jähne
Manuela Janietz
Andreas Joswig
Roland Koim
Christian Kraft
Christiane Löffler
Sebastian Mack
Johanna Malsch
Thomas Müller
Michael Oertel
Sabine Ohser (FZ Rossendorf)
Christian Patzig
Robert Pietzcker
Thomas Reicher
Matthias Schmelz (IPHT)
Torsten Schmidt
Annett Schröter
Christian Schwarz
Holger Sihler
Johannes Slotta
Mathias Steglich
Tobias Steinbach
Michael Steinert
Alexander Steppke
Reinhard Volkmer
Alexander Voigt (Strahlentherapie)
Martin Voitsch
Mathias Weiß
Daniel Wittig
Gabriele Zieger

Technical Staff

Ulrich Barth
Uta Bornkessel
Uwe Eberhardt
Lutz Föllmer
Silke Frunzke
Kristina Garlipp
Dieter Hasler
Torsten Hilprecht
Frank Jehn
Dr. Günther Kirsch (to 08/06)
Gerald Lenk
Holger Mühlig
Anja Mittelstädt
Ralf Neubert
Stefan Prass
Helga Rudolph
Sigrun Schurbaum (ATZ)
Sylvia Stender
Matthias Thürk
Carmen Voigt